MASTERS THESIS

January 15, 2015

Single top channel in association with $H \rightarrow b\bar{b}$ production at ATLAS: a feasibility study

Claire Antel

University of Cape Town

supervisor and co-supervisor:
Dr Andrew Hamilton and Dr Heather Gray

Claire Antel
antcla002@myuct.ac.za

This dissertation is submitted to the Faculty of Science at the University of Cape Town, in complete fulfilment of the requirements for the degree of Master in Science.

As the candidate's supervisor, I have approved this dissertation for submission.

Signed:

Signed by candidate	20/01/2015
Dr Andrew Hamilton	Date

Student Declaration

I, the undersigned, hereby declare that the work contained in this thesis is my original work, and that any work done by others or previously by myself has been acknowledged and referenced accordingly.

Signed:

Signed by candidate	15/10/2014
Claire Antel	Date

Abstract

A degeneracy in the minima of the profile likelihood function of the Higgs boson coupling to fermions and bosons, where boson couplings are assumed to be positive, is reported by both ATLAS and CMS. Although one minimum lies in the region of positive fermionic coupling scale factors, consistent with the Standard Model, the second minimum lies in the negative region - a region which would indicate new physics.

This degeneracy can potentially be resolved by studying a fermionic-bosonic interference that takes place in the single top quark production in association with a Higgs particle, in which the cross-section is significantly enhanced for anomalous coupling values. A truth level feasibility study of the tH process with $H \rightarrow b\bar{b}$ is conducted at 8 TeV and 21 fb^{-1} of integrated luminosity, the equivalent of the 2012 run at the LHC. A sensitivity of 1.7σ is found for the enhanced case of a coupling scale factor of $c_F = -1$. This is insufficient for a detection. A projection to 14 TeV centre-of-mass energies indicates that at truth-level a 3σ significance with 15 fb^{-1} of integrated luminosity can be reached for the enhanced case. However, assuming as low as 5% systematic uncertainty lowers this to below 2σ across the whole luminosity range, indicating that the upcoming run at LHC will also be insufficient to resolve the degeneracy.

Acknowledgement

I would like to express my appreciation for the opportunity to work with Heather. Her guidance was extremely helpful and her consistent motivation and push kept me going throughout my write-up. I wish to thank her sincerely for all the time she gave me. Even during her busiest times, she gave me constant feedback on my work. I don't know how she does it.

I am deeply thankful for the kind of supervisor and person that Andrew is. His calm manner helped me not panic at times. I appreciated that he was helpful when I asked for help but otherwise left me to my own devices. I am *especially* grateful for all the support and help he offered on work I was doing outside of my masters thesis. I felt like I could go to him about absolute everything.

I would also like to thank Chris Young for looking through the detector-motivated section of my thesis and providing helpful feedback.

Finally, I am grateful for my parents helping me out during the busy times. I believe they still think I study astrophysics. Nevertheless, they were a great source of motivation.

Contents

1 Introduction

One of the primary physics goal of the LHC has in many aspects been achieved - a particle that looks like the Higgs boson has been discovered by the ATLAS and CMS collaborations with a mass of 125 GeV [1, 2]. Therefore the focus of the Higgs physics program has moved to measuring the properties of this particle in order to test if it is *the* Standard Model Higgs boson or if it is Higgs-like but behaves differently to Standard Model (SM) expectations in some way. The latter would mean that we have found new physics beyond the Standard Model (BSM). If direct searches yield no evidence to BSM particles, measuring the new Higgs particle properties could provide an interesting window into new physics.

Measurements of Higgs particle properties thus far are consistent with Standard Model predictions. Using all available data, ATLAS and CMS have observed the new particle with a signal strength of 1.30 ± 0.20 [3] and 0.88 ± 0.21 [4], respectively. The signal strength is defined as σ_{obs}/σ_{SM}, the deviation of the event yield from the expected value. The newly discovered particle is favoured to be a spin-0 particle of +1 charge parity by current analyses, and other hypotheses have been basically ruled out [5, 6]. The natural width of the SM Higgs boson is predicted to be 4 MeV – lower than the instrumental mass resolutions at the LHC experiments. An upper limit of 3.4 GeV at 95% C.L. has been set [6]. Measurements of the coupling strength to other SM particles by ATLAS and CMS have thus far been in compliance with Standard Model predictions. However, non-SM extensions to the Higgs sectors are still not excluded [3][4].

The analysis presented here probes the Higgs boson coupling to the top quark. It is a Monte Carlo feasibility study on single top quark production in association with a Higgs boson, following reference [7]. Due to an interference between the fermionic and bosonic couplings to the Higgs particle, the single top channel in association with Higgs (tH) production offers a unique opportunity to study the *relative* sign of the top Yukawa coupling with respect to the bosonic couplings. The interference leads to an enhancement in the signal for non-SM top Yukawa values and thus detecting this enhanced signal would be evidence for BSM physics. The Higgs particle is analysed via the $H \rightarrow b\bar{b}$ decay channel; the identification and reconstruction of b-jets is thus a prominent component of this analysis.

In addition to the tH feasibility study, this thesis includes a study on *particle flow*, an algorithm that is currently being developed in order to improve the resolution of jet measurements in the ATLAS detection process, and that CMS experiments are successfully using already [8]. Whilst the ATLAS calorimeter intrinsically provides excellent jet resolution, the resolution is considerably deteriorated by pile-up. The success of this project would, among other things, result in improved pile-up rejection.
The feasibility study involves the measurement of three b-jets in an event and in the case of a signal event, two of these are expected to originate from the Higgs particle decay. The mass resolution of the Higgs boson is degraded in a high pile-up environment. The studies on particle flow therefore, although

not studied in conjunction with, are linked to the tH analysis in that the implementation of the algorithm would lead to an improved measurement of the tH signal.

This thesis is laid out as follows. Section 2 covers the theory of the Standard Model (Section 2.1), including subsections on Higgs boson couplings in SM and BSM, which leads on to the theory of the tH process (Section 2.2). Section 3 is a general description of the LHC, followed by a section on the experimental tools used at the LHC – Section 4. This section gives a general description of the ATLAS detector and a more detailed description of subdetectors that are relevant to the current work (Section 4.1). Monte Carlo event generation and simulation is described in Section 4.2. This precedes a description of ATLAS physics analysis at a reconstructed level (Section 4.3) and at truth level (Section 4.4), the level at which the present tH analysis is performed. Section 5 is the detector performance motivated part of this thesis: it details the particle flow research at ATLAS and my contributions to it. Finally, sections 6 onwards cover the analysis, results and conclusion of the feasibility study of the tH process – the physics motivated part of this thesis.

2 Theory

2.1 The Standard Model theory

The existence of the famed Higgs particle was predicted 50 years ago as part of the Standard Model (SM) of fundamental particles. After the discovery of the τ neutrino in 2000 [9], the Higgs boson was the only remaining SM particle yet to be observed. The discovery of a Higgs-like particle in 2012 thus officially ended the search for fundamental particles that make up the SM framework.

2.1.1 Particles of the Standard Model

The Standard Model is the closest theory we have to a complete picture of the fundamental constituents of matter and their interactions and has thus far enjoyed wide success in predicting experimental outcomes in particle physics. As presented in Figure 1, the model describes the interplay between a total number of 17 different types of fundamental particles, some of which also have corresponding antiparticles. One of the intrinsic properties of a particle is its spin. A fundamental particle is classified as a *fermion* if its spin is a half integer of $\hbar$[1]. It is classified a *boson* if its spin is an integer number. Whilst the magnitude of a particle's spin is fixed, the direction can change. An electron, for example, is a half spin particle and thus a fermion. Its spin can either be orientated up or down, $+\frac{1}{2}\hbar$ or $-\frac{1}{2}\hbar$. These two types of fundamental particles behave very differently. Whilst fermions may never occupy the same state (all quantum numbers are the same) in a given region, bosons can. For example, only two electrons can occupy the smallest orbital of an atom: one electron with spin $+\frac{1}{2}\hbar$, and another with spin $-\frac{1}{2}\hbar$. This has

[1] spin has units of angular momentum, but cannot be thought of as the same angular momentum as in the classical world as there no such concept of a 'spinning' *point*-like particle.

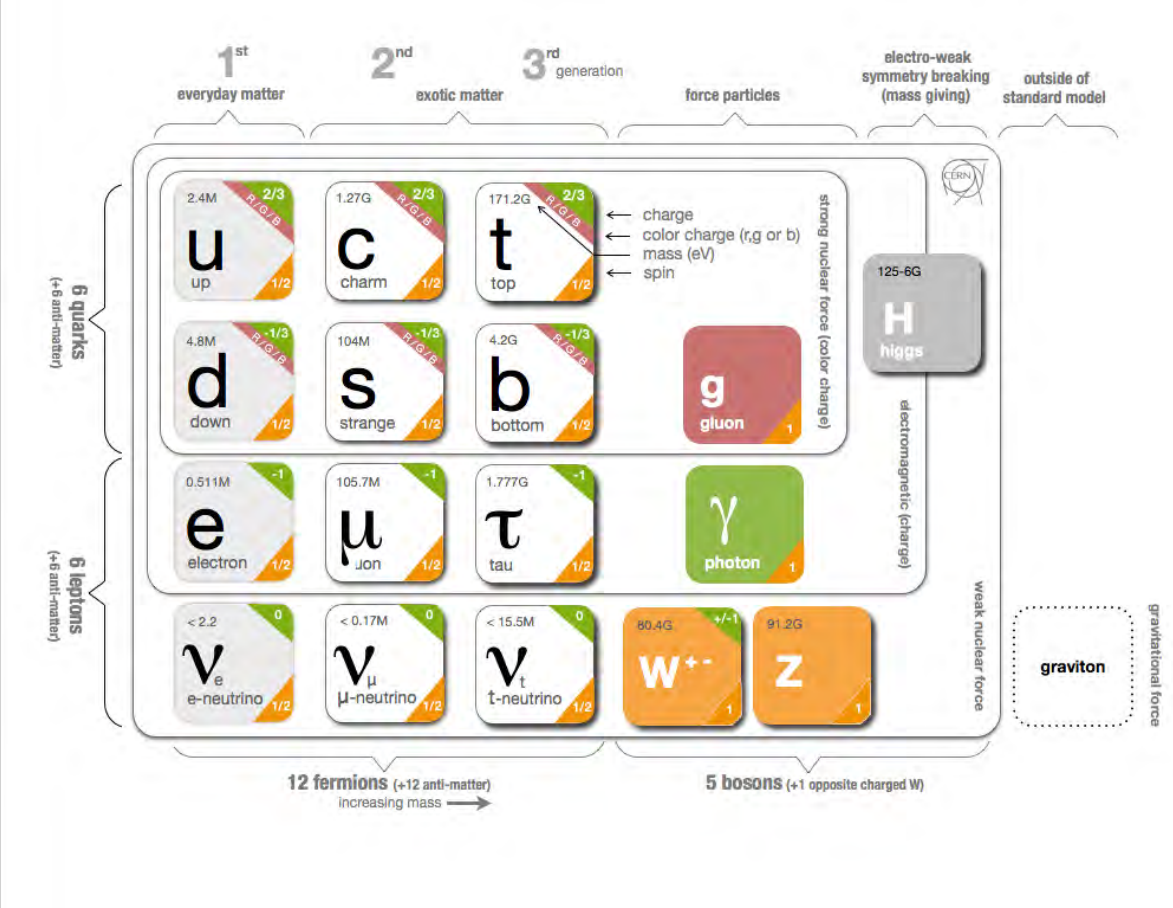

Figure 1: The fundamental particles of the Standard Model: three generations of quarks, three generations of leptons, four gauge bosons associated to three of the four fundamental forces and the scalar Higgs boson. The theoretical graviton, associated to the gravitational force, lies outside of the description of the Standard Model theory. [10]

led to all matter being made of fermions at a fundamental level: their resistance to occupying the same space, means structures of matter are able to form, from protons to atoms to stars. Fundamental bosons (also known as gauge bosons) on the other hand are of a different nature: they *can* occupy the same state. As bosons in the same state are identical, they are interchangeable. In this way, they keep matter glued together, since particles interact by exchanging gauge bosons. They thus generally exhibit a 'radiative' nature. A photon, for example, is a type of gauge boson.

These interactions are related to three of the four fundamental forces: the electromagnetic (EM) force (force between charged particles), the strong force (force that keeps composite particles such as protons or neutrons together) and the weak force (the weakest force after gravity, that is responsible for a lot of radioactive decays, such as neutron to proton decay).

Figure 1 shows particles grouped into leptons and quarks, as well as the forces between particles and the Higgs boson.

The group of leptons contains six members, each with an associated neutrino. The group is divided into three generations: the electron and electron neutrino, the muon and muon neutrino and the τ and τ neutrino. Alongside this group, is a group of corresponding antileptons which are opposite in charge. Neutrinos are almost massless and only interact weakly, making them very elusive – this is why the τ neutrino was discovered fairly recently.

There exist six different flavours of quarks which again can be grouped into three generations: the up and down quark, the strange and charm quark, and the top and bottom quark. These are held together by the strong force and are never observed individually but as composite particles, for example the proton and neutron. There also exist six different antiquarks, opposite in charge. In addition to electrical charge, quarks also carry a so-called colour charge: red, green or blue; or in the case of anti-quarks: antired, antigreen and antiblue. The reason for quarks being locked into composite particles is related to the colour-charge: no particle in nature may be observed as 'coloured', it must be colourless by being either made up of e.g. a red and anti-red quark or a (anti-)red, a (anti-)green and a (anti-)blue quark combination. This is known as *colour confinement*. No single quark can ever be detected directly as a consequence. Instead *hadronisation* takes place. That is, when a quark is produced in a high-energy collision it will instantly combine with virtual quarks and anti-quarks from the vacuum. The formed hadrons fragment and recombine until all hadrons are stable and colourless. These are observed as so-called *jets* in particle detectors.

Lastly there are the gauge bosons, or force carriers, that are associated to three of the four fundamental forces. Photons are exchanged between all particles that are electrically charged and thus experience the electromagnetic force. The gluon is exchanged between strongly-charged quarks. A fundamental difference is that the gluon itself carries a colour- and anticolour-charge and can thus couple to itself. The weak force is mediated by the Z and $W^{\pm}$ bosons and all particles experience this force. A quark can change its flavour through the emission of a W boson which carries away charge. The flavour change is what allows a neutron (udd) to decay to a proton (uud), for example. The Z boson in contrast is neutral. Neutrinos are the only particles that interact exclusively with the weak bosons.

The last particle, and also the last to be discovered, is the Higgs boson. The Higgs boson is not a mediator of a force so to speak. Instead it has lent particles their masses.

An additional gauge boson may be added beside this framework: the graviton, mediator of the gravitational force. As the gravitational force is also a fundamental force, this particle should naturally exist. However the Standard Model offers no description of particle interactions via this extremely weak force and so is not part of the Standard Model theory. Now that the Standard Model has been fully observed, a quantum description of gravity is probably one of the most important unanswered questions in physics at present.

The theoretical framework for the description of particles and their interactions in the Standard Model is *relativistic quantum field theory* (QFT). It treats particles as an excitation of a field continuous in space

and particle interactions as interactions between two fields.
The quantum field theory describing the electromagnetic field is known as quantum electrodynamics (QED) and that describing the strong field is known as quantum chromodynamics (QCD). The theory for the weak field falls under *electroweak theory*. Within this theory, the electromagnetic and weak forces are unified and only become two separate forces through *electroweak symmetry breaking*, which will be described in Section 2.1.3. The following section describes the mathematical formalism that QFT makes use of: the so-called Lagrangian.

2.1.2 The Lagrangian

In classical mechanics, the Lagrangian, L, is given as the kinetic minus the potential energy of a particle. In order to deduce the equation of motion of the particle from this, it is postulated that a particle will choose to travel along the path of *least action*. This means calculating the function L(x(t)) for which the path integral is a minimum. The solution for the minimizing function is given by the Euler-Lagrange equation,

$$\frac{\partial L}{\partial x} = \frac{d}{dt}\frac{\partial L}{\partial \dot{x}}. \tag{1}$$

In quantum mechanics, particles are described as fields rather than localised points. These fields are a function of space and time. In order to describe the behaviour of a field, we start with the Lagrangian density, $\mathcal{L}$, where $L = \int \mathcal{L} d^3x$. This is a function of the fields and their local (x, y, z) and time (t) derivatives.
For example, a free electron - or any spin-$\frac{1}{2}$ field, f with mass m - is described by the Dirac equation

$$i\hbar\gamma^\mu \frac{\partial}{\partial x_{mu}} f - mcf = 0 \tag{2}$$

(and similarly for the conjugate field $\bar{f}$). Here, γ^μ are the Dirac matrices satisfying $(\gamma^0)^2 = 1$, $(\gamma^1)^2 = (\gamma^2)^2 = (\gamma^3)^2 = -1$ and $\gamma^\mu\gamma^\nu + \gamma^\nu\gamma^\mu = 0$, constructed to be able to eliminate exactly these cross-terms.
The Lagrangian density, which gives such a solution for the Euler-Lagrange equation, is

$$\mathcal{L} = i\hbar c\bar{f}\gamma^\mu \frac{\partial}{\partial x_\mu} f - (mc^2)\bar{f}f. \tag{3}$$

The first term characterizes the kinetics and the second term the potential due to the particle's mass.

For a massive free Spin-1 field, A^μ, the Lagrangian reads

$$\mathcal{L} = -\frac{1}{16\pi}F^{\mu\nu}F_{\mu\nu} + \frac{1}{8\pi}(\frac{mc}{\hbar})^2 A^\nu A_\nu, \tag{4}$$

where $F^{\mu\nu} \equiv \partial^\mu A^\nu - \partial^\mu A^\nu$.

2.1.3 Electroweak Symmetry Breaking and the Higgs field

The Higgs field and the associated particle emerged from the independent work done by Peter Higgs [11] and Francois Englert and Robert Brout [12] in 1964. The theoretical construct of the new particle resulted from a symmetry breaking mechanism that was formulated in order to explain where the W and Z boson masses originate while the photon remains massless. This mechanism was lined out by both Higgs and Englert and Brout, hence now called the *BEH mechanism*. Peter Higgs however further mentioned in his paper that this may lead to a new scalar particle. The particle is therefore now known as the Higgs boson.

The motivation for reformulating the theory is due to a certain type of symmetry that is imposed, called *local gauge invariance*. It requires that when a field undergoes a position-dependant transformation in phase, $\Phi \rightarrow e^{i\theta}\Phi$, where $\theta = \theta(x)$ (i.e. depends on the local position in space), the Lagrangian is left invariant. When this is applied, it becomes necessary to introduce a vector (spin 1) field that interacts with the original field.

For an electron (spin-$\frac{1}{2}$ (spinor) field, f) imposing local gauge invariance will return a Lagrangian of the form

$$\mathcal{L} = [i\hbar c\bar{f}\gamma^{\mu}\frac{\partial}{\partial_{\mu}}f - (mc^2)\bar{f}f] - \frac{1}{16\pi}F^{\mu\nu}F_{\mu\nu} + \frac{1}{8\pi}(\frac{mc}{\hbar})^2A^{\nu}A_{\nu} - (q\bar{f}\gamma^{\mu}f)A_{\mu} \tag{5}$$

The first term is Equation 3 for a free electron. The last term emerged from imposing local gauge invariance and describes a coupling between the spinor and vector field. It is therefore natural to also include the second and third term which are from Equation 4 describing a free vector field. However, the Lagrangian is no longer invariant with the addition of the vector particle mass term. The particle must therefore be *massless* so that the invariance is not lost. The massless vector field and its coupling to the electron suitably describes the photon and the electromagnetic interactions.

This works well then in the case of the electrodynamics and chromodynamics where the new 'gauge' fields describe perfectly the massless photon and gluon as well as their couplings to charged and colour-charged particles respectively. But it doesn't match up with the weak mediators, the W and Z bosons, which are massive in nature.

Brout, Englert and Higgs offered a way of solving this by formulating the so-called *electroweak symmetry breaking* (EWSB) mechanism. This is a *spontaneous* breaking of symmetry, meaning that, without any external influences, the system chose a certain direction because *it had to*. In mathematical terms, the Lagrangian of a field, Φ, where $\Phi \rightarrow -\Phi$ leaves $\mathcal{L}$ invariant, is reformulated so that it describes a field Φ', defined in terms of the original field Φ, where suddenly the transformation $\Phi' \rightarrow -\Phi$ is no longer a symmetry. However, local gauge invariance remains preserved in the Lagrangian. The true symmetry is hidden away and the universe behaves according to a system with a 'broken' symmetry.

Once this transformation is made, three new components emerge. Two of these are incorporated to become the mass terms of the W and Z bosons, and the remaining term describes a new scalar (spin 0) field.

The field is shown to interact with fermions, from which additional mass terms for fermions arise [13]:

$$\mathcal{L} = -\frac{m_f}{v} f\bar{f}H + \frac{\frac{3m_H^2}{v}}{6}H^3 + \frac{\frac{3m_H^2}{v^2}}{24}H^4 + \delta_V V_\mu V_\mu (\frac{2m_V^2}{v}H + \frac{\frac{2m_V^2}{v^2}}{2}H^2). \quad (6)$$

where V is for a massive vector boson, i.e. W or Z boson, $\delta_W = 1$ and $\delta_Z = 1/2$ and v is the *vacuum expectation value* (vev) for the Higgs field. This value is the non-zero ground potential of the Higgs field in a vacuum.

2.1.4 Higgs coupling

The strength of the couplings between particles and gauge fields are parameters of the Standard Model that need to be determined empirically. A coupling value translates as the relative strength of forces between particles in the case of the strong, electromagnetic and weak fields, and is determined by the coupling term between two fields in the Lagrangian. This term is quantified by a dimensionless factor, the gauge coupling parameter, g. In each case, the coupling of the respective gauge field behaves differently. In the case of couplings to the Higgs boson, the strength of the coupling is determined by the mass of the particle as shown in Equation 6: for vector bosons, it is proportional to the squared mass, whilst for fermions, it is directly proportional to the mass. The Higgs-fermion coupling is referred to as the *Yukawa coupling*.

2.1.5 Higgs boson couplings in Beyond the Standard Model Theories

Although the Higgs boson discovery was a major boost to the Standard Model, it is not clear that this is the full theory. The theory contains over 20 free parameters, including the mass of particles and coupling strengths, as mentioned in the previous section. We have only obtained these experimentally - SM provides no *prediction* of these. The theory does not include gravity, nor dark matter, a very prominent but mysterious component of our universe. Various Beyond the Standard Model (BSM) theories exist but so far no experimental evidence has confirmed them. It is therefore hoped that evidence of new physics will emerge in searches in particle detectors around the world. Such evidence may help to extend the SM to resolve some of the above deficiencies.

One way to search for new physics in experiments is to study the properties of the newly discovered Higgs particle. Any deviations from the SM prediction in the measurements of its properties may provide hints about BSM physics.
One such property is the Higgs boson coupling strength to other SM particles. As the coupling is determined by the particle masses, the measurements of these give us SM predictions of the respective coupling strengths. The vector boson and fermion coupling strengths can be parametrised using κ_V and

κ_F respectively. These are defined as

$$\kappa_V \equiv g_{hVV}/g^{SM}_{hVV} \qquad \text{and} \qquad \kappa_F \equiv g_{hf\bar{f}}/g^{SM}_{hf\bar{f}} \tag{7}$$

They essentially quantify the deviation from the SM prediction, g^{SM}.

Using all available data from the 7 and 8 TeV runs, ATLAS and CMS have presented preliminary constraints on the fermion and vector boson couplings [14, 15]. The fit results done by ATLAS are shown in Figure 2 [14]. Here, ATLAS and CMS made the following assumptions: the total width of the Higgs

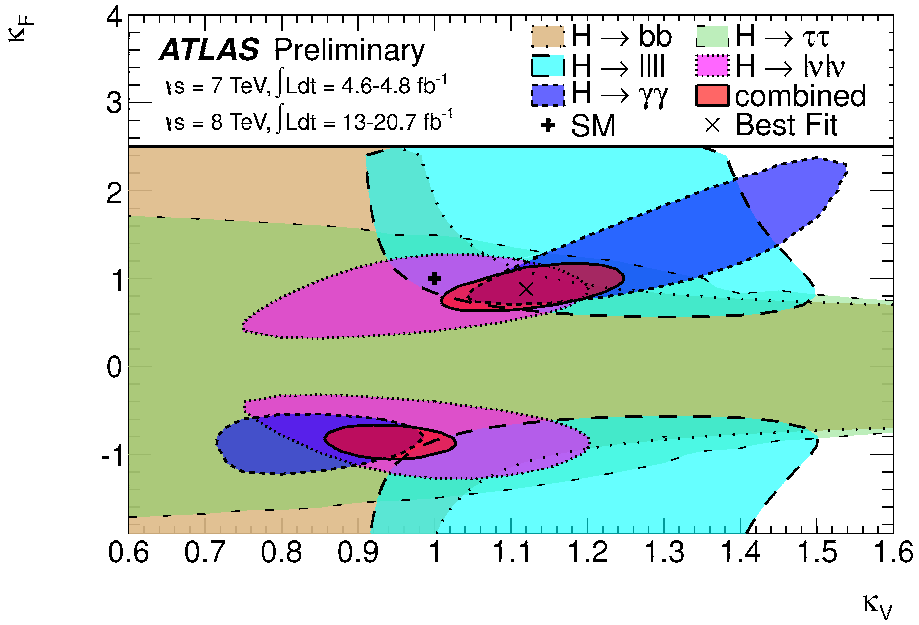

Figure 2: ATLAS κ_V vs κ_F coupling fits for every Higgs particle decay channel and their combination. The dashed lines mark the 68% CL contours. The best fit and the SM prediction (1:1) are marked by crosses. Although the best fit agrees within 68% with SM, there remains an area of positive correlation at negative κ_F values which is significant at a $\sim 1\sigma$ level.[14]

boson has no contributions from non-SM particles, so the sum of all SM particle contributions is taken; similarly, only SM particles contribute to the $\gamma\gamma$ loops (described in the following paragraph); the couplings to *all* fermions/bosons are uniformly modified. The last assumption means, $\kappa_t = \kappa_b = \kappa_\tau = \kappa_g = \kappa_F$ and $\kappa_Z = \kappa_W = \kappa_V$. Interestingly, although the best fit is in agreement with the Standard Model prediction, there remains an area where *negative* values of the Yukawa coupling are still compatible at a 2σ level [14]. This deviation from SM could signify new particles. The degeneracy remains when no assumptions are made on the total width of the Higgs boson.

In the ATLAS fit, κ_V is constrained to > 0; nothing is lost by setting a positive constraint on one of the two factors because only the *relative* sign between the two coupling scale factors is physical. The 68% CL

contour lines are traced out for each fit for a decay channel of the Higgs boson, as well as the combined fit. An important feature of the plot is the symmetry of the areas for every decay channel except for the $H \to \gamma\gamma$ decay. The symmetry in $\pm\kappa_F$ values is due to these channels being *insensitive* to the sign of the fermion coupling value. The $\gamma\gamma$ channel in contrast depends weakly on the relative sign between κ_F and κ_V. This results from the dependence of the event yield on the coupling scale factors which goes like

$$\mathcal{N} \propto \frac{\kappa_x^2 \kappa_y^2}{\kappa_H} \tag{8}$$

where particle x is from the production process and y the decay channel. κ_H is determined by its SM branching ratios to fermions and vector bosons and so given as $0.75\kappa_F^2 + 0.25\kappa_V^2$. Only the absolute values of the κ parameters can be determined because they only enter the equation squared. However, the decay of the Higgs boson to two photons occurs through a loop mediated by heavy virtual particles.

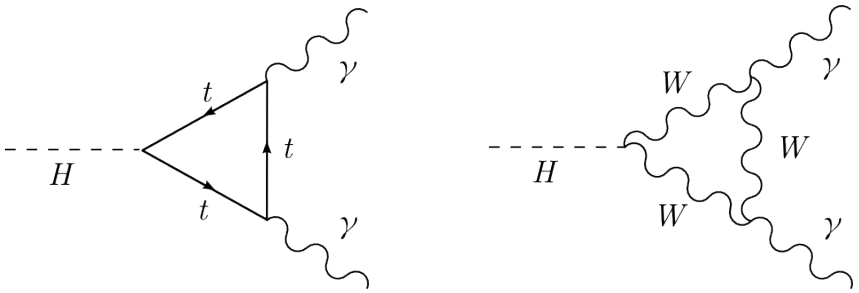

Figure 3: Feynman diagram of the loop-induced $H \to \gamma\gamma$ decay. The two major contributions are the top quark and W boson. Due to the interference of these two processes – one fermionic and the other bosonic – the $\gamma\gamma$ channel is affected by the relative sign between the fermionic and bosonic couplings.

The major loop contributions are from the top quark and W boson, shown in Figure 3. Therefore κ_γ is a function of the more fundamental coupling scale factors, κ_F and κ_V and scales as $|\alpha\kappa_V + \beta\kappa_F|^2$. The interference term between the fermionic and bosonic couplings means that the event yield depends on their relative signs: it is increased for coupling scale factors opposite in sign. This results in the fit currently partially favouring the second minimum at negative signs as shown in Figure 2. The $H \to \gamma\gamma$ decay channel however has the lowest branching ratio ($\sim 0.2\%$) and there are not enough statistics yet to lift this degeneracy. Other processes that are sensitive to the relative fermionic/bosonic coupling sign should therefore be studied.

2.2 The tH process

The top quark is unique in that it is exceptionally massive when compared to the other quarks. It is, in fact, at 173 GeV the most massive fundamental particle in the Standard Model. The second heaviest quark is the bottom quark with a mass of 4 GeV [16]. The top quark's high mass leads to a lifetime that

is short enough for it to decay before it hadronises. The top quark is thus the only quark we can observe as a 'bare' quark – through the detection of its decay products instead of only within a hadron. The top Yukawa coupling is similarly interesting because of the relation of the Higgs field to particle masses, which is proportional to their mass. This means one may expect the top quark to play a special role in the electroweak symmetry breaking mechanism.

It has been suggested in several works (e.g. [7, 17, 18, 19]) that the ambiguity in Higgs boson coupling measurements discussed in the previous section can be resolved from measurements of the single top channel in association with the Higgs. This channel presents a unique opportunity which is to study the relative signs of the fermionic and bosonic couplings. The core process is $W + b \rightarrow t + H$, illustrated in Figure 4. A W boson is radiated off a quark, and interacts with a bottom quark to produce a top quark. The grey circle denotes the region where different processes come into play. The two main processes are presented in Figure 5, where the Higgs boson is either radiated off a top quark or a W boson. There exists an interference between the fermionic and bosonic couplings that enhances the event yield if the scale factors are opposite in sign. In addition to the cross-section, the change in the Yukawa coupling value also affects the branching ratios of Higgs boson.
A negative sign of the top Yukawa coupling scaling factor spoils the unitarity and renormalizability of the electroweak theory. However, it is shown in [7] that a value of $c_F = -1$ will lead to a breakdown in perturbative unitarity at a scale of $\Lambda \sim 10$ TeV. This is well above the centre-of-mass energies of partons created in the tH process at the LHC (these are typically at $\sim$ 1 TeV), which means that perturbative calculations of the tH cross-section for LHC collisions are expected to be sufficiently accurate.

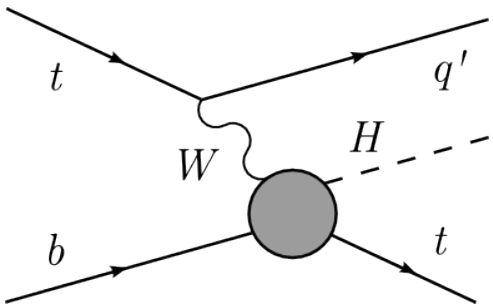

Figure 4: Feynman diagram of the core process $Wb \rightarrow tH$.

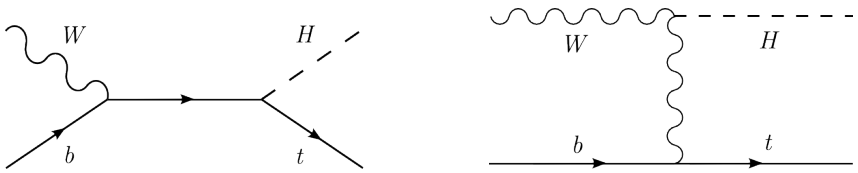

Figure 5: Feynman diagrams of the two major contributions to the core process $Wb \rightarrow tH$.

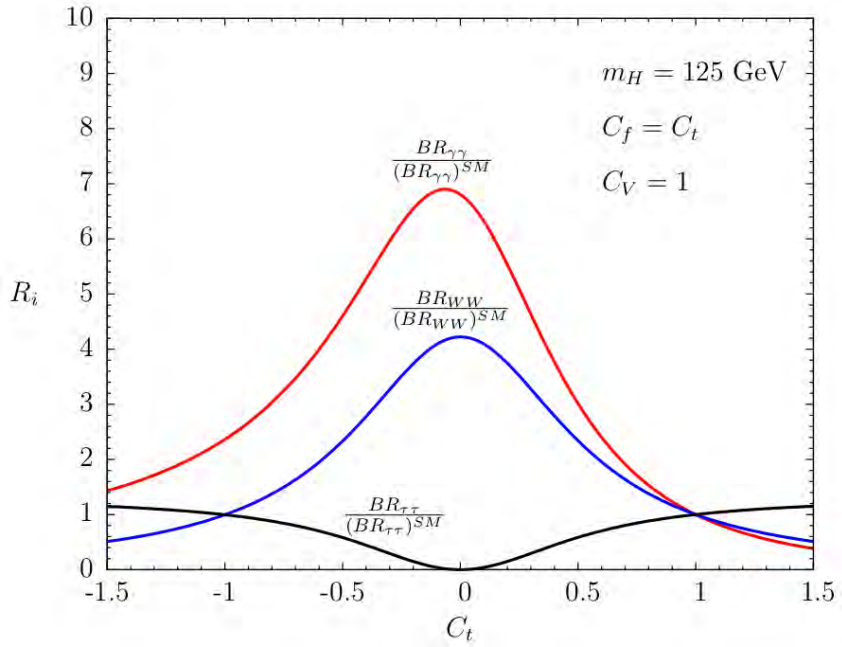

Figure 6: The branching ratios for the WW, $\gamma\gamma$ and $\tau^+\tau^-$ decay channels normalised by the SM branching ratio, for $\sqrt{s} = 8$ TeV. [19]

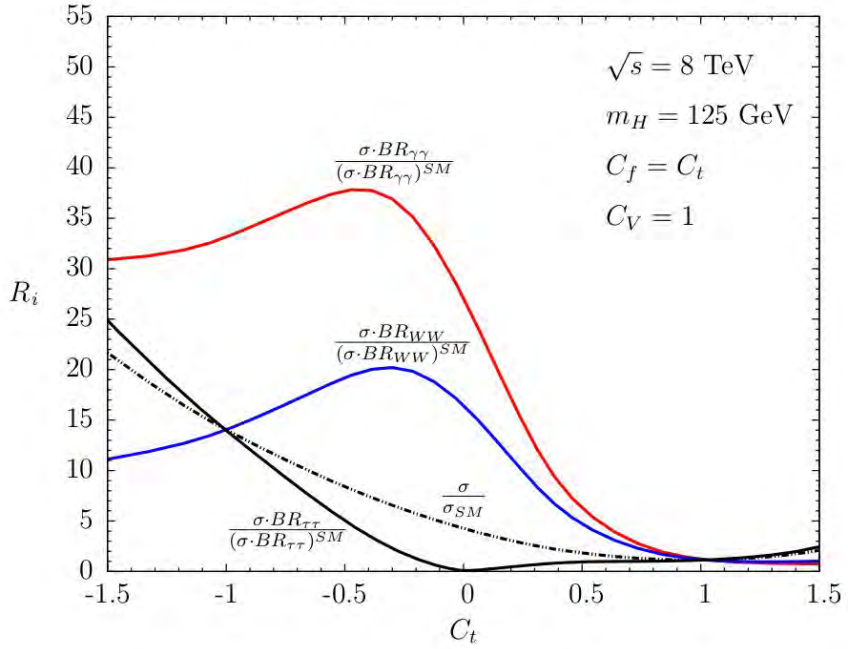

Figure 7: The event yields for the WW, $\gamma\gamma$ and $\tau^+\tau^-$ decay channels normalised by the SM event yield, for $\sqrt{s} = 8$ TeV. The dotted line is the cross-section of the $pp \to tHj$ process normalised by the SM value. Here, $c_V = 1$ and $c_t = c_F$.[19]

In Figure 6 the branching ratio (BR) for various Higgs boson decay channels are shown, normalised to the SM value, assuming $c_F = c_t$ and $c_V = 1$ (where c is the same as κ used by ATLAS and CMS). The

process with the strongest deviation is the $\gamma\gamma$ channel: Here, the BR is doubled for an inverted fermionic coupling value, $c_F = -1$. For the same configurations, Figure 7 shows the relation between c_F and the event yields for relevant processes as well as the $pp \rightarrow tHj$ (where j is an additional jet emitted during the tH production process) cross-section (the dotted line), all of which are normalised to the SM-value. The cross-section for the tH process for an inverted fermionic coupling would be 13 times greater than the SM cross-section. The event yield is also increased as a result of the branching ratio dependency.

For a detection of this signal, Higgs boson and top quark decay channels must be chosen. The top quark is required to decay leptonically to provide a lepton trigger signature (the meaning of "trigger" is explained in Section 4.1.4). The various Higgs boson decay channels have conflicting advantages and disadvantages. Whilst the two photon or leptonic decay channels ($H \rightarrow \gamma\gamma$, $H \rightarrow WW* \rightarrow \ell\nu\ell'\nu$ and $H \rightarrow \tau\tau \rightarrow \ell\nu\nu\ell'\nu\nu$) suffer little background, the relative small branching ratios mean that the signal acceptance is small. On the other hand, the $b\bar{b}$ channel has larger signal acceptance but suffers from significant backgrounds. Parton-level studies of the tH process via photon decay were presented in [18] where it was concluded that the first year of the 14 TeV run would be sufficient for an observation of a negative fermionic Yukawa coupling. In [19] these studies were extended to also include leptonic decay channels, in which it was concluded that an observation at 8 TeV was feasible if all data from ATLAS and CMS at 8 TeV for both channels are combined. CMS have published their results of an analysis using the $H \rightarrow \gamma\gamma$ signal at 8 TeV and 19.6 fb^{-1}. They stated an expected significance of $1.2 \pm 1.2\sigma$. Using the $m_{\gamma\gamma}$ distribution to search for an excess of events, they reported zero events passing their acceptance requirements and a 95% confidence level upper limit on the event yield containing Higgs boson decays to two photons and $c_t = -1$ corresponding to 4.1 times the expectation [20]. Doing a simple rescaling of their expected signal an integrated luminosity of around 100 fb^{-1} of data would be needed to reach a significance of 3σ.

Very recently, ATLAS published their measurements of the $\gamma\gamma$ cross-section via both the t$\bar{\text{t}}$H and tH channels, using the full 7 and 8 TeV datasets [21]. Even for this analysis, not enough statistics in the $H \rightarrow \gamma\gamma$ channel was reached. Upper limits were set which strongly constrained the negative Yukawa sector especially. They reported an exclusion limit at 95% confidence level at 6.1 times the SM cross-section, as well as lower and upper 95% confidence levels of the Yukawa coupling strength at -1.3 and +8.0.

The present analysis is based on the parton-level studies presented in [7] in which the Higgs boson decay channel studied is $H \rightarrow b\bar{b}$. They estimated that an inverted Yukawa coupling may be excluded at a 95% confidence level at 8 TeV centre-of-mass energy and 25 fb^{-1} of data.

3 The Large Hadron Collider

In 1994 the construction of the Large Hadron Collider (LHC) was approved by the CERN council.[22] Twenty years later the first run of the LHC High Energy project has been successfully completed and, after two years of upgrades, the project, the most powerful collider ever built, is now on the verge of commencing with a second run.
The underground tunnel which houses the LHC was initially built for the Large Electron Positron Collider (LEP). LEP was decommissioned in 2001 to make way for the new proton-proton and lead ion collider. The tunnel lies 100 m underground and circles under the French-Swiss border with a circumference of 27 km. It was built to collide high energy protons to produce heavier and a greater number of particles than ever seen before, out of which it was hoped that new fundamental particles would emerge; specifically the Standard Model Higgs boson. The LHC also collides lead ions to create an opportunity to study quark-gluon plasma, one of the densest matter in the universe. This matter is in a strongly-interacting colour-deconfined state akin to the state of the very early universe [23].

The LHC uses a system of magnets to accelerate and direct two separate beams of protons around the ring before focussing them to collide. One beam runs clockwise and the other anticlockwise. The injection of the two beams happens through an elaborate *injection chain* (refer to Figure 8) which steps up the proton energies in stages. The source of protons is a tank of hydrogen gas at the beginning of Linac 2, a linear accelerator and the first accelerator in the injection chain.
The hydrogen is passed through an electric field to strip protons of their electrons. The protons are then accelerated to 50 MeV before entering the Proton Synchrotron Booster (PSB) which increases their energy to 1.4 GeV. The Booster was inserted to prevent lag in the chain between Linac 2 and the succeeding accelerator, the Proton Synchrotron (PS). The PS accelerates the protons to 25 GeV before they are directed to the final accelerator in the injection chain, the Super Proton Synchotron (SPS). The SPS steps up the energy to 450 GeV before the beams are injected to the LHC for a final charge up and subsequent collisions.[22]
The protons are injected and collided in bunches in order to maximize the probability of individual protons colliding. During Run I, each bunch held 1.6×10^{11} protons and were 50 ns apart [25]. Once the particles reach the maximum energy, the bunches are directed towards interaction points centred in detectors where some protons within the bunches collide. During Run I, the mean number of events that took place during each bunch crossing (that is, when two bunches of protons, one from each proton beam, cross at the interaction point) was 20 [25]. The frequency of proton collisions in a detector was thus at around 400 million per second.
The injection of lead ions for the ion collision runs can be similarly followed in Figure 8. In this case, the ion beams are initiated in the linear accelerator, Linac 3.

The construction was completed in 2008 after which many test beam runs followed. The first run, or

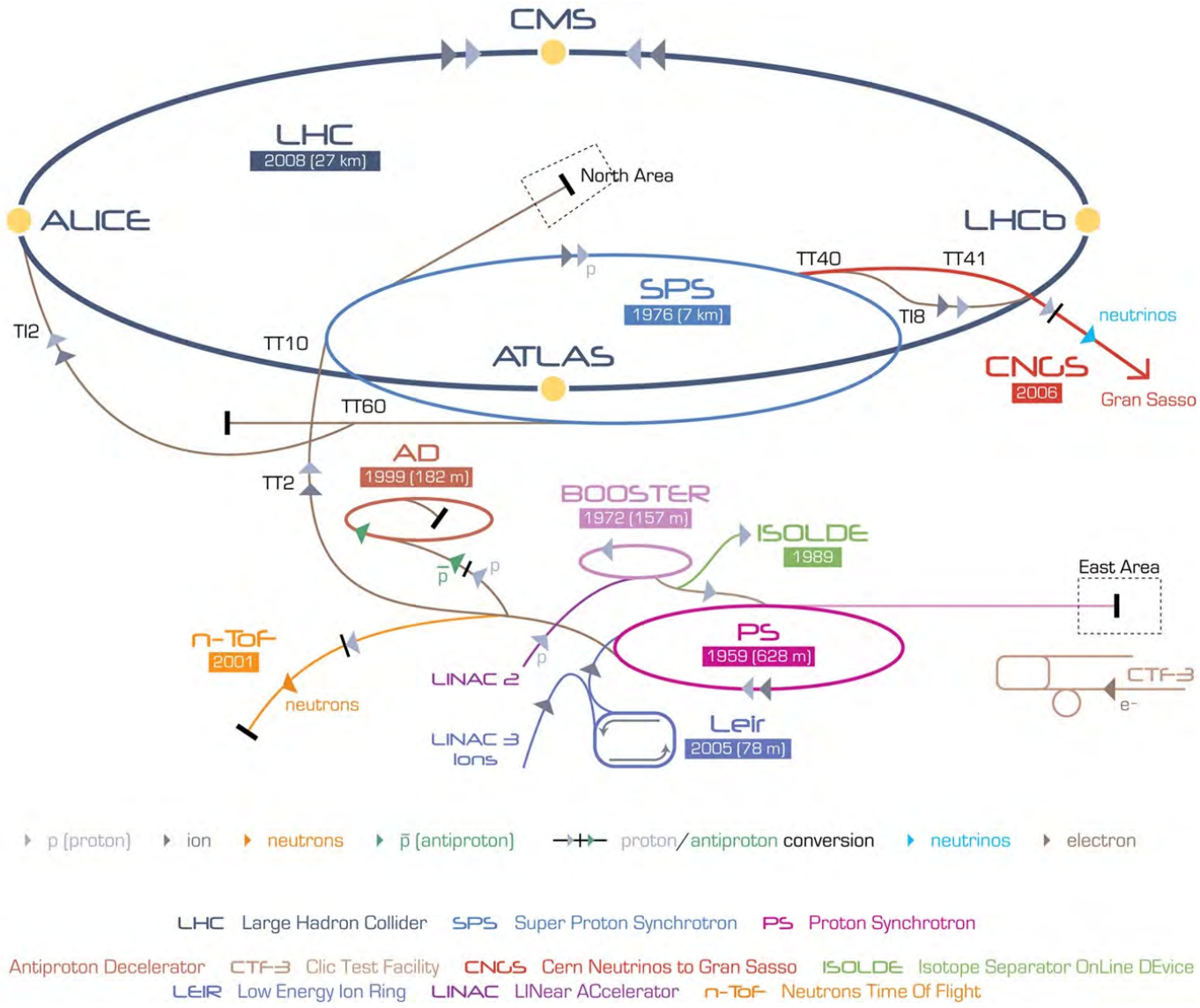

Figure 8: A diagram of the LHC and its injector systems. Protons are injected through Linac 2 → PSB → PS → SPS. The beams are then injected into the LHC through the transfer line TI2 and TI8. ATLAS and CMS are the two general-purpose LHC experiments that measure proton-proton collisions. Proton-proton beams are thus made to cross each other at these two diametrically opposite interaction point.[24]

Run I, was performed during 2011 and 2012, colliding protons at 7 and 8 TeV centre-of-mass energies ($\sqrt{s}$) respectively. A total integrated luminosity of roughly 25 fb^{-1} was achieved. The run reached its pinnacle of success with the discovery of a Higgs boson. Other achievements were the detection of a new composite particle, a bottomonium meson, through proton-proton collision [26] and a further understanding of quark-gluon plasma in heavy ion collisions. Although the top quark had already been observed at Fermilab, the most prominent particle physics laboratory in the United States, in 1995 (add ref!), the LHC is like a top quark factory, allowing the analysis of its spin and couplings.
Run II will begin in 2015, stepping up the proton-proton collision to 14 TeV centre-of-mass energy and reducing the bunch spacing to 25 ns. Up to 100 fb^{-1} of data will potentially be accumulated.

4 Experimental Tools at the LHC

There are four large detectors in total around the beam line, labelled at the yellow points in Figure 8.
Largest are the two general-purpose detectors, ATLAS (A Toroidal LHC ApparatuS) and CMS (Compact Muon Solenoid), studying proton-proton collisions for new physics. A large motivation for their construction was the search for the Higgs boson, as well as the search for supersymmetric particles. They also aim to measure Standard Model parameters with higher precision than previous experiments.
ALICE (A Large Ion Collider Experiment), roughly half the size of ATLAS, is dedicated to studying QCD processes through the collisions of heavy nucleii. The experiment also uses proton-proton collisions to collect reference data. The collisions result in a quark-gluon plasma, an extremely hot phase in which quarks and gluons are deconfined. This is believed to be a state that existed at the very early universe prior to a phase transition towards the formation of hadrons as the universe cooled down. Photons emerging from this highly dense and hot state allow the study of thermal radiation from the early phase of the universe.[27]
The Large Hadron Collider beauty (LHCb) experiment is dedicated to the search for rare decays of bottom (beauty) and charm hadrons. The studies into heavy flavour physics should give new insights into the matter-antimatter asymmetry of the universe, known as CP violation.

The studies presented herein are performed with the ATLAS experiment. Subsequently, the rest of this section gives further details on the ATLAS detector and analysis tools specific to ATLAS.

4.1 The ATLAS Detector

A cut-away view of the ATLAS detector is shown in Figure 9. Its general shape is that of a barrel, 44 m in length, with two end caps on either end, 25 m in diameter. The 36 mm diameter beam pipe runs along the z-axis of the cylindrical geometry.

The following detector coordinate directions are applied: the $z-axis$ is the beam axis; $x-$ and $y-axes$

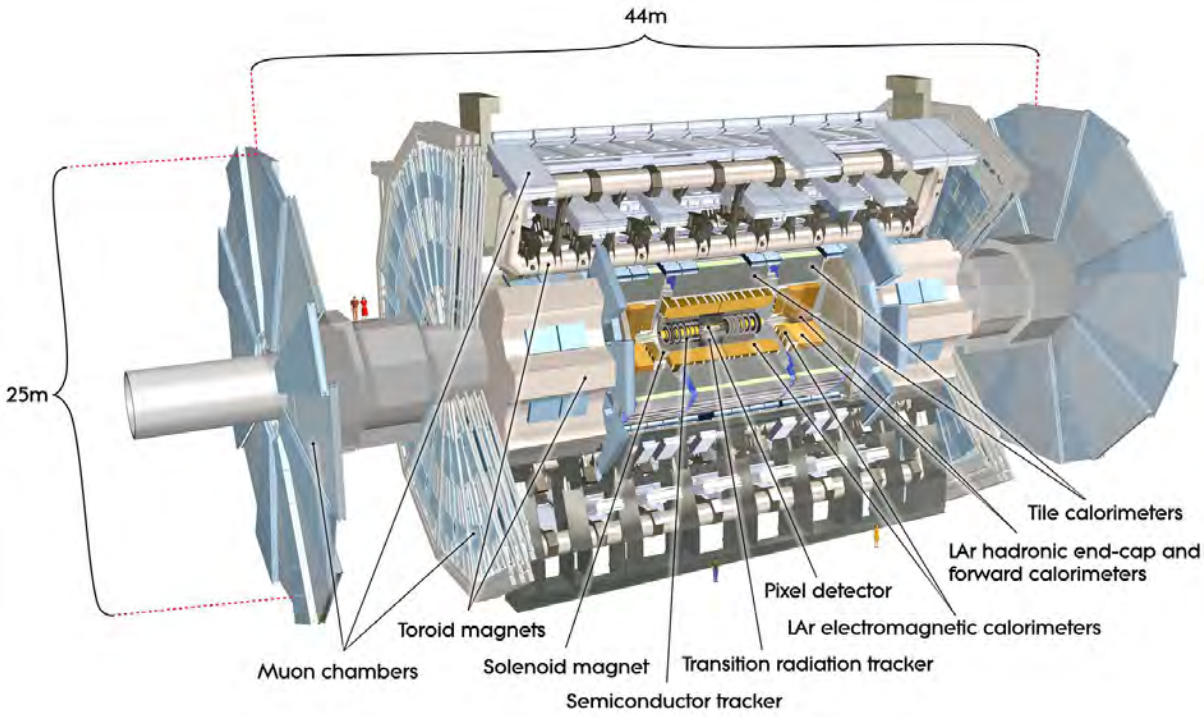

Figure 9: A labelled cut-away view of the ATLAS detector layout showing all of the subcomponents.[28]

define a plane perpendicular to the beam axis; ϕ, the azimuthal angle and θ, the polar angle. The positive x direction is defined as from the interaction point to the centre of the ring and the positive y direction as upwards. Generally, θ is expressed in terms of *pseudorapidity*, η = -ln[tan(θ/2)]. The value for η will thus range from 0 perpendicular to the beam axis to = $\pm\infty$ along the beam axis. Detection of particles extends down to roughly $\eta = +/-4.9$. A commonly used distance is ΔR, the distance in the $\eta - \phi$ plane defined as $\sqrt{\Delta\eta^2 + \Delta\phi^2}$. Since particle hits lie in the $\eta - \phi$ plane, it is the transverse momentum, p_T, of the particles that the detector measures.

The detector needs to serve several purposes, with high precision, some of which are: identifying and measuring electrons and photons (using electromagnetic calorimetry), measuring jets and missing transverse energy (using hadronic calorimetry), measuring muon momenta (using muon spectrometry), perform efficient tracking of particles (using a tracking system) and have large acceptance coverage (a large η and almost all-around ϕ coverage). Figure 10 is a display of an actual event recorded at ATLAS. Calorimetry cell signals and tracks are clearly evident with an even ϕ distribution.

Two issues which complicate measurements in ATLAS are pile-up and the underlying event. Pile-up is additional proton collisions that occurred during the same bunch crossing, emerging particles of which will overlay the physics event of interest. At 20 interactions per bunch crossing, this becomes a serious background. The event displayed in Figure 10 contained 25 detected proton collisions. It gives one an

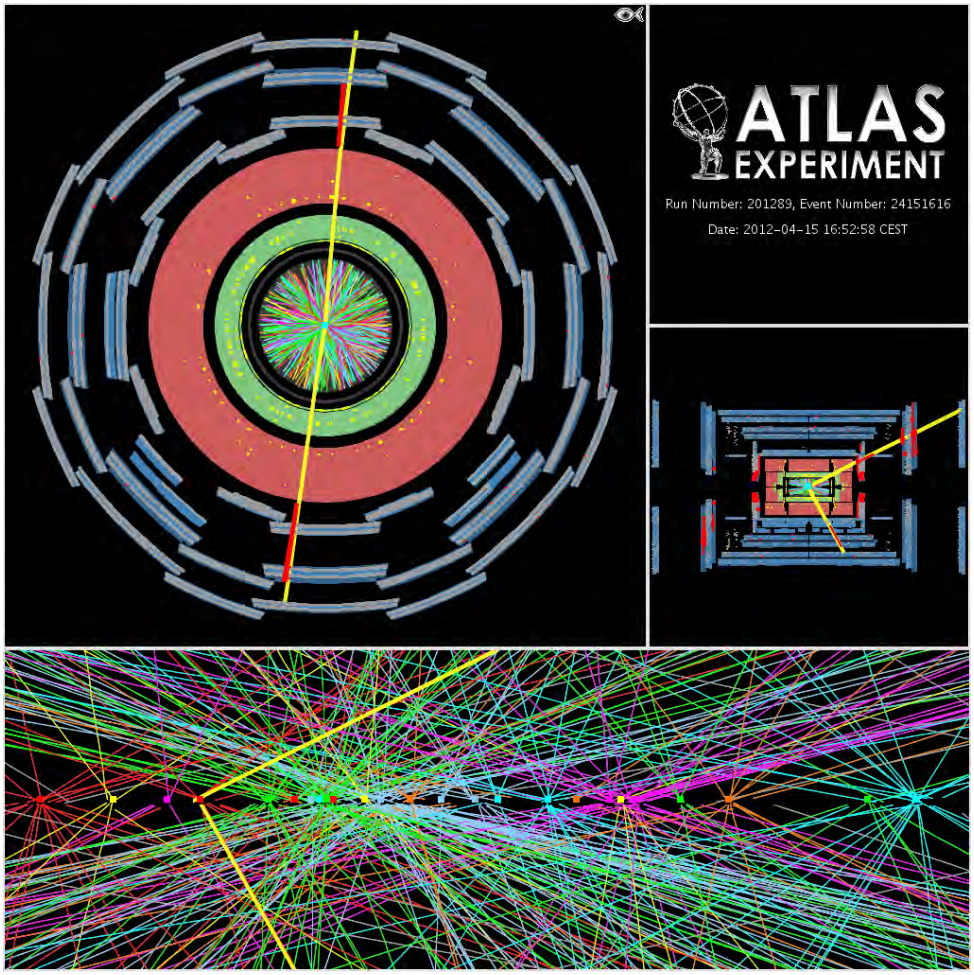

Figure 10: A display of an actual event recorded at ATLAS in 2012. It is a $Z \rightarrow \mu\mu$ candidate: the two muon tracks are clearly evident. A total of 25 reconstructed primary vertices were detected, demonstrating the large pile-up effects in the 8 TeV collision environment.[29]

idea how convoluted the environment becomes under pile-up.

The underlying event contains particles that are created in addition to the hard core process of the physics event of interest, such as radiated gluons or particles from the interaction of a separate pair of partons from the colliding protons.

Another issue is the large amounts of events that cannot all be recorded for offline analyses. Ultimately, out of the 400 million events that take place per second, only 200 are retained for offline physics analysis. It is thus attempted to select 'interesting physics' events in real-time through a trigger system. The trigger system begins with a coarse search of an event at real time for features such as high momentum signals or a great amount of missing energy. The event selection is then refined offline using higher resolution information. Further details are given in Section 4.1.4.

To be able to perform the tasks outlined above, the detector consists of several subdetectors which are

labelled in Figure 9 in a cut-away view. Starting at a radius of 51 mm around the beam pipe lies the *Inner Detector* (ID). This component is used for the measurement of particle tracks within $|\eta| < 2.5$ with high precision as the particles pass through. It is surrounded by a solenoid that immerses it in a magnetic field and bends particle trajectories.
Outside of the solenoid lie the calorimetry components for the energy measurements of all particles except for muons and neutrinos. The calorimetry system covers a wide η range, up to $|\eta| < 4.9$ and is therefore also sensitive to forward radiation. The particles will deposit (most of their) energy in the high-granularity calorimeter cells. Cells with energy deposits of a particle are then 'clustered' (refer to the *'Topological Clustering Algorithm'* in Section 4.3.2) to obtain the total sum of the particle's energy. In the case of hadrons, the clusters within the calorimeter are subsequently used to reconstruct the hadron shower that results due to colour-confinement (refer to the explanation of *'Jet Reconstruction'* in Section 4.3.2).
Enveloping the inner detector and calorimetry components is the muon spectrometer. Part of the muon detection system are three large superconducting toroids. There is a large space between the magnets and the muon calorimeter within which the paths of muons are greatly bent by the magnetic field.
Both the calorimeter and muon system have coarse-granularity components for triggering.

The signature of the tH process studied in this thesis requires an electron or muon to trigger the event. Muon identification and momentum measurements are performed in the muon spectrometer, whilst for electrons these measurements are performed in the electromagnetic calorimeter. Another signature of the process are the four jets (three b quark jets and a forward jet) identification, precise momentum measurements of which are done in the inner detector. Finally, my work related to particle flow is strongly focussed on processes in the calorimeter. Therefore an overview of the inner detector, muon spectrometer and the trigger system, as well as a more detailed description of the ATLAS calorimeter, are presented in this section.

4.1.1 The Inner Detector

The high energies and luminosity at the LHC results in a high density of particle trajectories, many of which are heavy flavoured hadrons. Due to pile-up, these can originate from different proton collisions. A fine resolution is therefore required in order to identify individual tracks and extrapolate them back to their point of origin. This point is either the proton collision point (the primary vertex) or the decay point of a heavy hadron or τ lepton that emerged from the proton collision (a secondary vertex).

The Inner Detector, a 1.1 m in radius and 3.5 m in length subdetector, is dedicated to measuring charged particle tracks. The inner component of the ID is constructed very closely around the beam pipe, its first layer located at 51 mm radius around the 36 mm radius pipe. The close proximity is required in order to be able to extrapolate to the primary vertex with little ambiguity. Additionally it is required

for the measurement of secondary vertices of heavy (bottom or charm) flavoured hadrons which are expected to decay in the very inner region of the ID. The position of the secondary vertex depends on the expected lifetime of the hadron. Locating secondary vertices is thus a means of identifying hadrons and their flavours. A central superconducting solenoid providing a 2T magnetic field surrounds the ID. The magnetic field is required as it bends particle trajectories. The direction and degree of bending allows us to extract the particle's charge and momentum.

High resolution momentum and vertex measurements are obtained for charged tracks with $p_T > 0.5$ GeV and in the $|\eta| < 2.5$ range. Additionally, electron identification can be performed for tracks within $|\eta| < 2.0$ and 0.5 GeV $< p_T <$ 150 GeV.

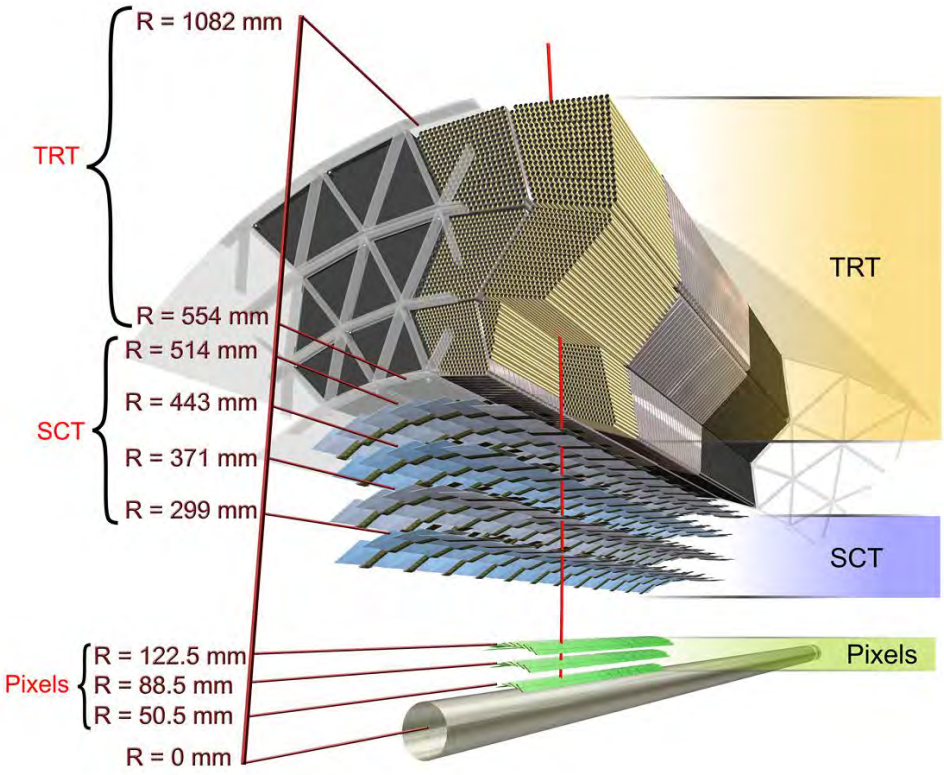

Figure 11: A labelled cut-away view of the ATLAS Inner Detector is shown. The pixel detector and the Superconducting Tracker (SCT) are made of silicon pixels and strips for high-precision track measurements. The Transition Radiation Tracker (TRT) uses straw tubes of gas for lower-precision but continuous track measurements.[30]

The different components that make up the ID are shown in Figure 11. Measurements in the very inner region are done by the pixel detector comprised of three layers of high-granularity superconducting

silicon pixels. The high granularity is essential for vertex measurements. Further out is the Superconducting Tracker (SCT), comprised of four layers of silicon microstrips. Both components consist of a barrel made up of concentric cylinders and rings in the endcap region, orientated perpendicular to the beam axis (refer back to Figure 9).
In the outer region lies the Transition Radiation Tracker (TRT) which makes use of 4 mm in diameter straw tubes. These are arranged parallel to the beam axis in the barrel region (in roughly 36 layers) and radially in wheels in the endcap region which extends down to $|\eta| = 2$. The measurements performed by the TRT are of lower precision and only give information in the R and ϕ direction. However, due to the greater number of layers, it receives more hits than the inner region, offering a more continues track measurement. Furthermore, the high transition radiation that occurs through interaction of highly relativistic particles with the straw tube gas is used as a means of identifying electrons and positrons.[31] Ultimately, all hits in the ID are used as input to a track fitting algorithm [32] to reconstruct tracks.

4.1.2 The Calorimeter

A calorimeter in particle physics works by initiating a particle shower and absorbing these particles in the instrument's so called absorber material. A second type of material - the active material - detects the energy from the shower and sends as output an electronic signal that is proportional to the incident energy. The calorimeter is non-compensating, meaning the measured energy falls short of the true energy and needs to be corrected for, using calibration methods.
The ATLAS calorimeter is a subdetector that is located between the inner detector and the muon detector. It has in total approximately 100 000 cells [33] and measures the energies of charged as well as neutral particles by recording the energy deposited within these cells. The calorimeter has several components, which are needed for both electromagnetic and hadronic calorimetry. The electromagnetic calorimeter components are there for the detection of particles that interact electromagnetically. These are mainly electrons and photons. The hadronic calorimeter components detect particles that interact via the strong force. These particles are mostly hadrons formed from the hadronization of a quark or gluon. The interaction length of a hadronic shower is much larger than the radiation length of an electromagnetic shower, which leads hadronic calorimetry to be deeper and denser.

There are two types of calorimeters in the ATLAS detector: the liquid argon (LAr) calorimeter and the tile calorimeter (TileCal). The LAr calorimeter measures particle energies through the ionisation of secondary electrons in the active material (liquid argon) that had come from the developing shower in the absorbing material. The tile calorimeter measures energies using the emitted light from scintillation tiles and uses steel as the absorbing material.

The liquid argon (LAr) calorimeter is described in detail in [34]. It has electromagnetic (EM) calorimetry covering the region $|\eta| < 3.2$ using lead as the absorber material and hadronic calorimetry covering the

more forward region $|\eta| = 1.4$ to 4.8 (the acceptance level) and using copper as the absorber material.
The EM calorimeter component in the LAr calorimeter consists of a barrel and an EM wheel in the so-called endcap calorimeters, which are situated in the forward regions of the detector.
Their construction makes use of an interesting design of accordion-shaped lead plates of electrodes, which gives an unbroken ('no cracks') surface all the way along the azimuth direction. The barrel calorimeter acts in the central $|\eta| < 1.4$ region and is barrel-shaped but split into two identical half-barrels, leaving a gap of a few millimeters between them. The EM wheel actually consists of a bigger and smaller wheel, which cover the range $|\eta| = 1.4 - 2.5$ and $|\eta| = 2.5 - 3.2$, respectively. The barrel and the big EM wheel each have three sampling layers and the small EM wheel has only two (due to precision physics not being achievable at this η range). A schematic of the three sampling layers of the EM barrel calorimeter at $\eta = 0$ is displayed in Figure 12. The sampling layers are of varying granularity ($\delta\eta \times \delta\phi$) and are finest in the central η region. The finest granularity is $\delta\eta \times \delta\phi = 0.025 \times 0.025$ in the middle layer at $\eta < 1.8$, where most of the energy is deposited.
Due to the amount of material in front of the barrel (e.g. the solenoid), a presampling layer is needed to correct for the energy that is absorbed before it reaches the barrel. The triggering system of the calorimeter (also shown in Figure 12) is maintained in a last layer - trigger towers of a broad $\delta\eta \times \delta\phi = 0.1 \times 0.1$ granularity. They trigger on high p_T electrons, photons and jets.
The hadronic component of the LAr calorimeter consists of one wheel in each endcap which are simply made up of parallel copper plates and together cover the η range $1.4 - 3$. Since hadronic shower shapes are wider, the hadronic component has a coarser granularity than the EM component, the finest being 0.1×0.1. Finally, there is the forward calorimeter that covers the very forward and *highest*-radiation η region $3 - 4.8$. The absorber mediums are copper and tungsten. Tungsten was chosen for its high density as this would limit the sizes of the showers and reduce leakage to the surrounding calorimeter components.

The tile calorimeter lies in the outer parts of the calorimetry component and its role is to measure the energies of more centrally placed hadronic jets. It makes use of steel as the absorbing material and scintillation plates that are arranged in planes lying perpendicular to the beam. The calorimeter is made up of a central barrel covering the $|\eta|$ range < 1.0, and two extended barrels, one on each side, covering the $0.8 < |\eta| < 1.7$ edges. The tile calorimeter has two sampling layers all around. Its granularity - of 0.1×0.1 - is not as fine as the LAr calorimeter.

4.1.3 The Muon Spectrometer

The muon spectrometer (MS) lies at the outer part of the ATLAS detector. It performs high-precision tracking measurements for charged particles that have passed through the ID and the calorimeter and through the magnetic field of the spectrometer. Its acceptance range is $|\eta| < 2.7$. The only type of charged particle capable of propagating so far out from the interaction point is the muon. This is due to

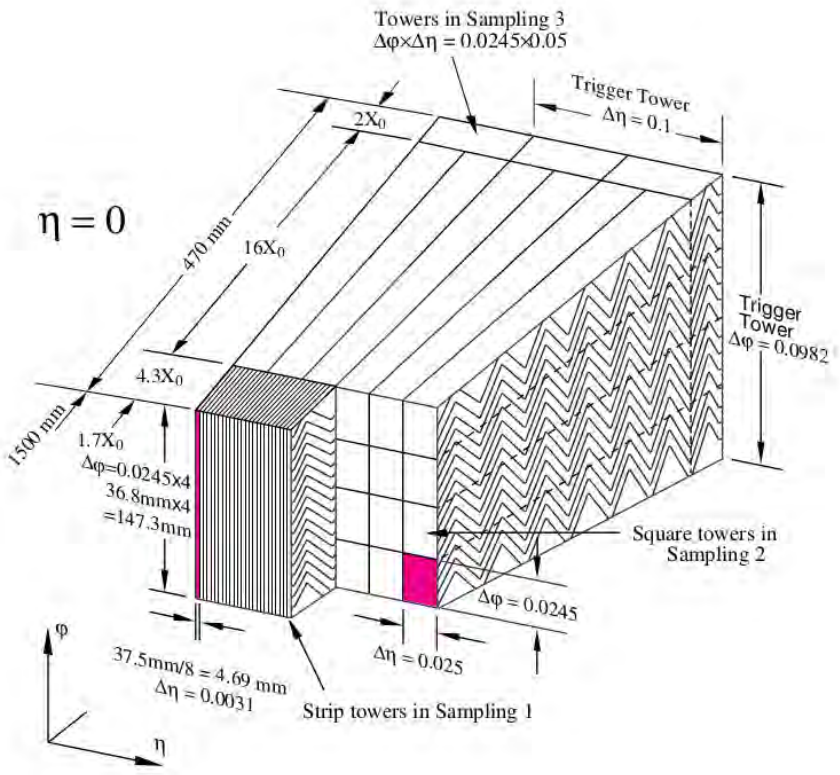

Figure 12: A schematic of the sampling layers in the EM barrel calorimeter (Figure 1.2 in [34]) at $\eta = 0$. Its accordion structure and its granularity is clearly drawn out. Sampling layer 1 consists of $\delta\eta \times \delta\phi = 0.0031 \times 0.1$ towers. Its fine granularity in $\delta\eta$ mainly serves to reject π^0 particles. Sampling layer 2 is where most particles of interest will deposit their energy. A fine granularity in both directions, $\delta\eta \times \delta\phi = 0.025 \times 0.025$, was thus chosen. Sampling layer 3 is somewhat coarser ($\delta\eta$ is increased to 0.05) to limit the total number of channels. Trigger towers cover the outer layer of the barrel with a coarse granularity of $\delta\eta \times \delta\phi = 0.1 \times 0.1$

its relatively long lifetime (it decays only weakly) and the small energy loss when passing through the detector material, unlike the lighter electron. Part of the muon spectrometer is a magnetic configuration of three large toroidal magnets– one envelopes the barrel region and the other two, of smaller radii, are inserted at the endcaps and within the barrel toroid. The magnetic field strength varies between $0.5 - 1$ T. Precision-tracking chambers are arranged in three cylindrical shells around the barrel region. The outer shell lies at a 10m radius. Chambers in the endcap region form three large wheels, the furthest lying at 21m from the interaction point. The barrel toroid extends out to a radius of 20m, and extends 12.5m from the interaction point either way. The toroid magnet therefore shapes the overall barrel region, whilst the endcap muon chambers, located outside of magnet system, determine the total length of the ATLAS detector (refer to Figure 9). In addition to this, the system houses fast trigger chambers that send out track information as soon as the passage of a particle is detected within $|\eta| < 2.4$. This acts as part of the trigger system of the detector.[31]

4.1.4 The Trigger System

As mentioned earlier, not all events are retained for offline analysis. An interesting feature, i.e. a trigger, must exist in an event for the system to decide to keep it.
The trigger system works in three stages. The Level 1 trigger coarsely analyses an event at real time in search for a certain signal. This is either a high p_T electron, muon, tau or jet, or a large amount of missing energy. The Level 1 analysis works with the measurements from the trigger towers in the calorimetry and muon systems. If it finds an interesting signal, it establishes the 'region of interest'. Information on the 'region of interest' is then sent to the Level 2 trigger. Each event is processed in less than $2.5\mu s$. The Level 2 trigger does a refined analysis of the 'region of interest' using fully reconstructed data. This is executed in around $40ms$ and if it confirms the trigger signal, the event is passed on to the event filter. Here all information in the event is analysed offline thoroughly at four seconds per event. In the end, of the initial 400 million events per second, an average of 75 000 will pass through Level 1, 3500 through Level 2 and only 200 events will eventually pass through the event filter to be stored on tapes at CERN for physics analysis by scientists.
Electron and muon triggers are more common than tau triggers as electrons and muons are cleaner signals. The reduced background means they can be triggered at a lower p_T.

4.2 Monte Carlo Event Generation & Simulation

Monte Carlo (MC) generation of collision events are the basis of any analysis. They aim to generate as accurately as possible particle collision events the results of which are not simple $2 \rightarrow 2$ particle productions: there will be bremsstrahlung, virtual particles and hadronisation so that a cascade of multiple hadrons, photons and leptons results. Also, processes are of a probabilistic nature, and for this Monte Carlo event generators are useful as they work by making 'random' decisions. MC event generators serve a myriad of purposes. Mathematical calculations become highly complex and at some point non-perturbative when describing a hard collision and this description is impossible to draw out 'by hand'. Non-perturbative effects have to be modelled instead.
Event generation thus give physicists an idea on the event rates and distributions to expect - this is good to judge the feasibility of working with a process, as is done in the work of this thesis. Generators allow us to simulate possible background so that analysis strategies can be formed around discrepancies between signal and background. They offer us a framework - usually based on the Standard Model - to compare to what is observed in real data, so that we can confirm expectations or seek deviations.

There exist several Monte Carlo generators, some of which are general-purpose and all-inclusive and others are specialised. A general-purpose generator will include hard and soft interactions, formation of parton showers and hadronisation. Specialised generators are used for example for the computation of NLO hard scatter processes, for the simulation of background processes only, multiple parton processes

or pile-up, among others.

Monte Carlo methods are further used for detector simulation. Events are generated and interfaced with a detector, so that the event now looks like how we would observe it in the real detector. These MC simulations have several purposes: they are an aid for optimizing the detector where most of the interesting physics happens; to study detector imperfections so that acceptance factors can be evaluated; or finally, to study the response of the detector so that real data can be scaled, or 'unfolded', to particle level.

The difference between an MC event generator and event simulator, is that a generator gives information at *truth* level, and a simulator gives information at a *reconstructed level*. At truth level, particles are as generated from the collision. At reconstructed level, particles are reconstructed from simulated detector signal (e.g. calorimeter hits, tracks...) and are therefore affected by detector and reconstruction inefficiencies.

Most Monte Carlo samples used in this analysis were generated using a general-purpose MC simulator called Pythia [35], together with MadGraph [36], which provides a leading order (LO) Matrix Element generator. The exception are the samples of the $t\bar{t}$ process. Due to its large cross-section and 1 and 2 lepton signatures, this process is commonly used for comparison and calibration studies. It is the biggest background in the analysis and was generated likewise with Pythia, together with POWHEG[37], a next-to-leading-order (NLO) Matrix Element generator.

4.3 Physics Analysis

Physics analysis in ATLAS is completely based on statistics. In order to claim an observation of a process, a certain number of events above expected background events must be observed. The number of expected events of a particular particle interaction can be expressed as

$$N = \mathcal{L} \times \sigma \times \varepsilon \times A. \tag{9}$$

Here, $\mathcal{L}$ is the total integrated luminosity: the total number of proton-proton interactions, at a particular collision energy, per area, that occurred during the period of data collection. The number of events are proportional to the cross-section, σ, of the process. The cross-section has units of area and is the probability of the process of interest occurring. The value $\mathcal{L} \times \sigma$ will thus be the total number of proton collisions expected to have produced this process. The efficiency, ε, and the acceptance, A, are detector and reconstruction effects. Inefficiencies related to particle detection and reconstruction will necessarily lower the number of events. Some particles are not detected because they fell into inactive regions, such as gaps in the detector, or were absorbed by 'dead' material. 'Dead' material is all material that lies between detector components and does not make detections, e.g. the magnets and cryostats. This will

lower the 'acceptance' and N. Finally, when a particular process is searched for, certain acceptance criteria are applied to all events in order to extract the relevant events from background events. This further lowers the acceptance.

To quantify the significance of the number of signal events (S) observed over the number of background events (B), one assumes a background-only hypothesis. This means the expected mean number of events is B with a standard deviation of $\sigma_{stat} = \sqrt{B}$, assuming Poisson fluctuations. The p-value for an observation of $N = S + B$ events in a background-only hypothesis is

$$p = 1 - \Phi(\frac{N-B}{\sqrt{B}}), \tag{10}$$

Where $\Phi(\frac{N-B}{\sqrt{B}})$ is the cumulative distribution function for the background-only normal distribution: effectively the area of the distribution from negative infinity to N.
The significance of this is the z-value,

$$\begin{aligned} Z &= \Phi^{-1}(1-p) \\ &= \frac{N-B}{\sqrt{B}} \\ &= \frac{S}{\sqrt{B}}. \end{aligned} \tag{11}$$

This defines the significance of an excess of events above the expected background. As this holds for $S << B$, it is sufficient for the present feasibility study[2]. An approximate way of including systematic uncertainties in the background estimation is by taking the quadratic sum of the statistical and systematic uncertainties, $\sigma^2_{total} = \sigma^2_{stat} + \sigma^2_{sys}$. The significance then becomes

$$Z = \frac{S}{\sqrt{B + \sigma^2_{sys}}}. \tag{12}$$

In particle physics, a significance of 3σ is defined as 'evidence' of a signal, and a significance of 5σ an 'observation'. The events signifying the Higgs boson discovery in 2012 were observed with significance values of 5.9 (expected 4.6) and 4.9σ (expected 5.9) by ATLAS and CMS respectively with 10 fb^{-1} of proton collision data. [1, 2]

As indicated in the description of ATLAS subdetectors in the previous section, different types of particles interact with different regions of the detector. Various methods and algorithms exist to reconstruct these different types of particles as they leave signal (or even lack of signal) signatures.

[2]For a more accurate value, one would use a formula based on the likelihood ratio test, $\sqrt{2(S+B)ln(1+\frac{S}{B}) - 2S}$.

The different types of signatures used in ATLAS are electrons, muons, photons, hadrons, and undetected particles. All other types, such as taus, W bosons and Z bosons are detected via their decays into one of these types of particles.
Particles need to be reconstructed as objects for analysis from the signal they leave in the detector. Electrons, photons, and hadrons are reconstructed using the energy deposited in the calorimeter cells, via the *sliding-window* algorithm or the *Topological Clustering Algorithm* (Section 4.3.2). If identified in the central region, their origins (the initial proton collision or the decay point of a parent particle) are established by associating the tracks measured in the inner detector to the reconstructed object in the calorimeter. Hadrons are further used in the reconstruction of *jets* (an object that represents the hadron shower initiated by a free quark) using a jet reconstruction algorithm. Muons are reconstructed using combined tracking information in the muon chambers and the inner detector. Finally, neutrinos or unknown invisible particles are reconstructed through the missing energy: the negative vector sum of the transverse energies of all particles that were detected and any additional unclustered energy in the calorimeter.

4.3.1 Leptons and Photons

Electrons, taus and photon measurements are obtained from the calorimeter, and the muon measurements from the muon chamber. Except in the case of photons, further measurements are obtained from the tracker. In an attempt to gather all calorimeter cells that contain the energy of a particle that has interacted with the calorimeter, a clustering algorithm is used. For central electrons, this is the *sliding-window* algorithm. A *seed*, i.e. a group of cells with a significant amount of energy above the expected energy, is found with a window of dimensions equal to the granularity of the middle EM calorimeter layer. Any tracks for which the extrapolated coordinates are within $\delta\eta < 0.05$ and $\delta\phi < 0.10$ of the window are identified. An electron is reconstructed if at least one track is associated. The reconstruction efficiency for electrons above 25 GeV is between $85 - 95\%$.

Cluster and associated track information are used to identify/distinguish between the different types of particles.

Lepton Identification

Electron and photon identification is based on various methods, ranging in complexity, and depending on the strictness of selection criteria, the p_T values and the η values. However, the simple idea is outlined in the following.
Criteria are based on shower shapes, track matching, number of vertices and number of hits in the various parts of the ID. The shapes of clusters formed by electron and photon hits are typically more narrow and shorter compared to clusters from hadrons. Furthermore, they are concentrated in the EM layers of the

calorimeter. Electrons are distinguished from photons by using track information in the ID. Track vertices are located to distinguish photons that have converted to an electron positron pair after the collision. Tracks are extrapolated to the middle EM layer and associated to any clusters lying nearby. Additionally, the ratio between the energy measurement of the cluster and the momentum measurement of the track, E/p, can be computed to see if they match. If an EM cluster has no track associated to it, it is identified as a photon, but if there are associated tracks that moreover lead back to a secondary vertex, it is identified as a converted photon. Transition radiation in the TRT is a good indication of an electron and so requiring a certain number of hits in the TRT is also a way of identifying electrons.

Muons are reconstructed and identified using various methods. The simplest uses hits in the muon chambers to reconstruct the track which is then extrapolated straight to the beamline. Another method is to attempt to match a muon chamber track to a track measured in the ID and then combining the track measurements. Alternatively, a track in the ID can be extrapolated to the muon spectrometer to seek any nearby hits.
The advantage of only using the muon spectrometer hits is that the measurements are not limited by the slightly narrower η coverage of the ID. However, muons from hadron decays in the calorimeter and of no importance to the main physics process will be accepted. These contribute to the fake muon rate. Conversely, low p_T muons of interest which do not have enough energy to penetrate into the muon spectrometry region, will *not* be accepted, lowering the true muon acceptance rate.

Uncertainties from the measurement of electrons and muons result from trigger and identification efficiencies. Generally in well instrumented areas of the detector, the efficiency uncertainties are expected to be on the order of $\sim 1\%$. There is an additional uncertainty in the scale and resolution of the electron or muon p_T at a sub-percent level. Uncertainties in electron and muon measurements are consequently negligible.

Tau lepton identification is more complicated. Taus are heavy enough to decay hadronically, which they do 65% of the time. Their decay products mostly include a neutrino and an odd number of pions. Products from leptonically decaying taus are almost indistinguishable from prompt electrons and muons and the reconstruction efficiency is hence very low. These types of taus are thus usually not included in analyses. Hadronically decaying taus can look similar to QCD jets as they also deposit their energy in the hadronic calorimeter. They however produce narrower shower shapes, and furthermore have a distinct number of tracks associated to them if they have decayed to charged pions. Taus with only neutral decay products are not reconstructed. The QCD background leads to low rejection factors and subsequently tau reconstruction efficiencies that are considerably worse than for electrons, photons and muons. The rejection factor for the identification of final state taus varies with the number of associated tracks. The high end of the rejection factor is around 10 for 1-track taus with loose selection criteria and a target

efficiency of 70%. This can be increased to 500 for multiple-track taus with tight selection criteria and a target efficiency of 35% [38].

4.3.2 Hadron Showers

Hits in the hadronic calorimeter are clustered via the Topological Clustering Algorithm. Each cluster is then used as input for jet reconstruction – i.e. the reconstruction of a hadron shower initiated by a quark or gluon. It was already discussed in the previous section how tau jets are distinguished from quark and gluon jets.

The energy and direction of the initial quark is extracted from the reconstructed jet. Determining the flavour of the quark is important for physics analysis such as the $H \rightarrow b\bar{b}$ decay. As mentioned earlier, top quarks will decay before they hadronise, and so their flavour is determined through their decay products which is largely $W + b$. Light flavoured quarks are easily distinguished from bottom and charm quarks because of the relatively large difference in lifetime, which leads to a displaced vertex that can be identified. Distinguishing charm from bottom quarks is however more complicated. A b-tagging algorithm is used to 'tag' jets as b flavoured. Here, a compromise needs to be made, as a higher b-tagging efficiency is necessarily met with a higher c-*mistag* efficiency. The clustering algorithm, jet reconstruction and b-tagging methods are described in the following.

Topological Clustering Algorithm

Particles hitting the calorimeter will deposit their energy into several cells. However, instead of working with each individual cell that has been hit, cells are grouped into three-dimensional clusters to collect the energy deposited by a single particle. This also reduces noise in the calorimeter, as only cells with certain significant energy above the noise level are accepted as part of the cluster. Cells are clustered using the Topological Cluster Algorithm. This algorithm first finds a seed, i.e. cells with a certain significant amount of energy above the expected energy that depends on electronics and pile-up noise - the first energy threshold. All neighbouring cells in all three dimensions (and cells neighbouring these) that lie above some secondary energy threshold are then added to the seed. Adjacent cells are added until no more lie above this threshold. Outer adjacent cells are then added to the cluster if they pass a tertiary energy threshold. The energy thresholds are defined as

$$\Gamma = \left| \frac{E_{cell}}{\sigma_{noise,cell}} \right| . \tag{13}$$

Here, $\sigma_{noise,cell}$ is calculated from the quadratic sum of the electronics and pile-up noise. ATLAS uses settings of $\Gamma = 4$, 2 and 0 for the primary, secondary and tertiary thresholds respectively.

In addition, an attempt is made to split clusters containing multiple maxima. The final cluster energy is given at an electromagnetic scale, which means its energy measurement is the 'raw' electronic signal from the calorimeter reading.[39] At this scale the energy has not yet been corrected for energy loss in non-interacting neutrinos, invisible nuclear states that absorb energy to form, dead material and from the

cluster reconstruction algorithm itself. It is also not corrected for the response of the calorimeter E/p, where E is the energy of the cluster and p the momentum measurement of the track and which varies with energy and location. Local hadronic calibration (correction applied to each cluster for these energy losses to more closely reflect the true energy of the particle) must subsequently be implemented.

Jet reconstruction

Particle detectors measure quarks as a shower of a bunch of stable hadrons that have been created from quarks and gluons. The charged particles in a shower appear as hits in the calorimeter. In order to tag the original quark in the event, all calorimeter clusters resulting from the hadronisation of the particle must be grouped. This is challenging due to additional low-momentum particles that are irrelevant to the process. These particles can emerge from the underlying event or from pile-up. The input for jets are either clusters generated by the topological clustering algorithm or Monte Carlo generated particles that are stable (by definition, those which have a lifetime of around > 10 ps in the laboratory rest frame) [39]. For the present section, the term 'particle' refers to both types of input. Algorithms are used to group particles and reconstruct what is known as jets. These algorithms aim to leave a jet minimally affected by soft emissions, i.e. particles from pile-up and the underlying event. They must also not fail in the events of collinear splitting - where a parton radiates a gluon moving parallel to the parton.

The algorithm of best performance and thus the one generally used at ATLAS, and in the present analysis, is the anti-k_T method [40]. The algorithm is based on a general description of distance parameters which are

$$d_{ij} = min({p_{Ti}}^{-2}, {p_{Tj}}^{-2})\frac{\Delta R_{ij}^2}{R^2} \tag{14}$$

and

$$d_{iB} = {p_{Ti}}^{2p}, \tag{15}$$

where p_T is the transverse momentum of the particle. The distances are computed for each particle pair and the pair for which d_{ij} is smallest is combined to one particle. If however d_{iB} is smaller than the smallest d_{ij}, particle i is taken off the list of particles, or subjets, and defined as a complete jet. Equation 15 is essentially a cut off on particle combination distances: particles will no longer be combined if the distance between them is greater than R. The negative power in the anti-k_T method means that soft particles will cluster to a hard particle before clustering amongst themselves. The result is thus a circular accumulation of radius R of soft particles around a hard particle if there is no other hard particle within 2R of the first. This is in contrast to other algorithms, where the shapes produced are irregular. Anti-k_T jet shapes are shown in Figure 13. If there are two hard particles with distance $R < \Delta_{ij} < 2R$ then the

circles of accumulated soft particles will be clipped in some way depending on the p_T difference: if the one hard particle has a higher momentum than the other, the first one will accumulate also the soft particles where the two circles centred on the particles overlap (as occurred with the pink and green jets in Figure 13); if they are of similar momenta, the piece of circular area between them is divided by a more-or-less straight line. The jet areas in the event of two hard particles lying within R of each other are again weighted by the relative momenta. The two particles are merged but the jet area is centred towards

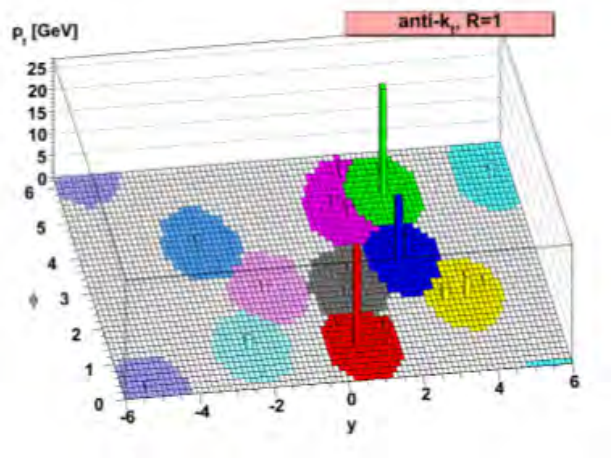

Figure 13: Jets reconstructed using the anti-k_T method in parton-level events. The result is a regular cone shape.[40]

the higher-momentum hard particle. For particles of similar momentum, the area will be malformed by the merging of two circles. The circle-like shape of jets in the anti-k_T method has the advantage that experimental calibration, corrections to background particles and some theoretical calculations are made easier. A disadvantage is that the substructure of a jet is washed out, which leaves little evidence of the branching nature of QCD radiation.[40]

The jet reconstruction efficiencies for the Anti-kT method starts at 100% for 60 GeV and above and decreases down to 95% for jets at 10 GeV. The purity of the jets being reconstructed is 94% at 10 GeV, rising up to 100% for 15 GeV and above.[41] The uncertainties on the reconstruction efficiencies range from $4-1\%$ for 20 GeV $-$ 1 TeV jets, respectively [42].
Acceptance criteria of reconstructed jets generally include limits on p_T and η values to minimise uncertainties. They also include a lower limit on the so-called jet vertex fraction (JVF) in order to avoid including jets from other proton-proton interactions. This requires that a certain fraction of the p_T sum of all tracks associated to the jet comes from tracks that can be associated to the identified primary vertex. Requiring a JVF of > 0.75 has a $\sim 3\%$ effect on the acceptance of events [43].

b-tagging

Due to events of high interest such as the dominant $H \to b\bar{b}$ channel and the dominant top quark decay to a W and bottom quark, the ability to tag a jet containing a b quark is important in ATLAS physics analysis.
A b-flavoured jet can be distinguished from other jets through several traits. Hadrons containing a b quark have short lifetimes relative to light jets. They thus decay within the pixel detector, so that the secondary vertex will be measurably displaced from the primary vertex, and furthermore, lie in line between the primary vertex and the reconstructed jet. The track offset of decay products from the primary vertex is thus one way to separate b-jets from other jets. The relatively high mass of the b quark and its decay to considerably lower mass particles which will necessarily carry away momentum in the transverse direction, leads to a greater number and spread of tracks for b-hadrons compared to other jets. All of these traits mean good b-tagging performance critically relies on the reconstruction performance of charged jets in the ID; specifically the accuracy of measurements in the innermost layer of the pixel detector.
Lastly, b-hadrons can decay semi-leptonically. In this case, one can use the lepton as a flag for the presence of a b-hadron.

The b-tagging efficiency is lower than the jet reconstruction efficiency as it hinges on many additional factors. A jet can only be b-tagged if the primary vertex in the event is known and measured with sufficient accuracy. The possibility of having identified the wrong primary vertex further increases the fake rate of b-tagged jets. Furthermore, only topological clusters associated to tracks can be used.
Whilst light quarks are 10-1000 times lighter than b quarks, c quarks are only 4 times lighter. The c quark therefore has a comparable lifetime, leading to a greater mistag rate of c-hadrons. A b-tagging efficiency of 70% is usually accompanied by a c- and light-mistag efficiency of 20% and 0.7% respectively [43]. These efficiencies are determined by a multivariate technique, MVI, which incorporates various tagging algorithms. The algorithms are respectively based on different types of criteria: impact parameter-, secondary vertex- and decay chain reconstruction-based.[44] As the tagging efficiencies vary with p_T, each jet must be corrected via a p_T-dependant scale factor. For b-tagged jets, this factor varies from 0.91-0.98 with uncertainties of $6 - 20\%$. For c (light) tags, the scale factor is around 1.1 (1.2) with an uncertainty of $12 - 22\%$ (16%) [43].

4.3.3 Missing transverse energy

Measurements of the missing transverse energy, $E_{\mathrm{T}}^{\mathrm{miss}}$, are needed to obtain information on particles that do not interact with the detector. Neutrinos are the only example within the SM. A W boson decays via $W \to \ell\nu$ around 30% of the time and since a top quark will almost always decay to a W boson and a b quark, extracting neutrino information in an event is important for top quark reconstruction. It is also important for the analysis of the Higgs boson decay channels $H \to \tau\tau$ and $H \to W^+W^-$ where the final states include multiple neutrinos. The measurement of $E_{\mathrm{T}}^{\mathrm{miss}}$ is also a way of searching for new particles,

such as dark matter candidates, by inferring the presence of 'invisible' particles.

The missing transverse energy in an event is measured by taking the negative vector sum of the transverse energy based on the calorimeter and muon system deposits. The energy input of this vector sum are from reconstructed objects (electrons, photons, muons, τ's and QCD jets) that have been corrected for energy loss and detector response, as well as from clusters that are not associated to any reconstructed object.
The accuracy of the $E_{\mathrm{T}}^{\mathrm{miss}}$ measurement therefore depends on the efficiencies and uncertainties of the various reconstruction methods as functions of p_T and η. It moreover depends on the accurate modelling of dead material in the detector, electronic noise and instrument failures. These factors all contribute to measurements of fake $E_{\mathrm{T}}^{\mathrm{miss}}$. [39]

4.3.4 Systematic Uncertainties

Various systematic uncertainties associated to specific reconstructed objects have been mentioned in the previous section. These and additional uncertainties are summarised here. The uncertainties are important for the modelling of the expected background on the reconstructed level as the modelled background will eventually be subtracted from the observed event distribution. The accuracy with which the significance of any observed *excess* can be quoted hinges on the systematic uncertainties of the modelled background.
Uncertainties are quoted from ATLAS analyses for $H \to b\bar{b}$ and $t\bar{t}H, H \to b\bar{b}$ channels ([42],[43]).

Dominant uncertainties are in the jet energy scale and the b-tagging efficiencies. Overall, the p_T-dependant JES uncertainty ranges between $1 - 7\%$ [42][43]. The overall uncertainty on flavour tagging efficiency is on the order of $6 - 20\%$, depending on the flavour and p_T of the quark [43].
The uncertainties on lepton reconstruction, identification and trigger efficiencies are only on the order of 1%.
Jet energy scale and lepton measurement uncertainties are then propagated to $E_{\mathrm{T}}^{\mathrm{miss}}$ measurements.

Another dominant effect is the uncertainty in the theoretical cross-section of relevant processes. The uncertainty for the $t\bar{t}$ cross-section, evaluated at next-to-next-to-leading-order (NNLO), is given as on the order of 10% [43].

There is an uncertainty in the integrated luminosity of 1.8% for the 8 TeV run.

Finally, pile-up has an effect on many aspects. In data there will be many more jets to deal with as proton collisions pile on top of each other. This affects the energy measurements of jets as the chances of jets overlapping is increased. It also increases the chances of reconstructing fake jets.

4.4 Physics Analysis at Truth level

In a truth level analysis the objects that are analysed are particles generated by the event generator. Detector level effects are not included and reconstructed objects are not considered. In other words, the factors that are not being considered in Equation 9 are the efficiency, ε, most aspects of detector acceptance and limited energy resolution. This section will define several truth objects that are relevant to the tH analysis in this thesis.
An MC sample of $t\bar{t}$ events is used in order to demonstrate how an analysis at truth level can be performed.

4.4.1 Acceptance criteria

To improve the realism, standard acceptance criteria for MC jets and leptons are applied. These are a $p_T > 25$ GeV and a $|\eta| < 2.5$ requirement. The requirements are motivated by suppression of low-momentum pile-up and underlying event particles and keeping the acceptance area to regions where the detector is of optimum efficiency.

4.4.2 Truth Missing Transverse Energy

The energy carried away by neutrinos is estimated using the truth missing transverse energy, $E_{\mathrm{T}}^{\mathrm{miss}}$. Since there is no pile-up or detector effects, the truth $E_{\mathrm{T}}^{\mathrm{miss}}$ very closely adds up to the true neutrino energy. The resolution of $E_{\mathrm{T}}^{\mathrm{miss}}$ is shown in Figure 14. The width of the distribution is due to the energy loss in truth-level reconstruction of jets discussed below.

4.4.3 Truth Jets

Jets at truth level are reconstructed using the Topological Clustering Algorithm as well as the anti-k_T jet reconstruction algorithm at particle level. Muons and neutrinos are excluded as inputs as they do not deposit significant energy in the calorimeter. In the case of the anti-k_T reconstruction, the distance parameter, ΔR, is set to 0.4.
The jet flavour is determined by the flavour of the highest p_T parton lying within the jet area.

It is not known from which truth quark these jets come from. It is therefore useful to match truth jets to truth quarks to study the relevant jets and compare how successful selection criteria are at selecting the correct jets. The matching is performed by comparing the p_T, η and ϕ values of the jet and quark and so requiring that: the jet and the quark are of the same flavour; $0.4 < p_T^{jet}/p_T^{quark} < 1.2$ and $\Delta R < 0.4$. Approximately 77% of truth b quarks in $t\bar{t}$ events are successfully matched to a b-jet when setting these requirements.

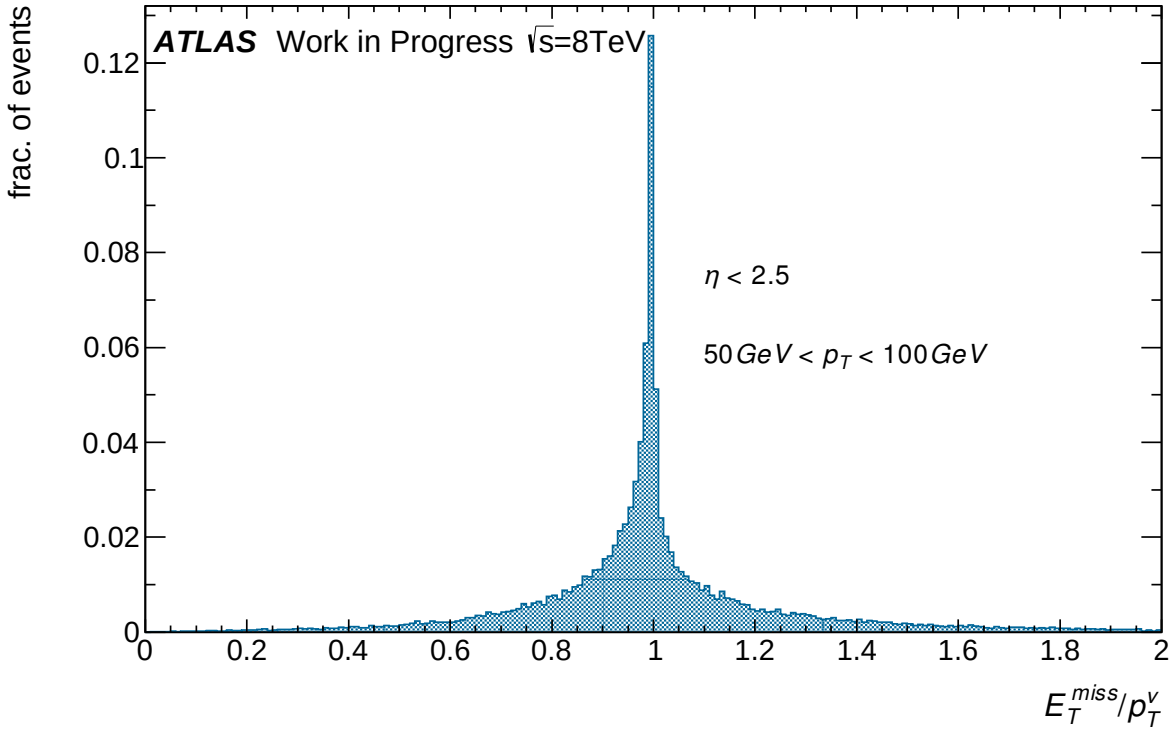

Figure 14: The ratio between the missing energy, $E_{\mathrm{T}}^{\mathrm{miss}}$, and the p_T of the truth neutrino is plotted, for neutrinos within $|\eta| = 2.5$.

The resolution for b-jets matched to b quarks in $t\bar{t}$ events is shown in Figure 15. There is an energy loss in jets, that is much wider than the loss in $E_{\mathrm{T}}^{\mathrm{miss}}$. The resolution is due to partons that were radiated away from the hadronic shower, carrying with it a fraction of the energy, and the p_T threshold on truth particles lying within the jet area. The degradation in resolution is more severe for reconstructed jets, where energy loss may additionally occur through particles falling outside the acceptance or losing energy to dead material whilst passing through the detector.
In reconstruction, $E_{\mathrm{T}}^{\mathrm{miss}}$ is highly dependent on the jet resolution as the loss in jet energy contributes to the sum of missing energy.

4.4.4 Reconstruction of a Parent Particle

A good way of discriminating between signal and backgrounds is to reconstruct the invariant mass of a parent particle from its decay products. The two muon tracks in the event displayed in Figure 10, for example, would be used in this way: if their invariant mass is close to the Z boson mass, the event is tagged as a Z boson production event.

The invariant mass of a particle is calculated using the energy and momentum of its decay products, as

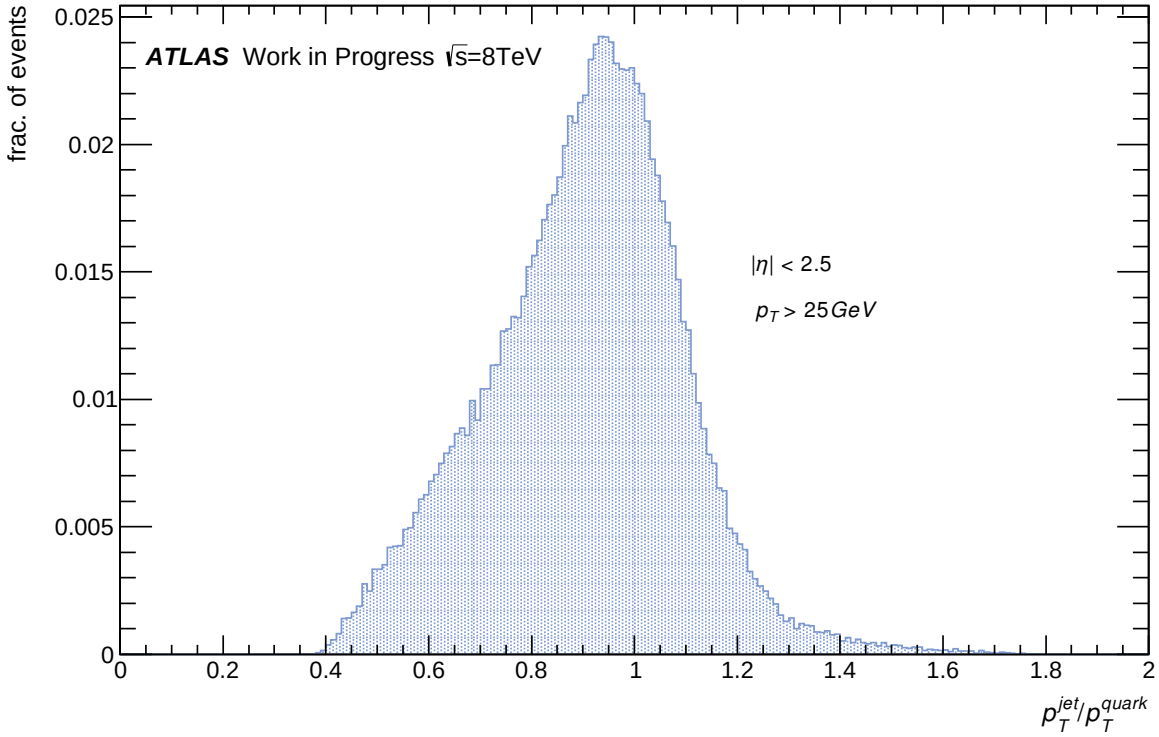

Figure 15: The p_T ratio between the truth b jet and the truth b quark is plotted, for quarks with $|\eta| = 2.5$ and 50 GeV $< p_T <$ 100 GeV.

$$m^2 = \sum E_i^2 - |\sum \mathbf{p}_i|^2, \tag{16}$$

where i is the index of the decay particle and $c = 1$.

The top quark decays to a W boson and b-jet. Therefore the first step is to reconstruct the W boson from the lepton and $E_{\mathrm{T}}^{\mathrm{miss}}$. Whilst the $E_{\mathrm{T}}^{\mathrm{miss}}$ information provides the transverse energy for the neutrino, the z component must be calculated by using Equation 16 and imposing a W mass constraint. For a neutrino, $E^2 = |\mathbf{p}|^2$, and so

$$\begin{aligned}
M_W^2 &= (E_\ell + E_\nu)^2 - [(p_x^\ell + p_x^\nu)^2 + (p_y^\ell + p_y^\nu)^2 + (p_z^\ell + p_z^\nu)^2] \\
&= E_\ell^2 - (p_x^{\ell 2} + p_y^{\ell 2} + p_z^{\ell 2}) + E_\nu^2 + 2E_\ell E_\nu - (p_x^{\nu 2} + p_y^{\nu 2} + p_z^{\nu 2}) - 2(p_x^\ell p_x^\nu + p_y^\ell p_y^\nu + p_z^\ell p_z^\nu) \\
&= m_\ell^2 + 2E_\ell E_\nu - 2(p_x^\ell p_x^\nu + p_y^\ell p_y^\nu + p_z^\ell p_z^\nu) \\
&= m_\ell^2 + 2E_\ell \sqrt{p_x^{\nu 2} + p_y^{\nu 2} + p_z^{\nu 2}} - 2(p_x^\ell p_x^\nu + p_y^\ell p_y^\nu + p_z^\ell p_z^\nu).
\end{aligned}$$

Here, p_x^ν and p_y^ν are substituted with $E_{\mathrm{T}}^{\mathrm{miss}}\cos\phi$ and $E_{\mathrm{T}}^{\mathrm{miss}}\sin\phi$, respectively. The equation is then solved for p_z^ν using the quadratic equation to eventually obtain two solutions,

$$p_z^\nu = \frac{1}{2(E_{\ell^2} - p_z^{\ell^2})}\langle p_z^\ell[2(p_x^\ell E_{\mathrm{T}}^{\mathrm{miss}} cos\phi + p_y^\ell E_{\mathrm{T}}^{\mathrm{miss}} sin\phi) - m_\ell^2 + M_W^2]$$
$$\pm \sqrt{E_\ell^2[(2p_x^\ell E_{\mathrm{T}}^{\mathrm{miss}} cos\phi + 2p_y^\ell E_{\mathrm{T}}^{\mathrm{miss}} sin\phi - m_\ell^2 + M_W^2)^2 - 4E_{\mathrm{T}}^{\mathrm{miss}2}(E_{\mathrm{T}}^{\mathrm{miss}2}{}_\ell - p_z^{\ell^2})]}\rangle. \quad (17)$$

The minimum value for p_z^ν is chosen. If the value within the square root is negative, $E_{\mathrm{T}}^{\mathrm{miss}}$ is recalculated so that the discriminant is zero, i.e.

$$(2p_x^\ell E_{\mathrm{T}}^{\mathrm{miss}} cos\phi + 2p_y^\ell E_{\mathrm{T}}^{\mathrm{miss}} sin\phi - m_\ell^2 + M_W^2)^2 - 4E_{\mathrm{T}}^{\mathrm{miss}2}(E_\ell^2 - p_z^{\ell^2}) = 0$$

and solving for $E_{\mathrm{T}}^{\mathrm{miss}}$,

$$E_{\mathrm{T}}^{\mathrm{miss}} = \frac{m_\ell^2 - M_W^2}{2(p_x^\ell cos\phi + p_y^\ell sin\phi \pm \sqrt{E_{ell}^2 - p_z^{\ell 2}}}. \quad (18)$$

The value that results in a valid value for eq. 17 is then chosen.

The invariant mass of the W boson reconstructed in this way is shown in Figure 16. The invariant mass

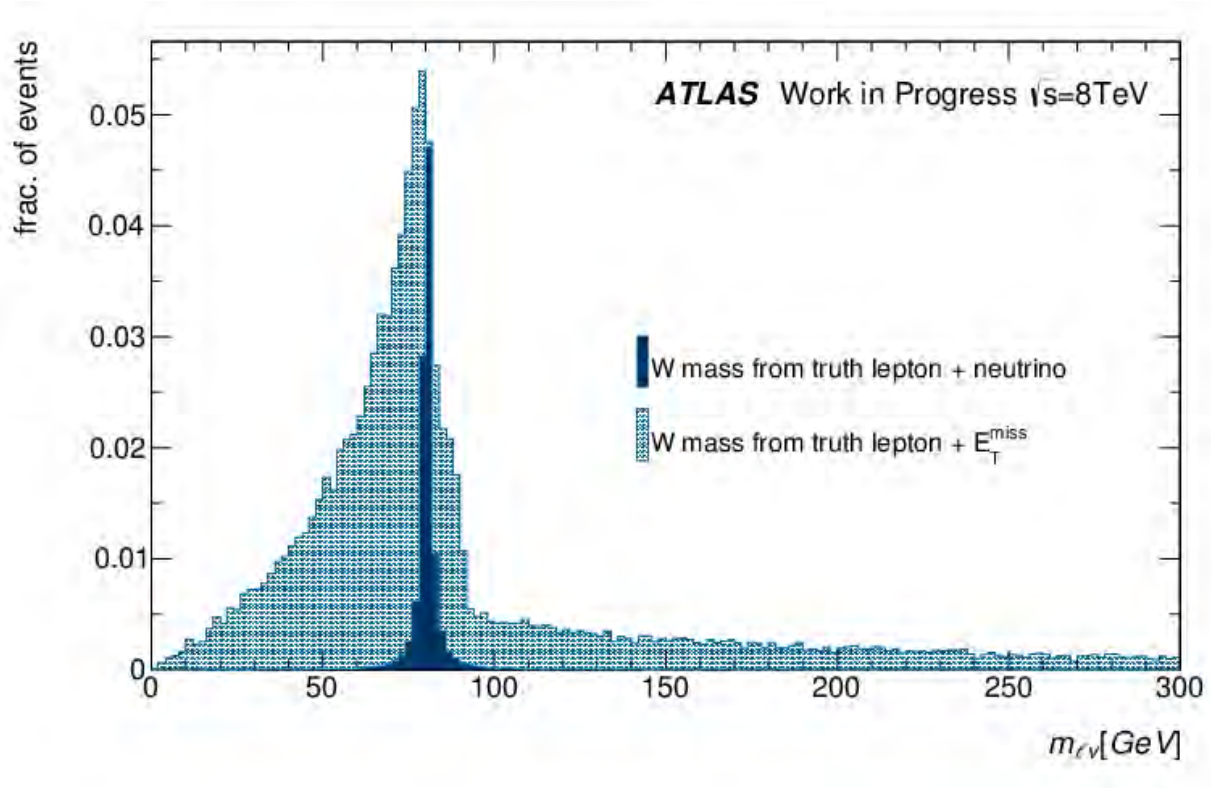

Figure 16: The invariant mass of the W boson is plotted. The W boson four-momentum was computed using the lepton and $E_{\mathrm{T}}^{\mathrm{miss}}$ information and by imposing a W boson mass constraint via eq. 17. The invariant mass of the truth lepton and truth neutrino is shown for comparison.

of the top quark can subsequently be computed from the W boson and b-jet four-momenta. The result is

displayed in Figure 17 where the invariant mass is that of the W boson and the b-jet, which was matched to the relevant b quark.

Due to the jet and $E_{\mathrm{T}}^{\mathrm{miss}}$ resolutions the distribution is widened around the true top quark mass of

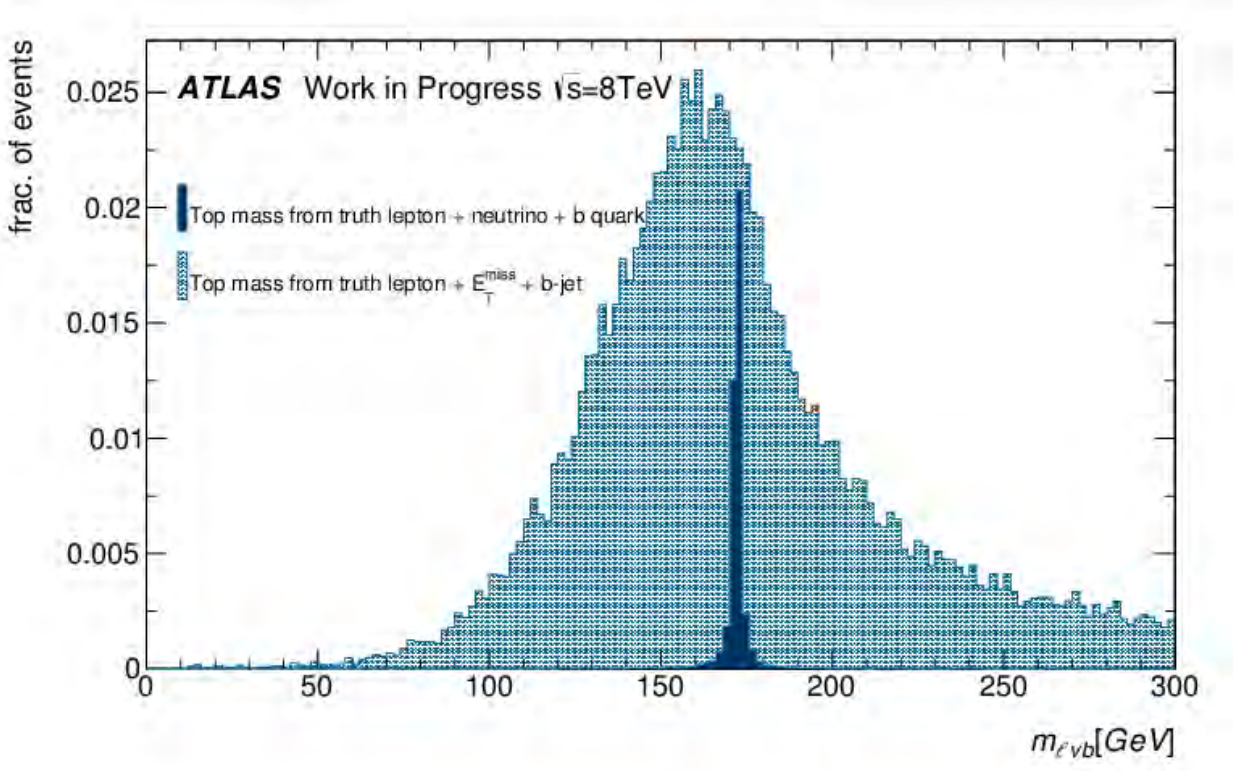

Figure 17: The invariant mass of the top quark is plotted. The W boson four-momentum was computed using the lepton and $E_{\mathrm{T}}^{\mathrm{miss}}$ information. The invariant mass for the top quark was then obtained from the W boson together with the b-jet matched up to the relevant b quark. The invariant mass of the truth lepton, truth neutrino and truth b quark is shown for comparison.

173 GeV.

4.5 Signal and Background Modelling Uncertainties

Whilst for truth level analysis, reconstruction efficiencies, although noted, do not have an effect here, uncertainties do arise from the Monte Carlo generation of the signal and background processes. These uncertainties are related to the fitting of the parton distribution function (PDF), renormalisation and factorisation scales and the modelling of parton showering and hadronisation. All of these affect cross-section calculations and hence the normalization of event counts. They are expected to be the dominant uncertainties.

The renormalisation and factorisation scales are imposed in order to cut off divergences in QFT so that a full calculation of the hard scatter cross-section becomes possible.

One divergence emerges in the QCD coupling behaviour: the coupling decreases at high energy scales (short distances) but tends to infinity at low energy scales (large distances). This can be attributed to the anti-screening effect from virtual gluon loops. The divergence is regulated by the renormalisation factor, μ_R.
The partonic cross-section is computed by expanding α_s around zero, i.e. at high Q. Additional terms to the leading order arise from the virtual quark and gluon loops – where the renormalisation scale is imposed – as well as from real gluon emissions. Here, a second divergence arises for soft gluons or gluons that are emitted collinearly to the moving parton. The factorisation scale, μ_F, regulates this. It effectively determines to which level partons and accompanying emissions are resolved. It thereby sets the boundary between processes that can be perturbatively calculated, and processes that have to be modelled.

The Parton Distribution Function (PDF) describes the distribution of quarks and gluons within the colliding proton – it gives the probability of finding a parton of a certain flavour carrying a certain fraction of the protons momentum. These functions can only be determined from fits to real data, as QCD does not offer description of PDFs [45].
An interaction matrix element is used, to evolve a collision of protons described by a given PDF. This matrix relates initial state particles (the gluons and quarks within the proton) to final state particle, determining the type and number of particles that are produced during the collision based on the energy of the incoming protons, PDFs and the probability of outcomes.

The matrix element is used to compute hard scatter processes (large p_T and large angles processes) at LO or NLO, determined by the order of expansion in α_s. Parton shower methods are then used to model low-p_T and collinear radiation, i.e. the contributions at higher order. This is done for both the incoming partons and outgoing partons, giving initial state radiation (ISR) and final state radiation (FSR). Once parton showers are generated, the final state patrons are subject to the hadronisation process in which the splitting and recombination of partons is modelled until all final state particles are stable and colourless.

When producing any Monte Carlo sample, several choices need to be made. These include choosing the renormalisation and factorisation scales, the PDF fit and models for parton showering and hadronisation. Any free parameters of the Standard Model, such as the masses of particles, must also be chosen. In order to determine the uncertainty in the input, several MC samples are generated with varied values or different models. The amount of deviation is taken as the uncertainty of the relevant input.

In the following, uncertainty estimates are obtained by looking at ATLAS analyses of cross-section measurements for top quark processes ([46], [47]). The quoted uncertainties are uncertainties of the cross-section measurements of the processes.
Uncertainties in the case of the modelling of the $t\bar{t}$ process, which is well understood, is dominated by

the choice of the PDF and the ISR/FSR modelling. These are on the order of $2-3\%$ [46]. The mass of the top quark is known to a precision of 0.9 GeV and varying this leads to subpercent uncertainty. Effects of scaling is also on the order of 1% [46].
The uncertainty in modelling of the single top quark is higher. The uncertainty in PDF is on the order of $3-8\%$ whilst the computation of ISR/FSR is on the order of 9%.[47]

5 Studies on particle flow

The studies on particle flow that were carried out for this work involved investigating the behaviour of clustering in the electromagnetic calorimeter of particular Monte Carlo events, with the aim of understanding certain processes underlying the implementation of particle flow. First a description of the particle flow algorithm is given, followed by the details of the studies done for the current work.

The construction and development of *particle flow* algorithms in ATLAS events is motivated by the relative resolutions of the tracker and the calorimeter. The charged pion resolution as a function of p_T at $\eta = 0$ is shown in Figure 18 for both subdetectors. At $\sim$ 150 GeV and below the p_T measurements in the tracker have a better resolution than the energies measured in the calorimeter. The degradation of the tracker resolution with rising p_T is due to the charged particle track's degree of curvature in a magnetic field being inversely proportional to its p_T. With rising p_T then an increasingly smaller sagitta is measured. In calorimeters on the other hand the resolution is related to the statistical fluctuations of the initiated particle shower. As the number of particles within a shower increases with the energy of the incoming particle, higher energy particles will initiate showers with lower statistical fluctuations and hence produce a signal of finer resolution. Associating clusters to tracks will therefore yield more

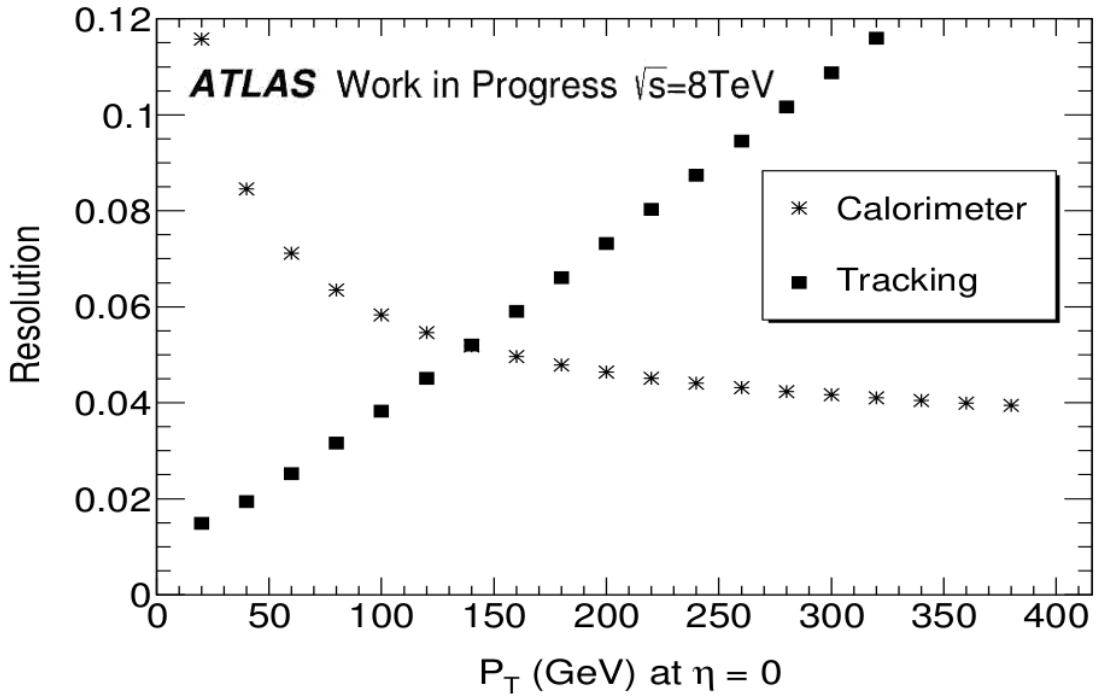

Figure 18: The charged pion resolution at $\eta = 0$ as function of p_T are shown (Figure 1 in [33]). The squares (stars) represent the resolution in the Inner Detector (calorimeter).

accurate measurements of momenta as well as direction by replacing the calorimeter measurements with those from the tracker for particles below $\sim$ 150 GeV.

In particle flow algorithms particles are reconstructed and identified by drawing upon and associating all information recorded by the various detector components. The process requires development and fine-tuning of algorithms used in each subdetector in order to obtain maximum efficiency and low fake rates. Particle flow has been widely used in the CMS experiment [8]. For CMS, the main benefit is improving the jet resolution. Hadron calorimetry in the ATLAS detector however already yields excellent resolution. Therefore, for ATLAS the main benefit is from the reduction of the impact of pile-up: because one can obtain better directional information from tracks, it is easier to extrapolate tracks associated to clusters to the correct primary vertices than extrapolate the clusters themselves.

The focus of these studies is the step in the particle flow algorithm in which information from charged tracks is associated with information obtained from the calorimeter [48]. The algorithm outputs so-called *eflow* objects which can be either charged or neutral. These objects thereafter become jet inputs. A charged eflow object is either a cluster that has been successfully associated to a track, or it is an isolated track (no clusters found in its vicinity). A neutral eflow object is reconstructed from an isolated cluster, which has also been ruled out as noise in the calorimeter. Additionally, neutral eflow objects are created from the remaining cells inside clusters remaining after cells associated with charged particles have been removed. When a charged eflow object is reconstructed, its energy is that measured in the tracking system.

The eflow object reconstruction process is illustrated in Figure 19. The value $E_{expected}$ is the expected energy of the cluster, and $\sigma_{expected}$ is the width of the expectation. These values are derived from the E/p response curve of the detector, where E is the energy measurement in the calorimeter and p is the momentum measurement in the tracker. Response curves are computed using single pion events and plotting the distribution of the number of events against values of E/p. These vary with the pions' extrapolated coordinates, track momenta and the calorimeter layer within which the deposits lie. The value for $E_{expected}$ and its width, $\sigma_{expected}$, are then obtained from $p_{track} \times \langle E/p \rangle$ where $\langle E/p \rangle$ and its width are extracted from a Gaussian fit to the local E/p curve. The algorithm further contains two variables, k_1 and k_2, that can be set so as to adjust energy thresholds and optimise eflow reconstruction. It is noted that the value for k_1 can be independently set in the two times that it appears.

The particle flow algorithm begins with the extrapolation of the track to the second layer of the three-layered EM calorimeter (refer to Figure 12) to obtain the tracker coordinates within the calorimeter. The nearest cluster to the track is then identified (step 1 in Figure 19). If this cluster has an energy above the energy threshold $E_{cluster} > E_{expected} - k_2 \times \sigma_{expected}$, cells of the cluster are subtracted one by one until the expected energy is recovered (step 2a in Figure 19). The nominal value for k_2 is -1.
A charged eflow object is then reconstructed and the remaining cells in clusters are kept. The procedure is repeated for any other tracks associated to the cluster. If the energies of the remaining clusters are

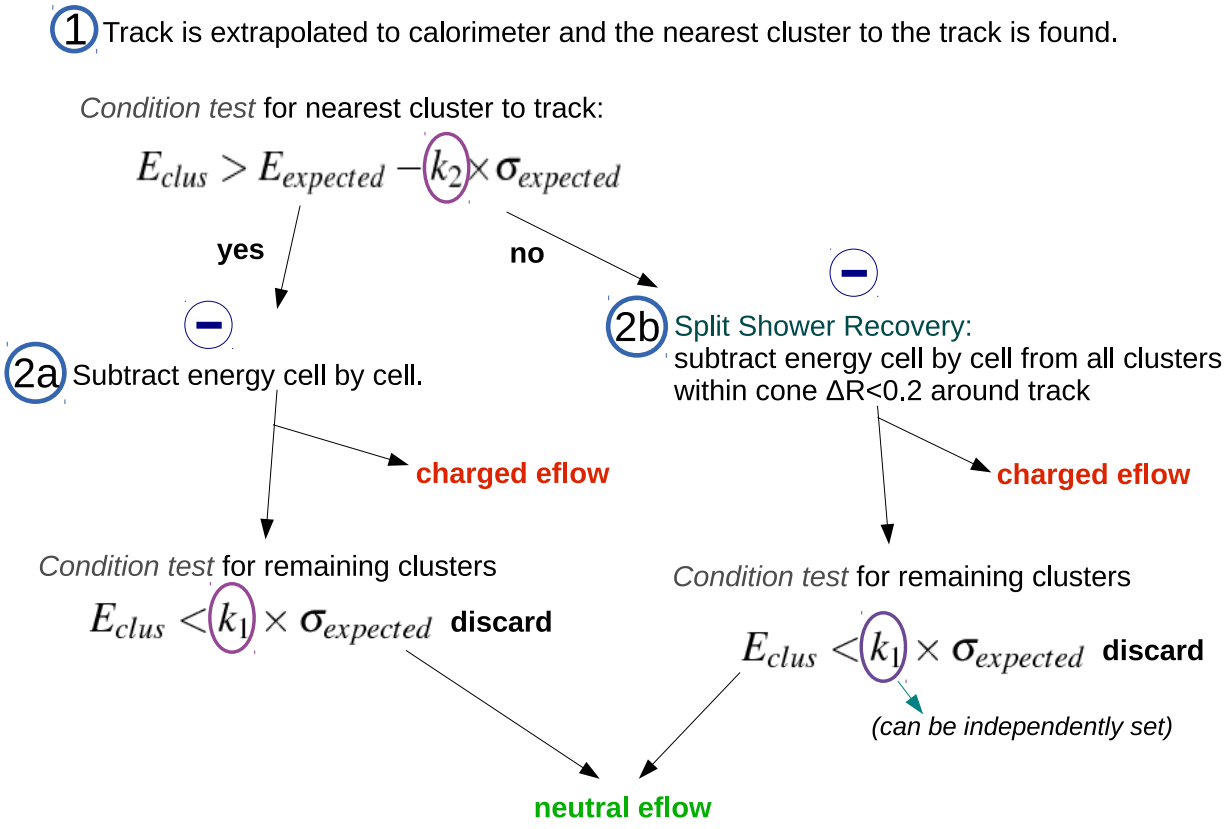

Figure 19: Procedure for identifying charged and neutral eflow objects. The variables, k_1 and k_2, can be set before the algorithm is run and k_1 can be different in the two cases that it is used.

found to have an energy that is below the threshold $E_{cluster} < k_1 \times \sigma_{expected}$, the clusters are discarded as fluctuations, else they are made into neutral eflow objects. The nominal value for k_1 in this case is 2. If the cluster nearest to the track does not pass the energy threshold, the *Split Shower Recovery Algorithm* is run (step 2b in Figure 19). This algorithm attempts to recover particles that were split into several clusters. In this case, all clusters within a cone of $\delta R(\sqrt{d\eta^2 + d\phi^2}) < 0.2$ of the extrapolated track coordinates are selected and energy is subtracted from these clusters cell by cell. A charged eflow object is then reconstructed. The new clusters are tested in step 2b the same way as in step 2a, but the value for k_1 may differ. The nominal value here is 1.28. After a neutral eflow object is reconstructed it can optionally be calibrated to the hadronic scale, i.e. all energy corrections are made so that its energy now more closely represents the true energy of the particle.[33]

The *order* of subtractions of the cells is computed via an algorithm based on the shape of the energy density profile. The energy density profile will peak in one of the layers, known as the 'layer of first

interaction'. This is the electromagnetic core of the shower, and is followed by a slowly decaying tail formed by subsequent interaction and decay products along the track axis. The core will hold an average 50% of the total energy and most of the visible energy.[33] The subtraction starts with the cluster associated to the highest p_T track and is ordered from the 'layer of first interaction' to subsequent layers, from the nearest to furthest ring of cells around the extrapolated track within each layer, and from the highest to lowest energy density cell within each ring. The ordering begins with the cells, moves out into rings of the same layers, and then further out to neighbouring layers.

The behaviour of clustering for different particle types, p_T ranges and η regions was investigated using *calibration hits*. Calibration hits are objects that are produced in specialised Monte Carlo simulations that provide full information on which particles deposited energy in active *and* inactive calorimeter cells, as well as dead material (which is given a simple granularity of 0.1×0.1). This provides the true energy deposited in actual calorimeter cells, and the invisible and missing energy, of any given particle passing through the detector. It allows detailed studies that include particles that have disappeared into dead material completely or particles of different types that have, by the bending of the magnetic field, together formed one cluster. Calibration hits are also a useful way to separate the energy from truth particles (truth energy) and energy from noise in the calorimeter.

5.1 Single particle studies

The inputs to the eflow algorithm are reconstructed tracks in the ID and clusters in the calorimeter. In order to eventually improve eflow reconstruction, the behaviour of the input objects needs to be understood. The focus in the present analysis is on cluster behaviours. To study the baseline performance of the topological clustering algorithm (refer to Section 4.3.2 for a description of the algorithm), MC events containing a single particle were created in order to create a 'clean' environment for analysis, as only one true cluster is expected in each event.
The effects of noise threshold settings on cluster properties and cluster splitting were first investigated. The noise suppression threshold determines the level in a cell below which any fluctuations are cut out. As the noise threshold is crucial for controlling rising noise levels with higher pile-up, the value is tuned depending on the amount of pile-up in events.
Further studies were done on the efficiency of the eflow reconstruction algorithm implemented on clusters in single partice events.

5.1.1 Samples and selections

Samples were specially created to include calibrated clusters, calibration hits, cell information, MC truth information and eflow objects. Files were generated for π^0, π^+ and π^- particles, as these are most commonly produced in particle showers. The production probability of each is roughly a third. Charged pions predominantly decay to muons. However, as charged pions travel a mean distance of $\sim$ 8m, they interact with the calorimeter directly. Neutral pions predominantly decay to two photons. Their travel distance before decaying is typically $\sim$ 25nm and so, in contrast to charged pions, it is the decay products that commonly interact with the calorimeter [16].

These files were produced with a flat distribution for logarithmic energy values, E, for energies ranging from 200 MeV to 2 TeV (i.e particles of varying energies were produced). Files were produced at noise suppression thresholds of 0, 8 and 30 (refer to Section 4.3.2 for a definition of the noise threshold).

Additionally, a sample was generated for π^+ particles with a suppression threshold of 30 and at a fixed energy of 1 GeV, the p_T distribution thus ranging from 0 to 1 GeV. This fixed energy sample helped to disentangle the effects that vary with particle energy.

5.1.2 Noise threshold effects

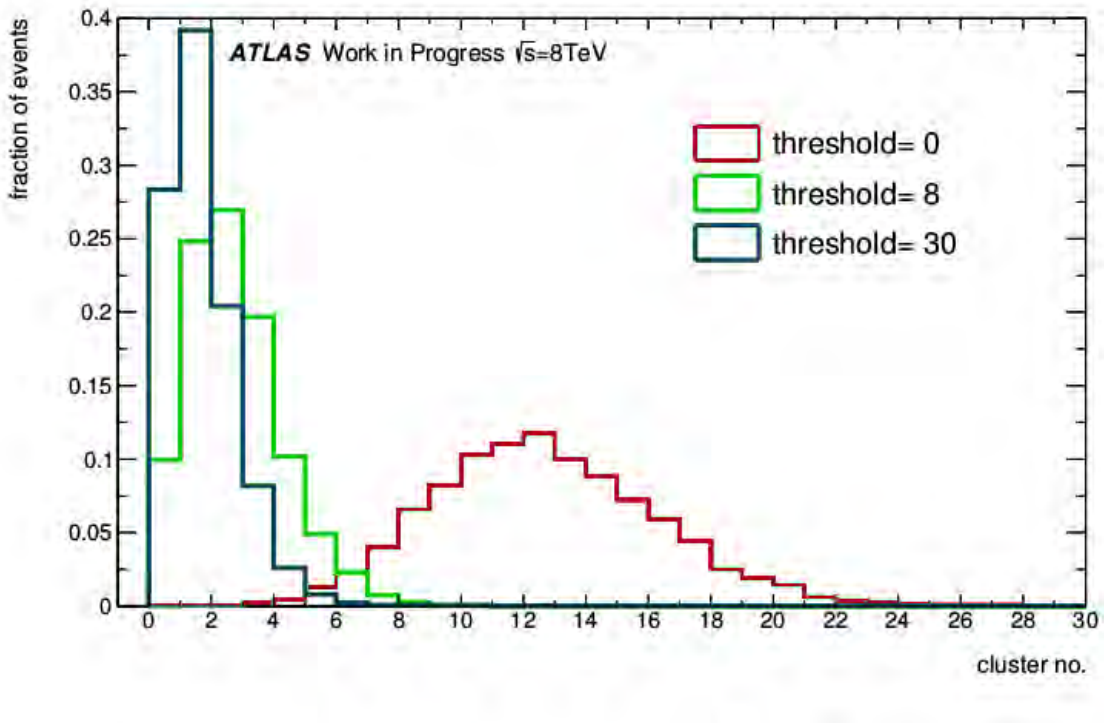

Figure 20: The number of clusters per π^0 single particle event is plotted where pion energies range from 200 MeV to 2 TeV. Clusters with truth energy *as well as noise* have been included. Distributions for three different noise threshold values are shown; in blue (threshold=30), green (threshold=8) and red (threshold=0).

In these single particle events, a single reconstructed cluster for charged pion events is expected, whilst up to two clusters are expected for neutral pion events as the neutral pion is expected to have decayed to two photons. The opening angle between the photons, however depends on the energy of the pion: the higher the pion energy, the closer the photons are produced. Nearby photons may appear as one reconstructed cluster.

This picture is spoilt by the impact of noise in the detector and effects from the imperfect cluster reconstruction. The behaviour of clusters from noise is shown in Figure 20 for the π^0 particle, where pion energies range from 200 MeV to 2 TeV. If there is no noise suppression (threshold=0), the number of clusters peaks at around 12 per event. This improves significantly for a suppression threshold set to 30 - it is then that the number of clusters peaks at one, however, 28% of events now contain zero clusters. A high suppression thus comes at a cost of loss in efficiency. Comparing Figure 20 to 21a, the amount of 'noisy' clusters becomes evident. Here the same histograms are shown for all three types of pions at

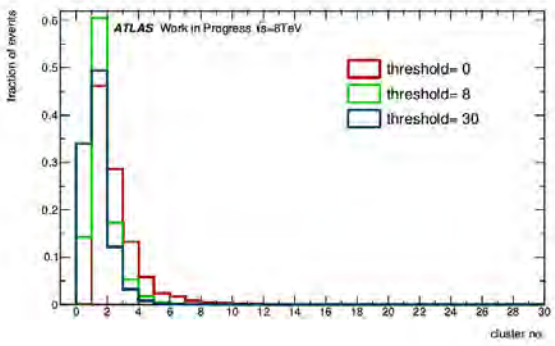

(a) π^0

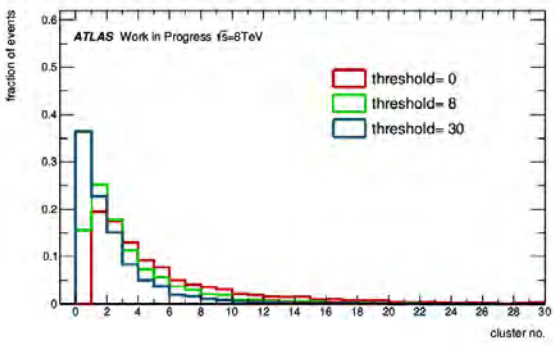

(b) π^+

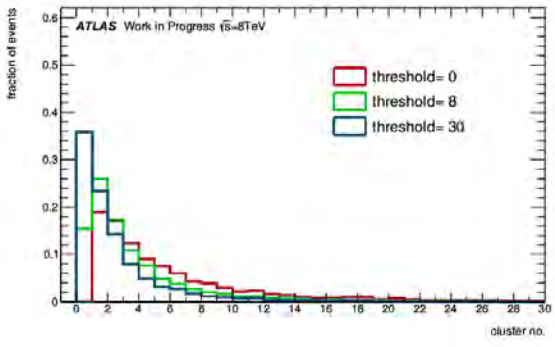

(c) π^-

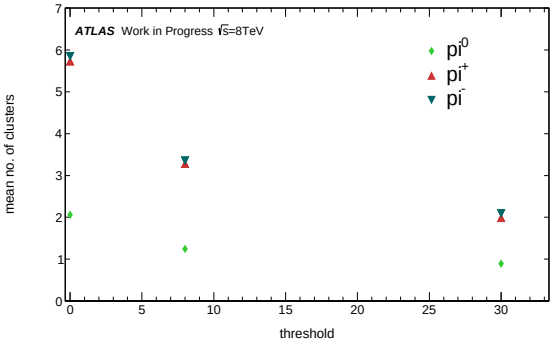

(d) mean number of clusters for all samples.

Figure 21: Plots (a)-(c) show the number of clusters per particle per event for π^0, π^+ and π^-. The three distributions in each plot represent three different noise thresholds.
In (d), the mean number of clusters for each particle type and threshold value is shown.

different threshold values, *but* with noisy cells excluded. In the π^0 case for a threshold of 30, Figure 21a, around 35% of events have no clusters, $\sim$ 50% have one cluster and the histogram peaks here. Events in the charged pion cases (figures 21b and 21c) for threshold 30 appear slightly less ideal: 40% of events have no clusters at threshold 30, and the histograms peak here. The charged pions however exhibit longer tails. The effects of the tails is evident in Figure 21d. Here the mean number of clusters for each sample and threshold value is plotted. Whilst the cluster number for charged pions *peaks* at zero, their mean value is actually closer to two. The mean value for the neutral pion is at one. Across all threshold values, charged pion events will on average produce more clusters than neutral pions. The reason for the higher number of clusters can be due to its size: hadronic showers are generally larger and therefore more likely to split into multiple clusters. It may also be due to the bremsstrahlung that charged pions undergo when travelling through the magnetic field of the ID. The radiated particles via bremsstrahlung result in additional energy deposits in the calorimeter.
Overall, the importance of setting the right threshold value to suppress noise is noted here, as otherwise one has on average more clusters than there are particles. In reality the threshold value is additionally important for pile-up suppression and so its value will strongly depend on the amount of pile-up in an event.

5.1.3 Two Cluster Events

The high average number of clusters for $\pi^{+/-}$ events prompted an investigation into single particle events at threshold value 30 with two clusters only. The relative properties of the two clusters were studied to understand why particles are split. The relative total amount of energy in each cluster was first studied and is presented in Figure 22. Figures 22a and 22b are from the flat logE distribution samples for π^0 and π^+, whilst the plot in Figure 22c is from the fixed energy sample. Events for π^- exhibit similar behaviour to those for π^+. The x-axis shows the fraction of the energy of the lower energy cluster over the energy of the higher energy cluster. It appears that for a significant fraction of two cluster events, the energy in the second cluster is small enough to have negligible impact. Around 32% of events in the π^0 sample and 38% of events in the π^+ sample have an energy fraction of less than 5%. In the bottom plot of Figure 22, the energy fraction for the fixed 1 GeV energy sample is shown. Here, working with a fixed energy sample proves to be illuminating. The fraction is more widely distributed and so most of the second clusters *do* hold a significant fraction of the particle's energy. Evidently, the conveniently small ratio depends on the particle energy: For a low 1 GeV energy particle, a split cluster is a non-negligible occurrence.

To construct a three-dimensional picture of the cluster splitting, the direction of the splitting was studied for two cluster events. Only events where the energy ratio of the two clusters is greater than 5% were selected. The splitting behaviours are summarised in figures 23, 24 and 25 for π^0, π^+ and fixed energy π^+, respectively. The figures show the distances of the two clusters in three different directions: η, ϕ and λ, the last of which is the depth into the calorimeter. In all cases the splittings in the η and ϕ directions

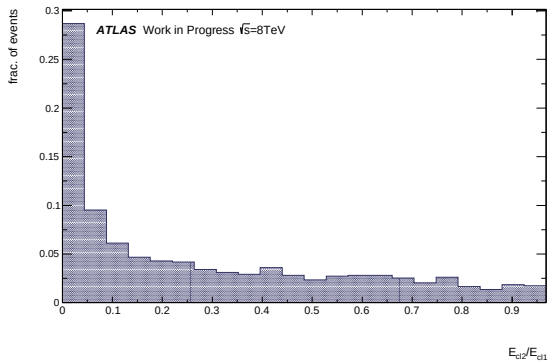

(a) π^0 two cluster events

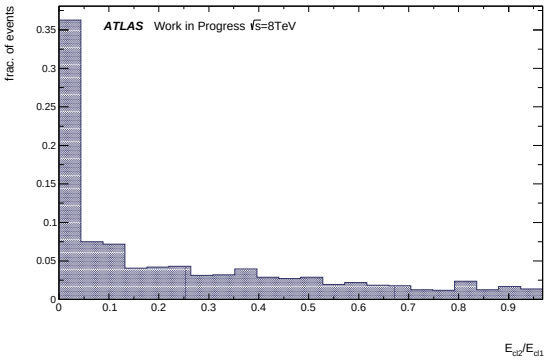

(b) π^+ two cluster events

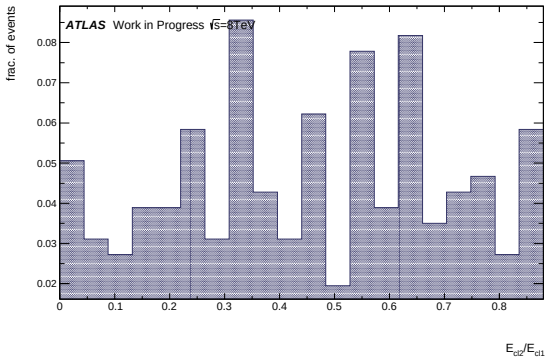

(c) π^+ *at fixed energy* two cluster events

Figure 22: The energy fraction between two clusters in two cluster events are displayed. Plots (a) and (b) display histograms of the energy fraction of the π^0 and π^+ samples with a flat logE distribution. Plot (c) is the same histogram for the π^+ at fixed energy. The x-axis is the fraction of the lower energy cluster over the higher energy cluster. An even split would thus appear at one.

are small. The splittings in the $\delta\eta$ direction in charged pion events are twice as big as those for π^0, whilst in the $\delta\phi$ direction it is comparable. The splittings in the λ direction differ: the clusters in the charged pion events appear to be separated to a much greater depth than in the neutral pion case. The average of the π^0 λ distances is 107 mm. This is less than the total liquid argon calorimeter depth, which is $\sim$ 470 mm and denoted by the solid red line in the plots. The average distance for π^+ (π^-) is 627 mm (671 mm), which is larger than the LAr depth. It is apparent that the splitting occurs along the shower axis, and that for charged pions the one cluster often lies in the EM calorimeter and the other further out in the hadronic calorimeter. The splitting along the shower axis can again be attributed to bremsstrahlung, where radiated particles reacted within the EM calorimeter and the charged pion initiated a hadronic shower deeper in the hadronic calorimeter.

The results for the π^+ fixed energy sample show that two clusters in low energy charged pion events, although more or less split as much in the η and ϕ directions, tend to be not as widely separated along the shower axis as in the charged pion events of flat logE. The average λ value of 245mm, though still greater than for π^0, is well within the LAr depth. It can thus be concluded that higher energy particles

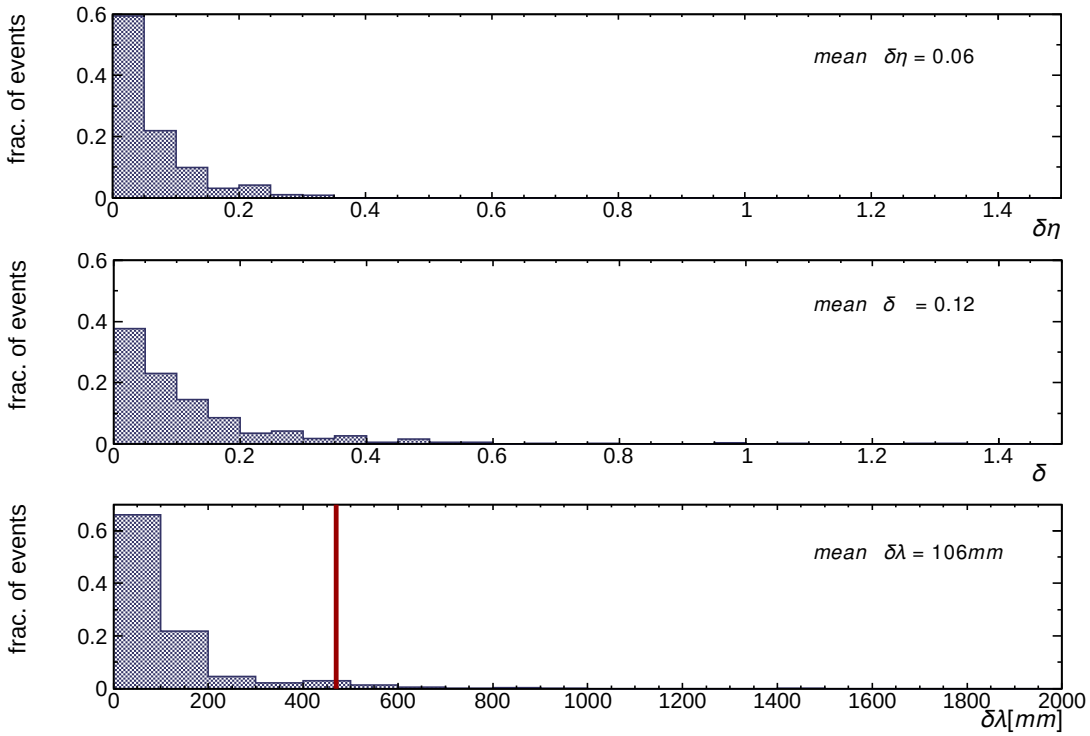

Figure 23: Direction of splittings of clusters in two cluster events for π^0: Plotted are the distances between the two clusters in the η, ϕ and λ directions.

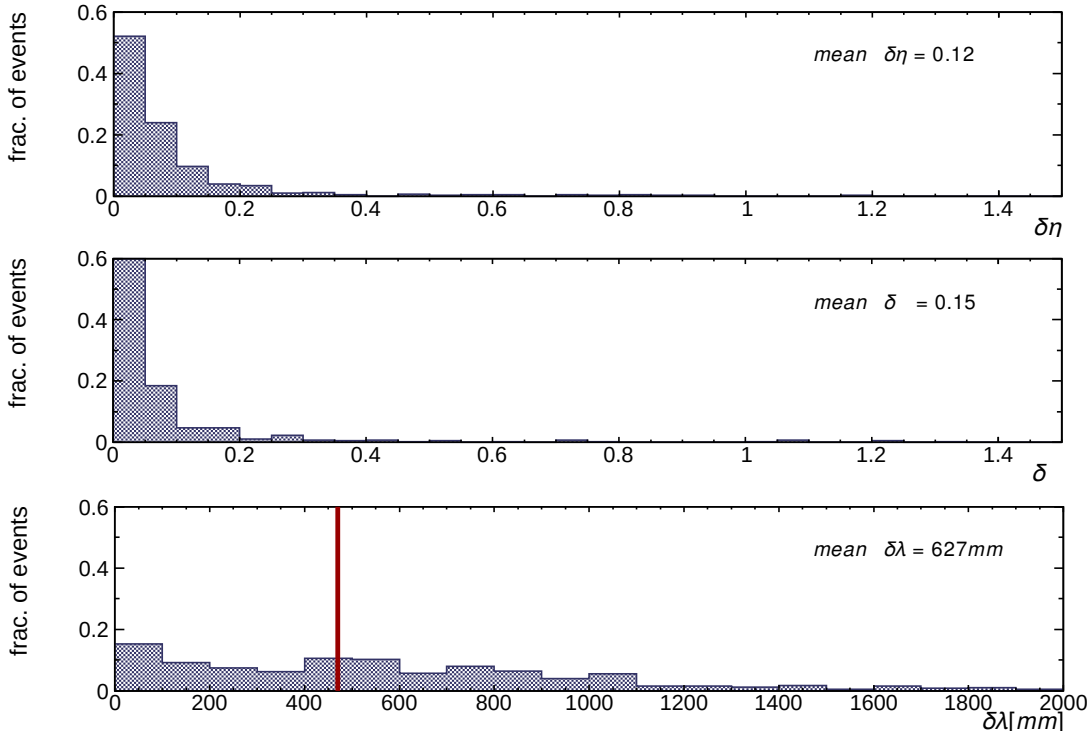

Figure 24: Direction of splittings of clusters in two cluster events for π^+: Plotted are the distances between the two clusters in the η, ϕ and λ directions. The splittings in π^- events are similar.

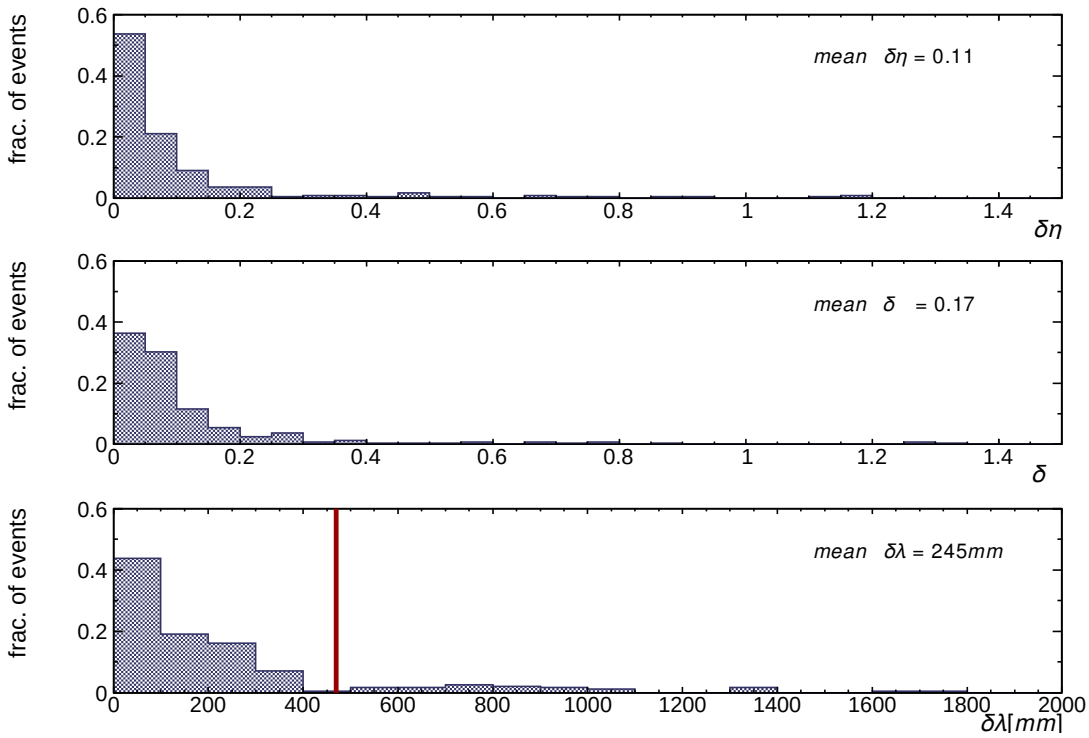

Figure 25: Direction of splittings of clusters in two cluster events for π^+ at **fixed** energy: Plotted are the distances between the two clusters in the η, ϕ and λ directions.

produce split clusters that are wider apart as these produce showers which are more extended in depth. The splittings in the $\eta - \phi$ plane for charged pions should be small enough for the Split Shower Recovery Algorithm to successfully reconstruct a charged eflow object from both clusters (the Split Shower Recovery cone has a width of $\delta R = 0.2$).

5.1.4 Reconstruction of Eflow Objects

Finally, the efficiency of the reconstruction of eflow objects was briefly explored. In the case of a single particle event where the particle is a charged pion, one charged eflow object and no neutral eflow object is expected. In Table 1 the success rate of this is estimated, simply by counting the number of neutral and charged eflow objects per event for the π^+ sample at fixed energy. Object counting was confined to the inner $|\eta| < 0.8$ region, and neutral objects are only counted if they lie within $\delta\eta = 0.2$ of a charged eflow object. Due to a p_T requirement of 500 MeV and above of tracks in the generation of samples, only events with pions of $p_T > 500$ MeV are included. Thus, this selection contain pions with p_T values ranging from $0.5 - 1$ GeV.

		0 objects	1 object	2 objects	3 objects	4 objects
$thr = 0$	charged	16%	84%	0%	0%	0%
	neutral	35%	37%	18%	7%	3%
$thr = 30$	charged	13%	87%	0%	0%	0%
	neutral	81%	16%	3%	0%	0%

Table 1: fraction of charged and neutral eflow counts per event and at $|\eta| < 0.8$ for different threshold values, for the 1 GeV fixed energy sample. Neutral eflow objects were only counted if they lay within $\delta\eta = 0.2$ of a charged eflow object.

Either one or no charged eflow object is reconstructed in an event. At a threshold value of 30, the fraction of 1 charged eflow object events is 87%. This is consistent with the tracking efficiency, which lies at around $80 - 85\%$ for p_T values of $0.5 - 1$ GeV [49]. The fraction of one charged eflow object events for a noise threshold value of 0 is similar.
It is evident that a 0 noise threshold value will lead to more neutral eflow object being reconstructed. This likely results from the increased amount of clusters of noise when the threshold value is low or zero. For a threshold value of 30 the situation is much improved, however 19% of events still include surviving neutral eflow objects within $\delta\eta = 0.2$ of a charged eflow object when these should have been discarded as noise fluctuations.

The surviving neutral eflow objects are further investigated by looking at the event lay-out. Two-dimensional visualisations of calorimeter hits and eflow objects in charged fixed energy pion events are presented in figures 26 and 27, in two parts: in (a) the visualisation is before the particle flow algorithm implementation, and (b) is the visualisation for after. Here the calorimeter is represented in its various layers in the central region: the presampler, the EM sampling layers 1-3, and the hadronic barrel sampling layers 1-3 (refer to 4.1.2 for a description of the calorimeter layout). The first pane in each subfigure shows the location of the extrapolated track coordinate, i.e. the charged eflow object, and the energy deposits in each calorimeter layer are shown in the subsequent panes. For panes in (a), calorime-

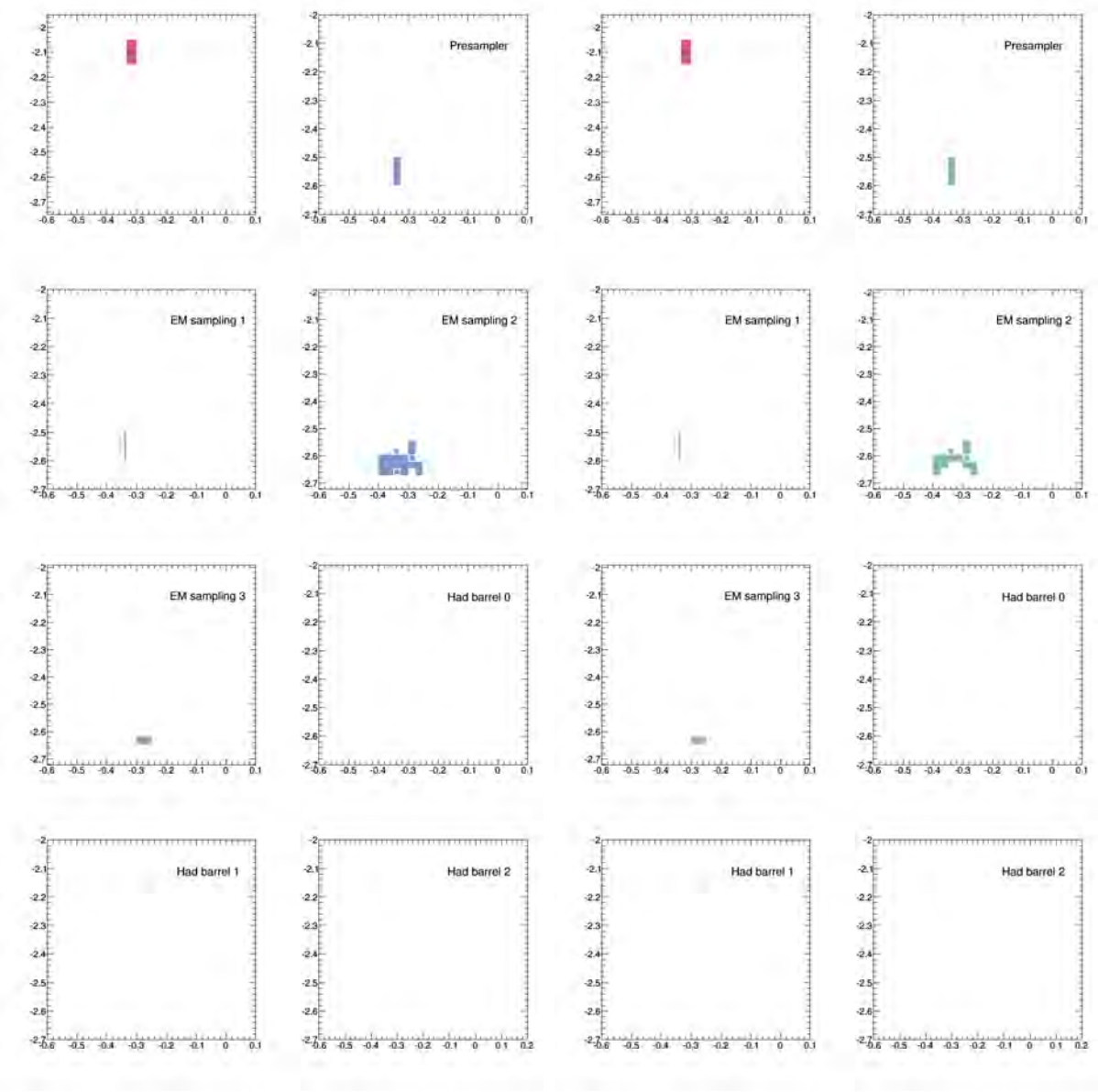

(a) calorimeter layers with extrapolated track coordinates (red) and truth energy-filled cells (blue).

(b) calorimeter layers with extrapolated track coordinates (red) and cells from reconstructed neutral eflow objects (green)

Figure 26: Calorimeter layers of a single charged pion event are shown for before eflow implementation (a), and after (b). The red cells present the extrapolated coordinates of the track, i.e. the charged eflow object. The left hand side shows cells in blue that contain truth energy, whilst the right hand side shows the surviving reconstructed neutral eflow objects in green and some cells containing truth energy have now been subtracted. The results after the eflow reconstruction are less than ideal: whilst some cells are subtracted in the EM sampling layer 2 (taken to be as part of the charged eflow object), the rest plus cells in the presampler, sampling 1 and sampling 3 are ignored and instead passed as a neutral eflow object.

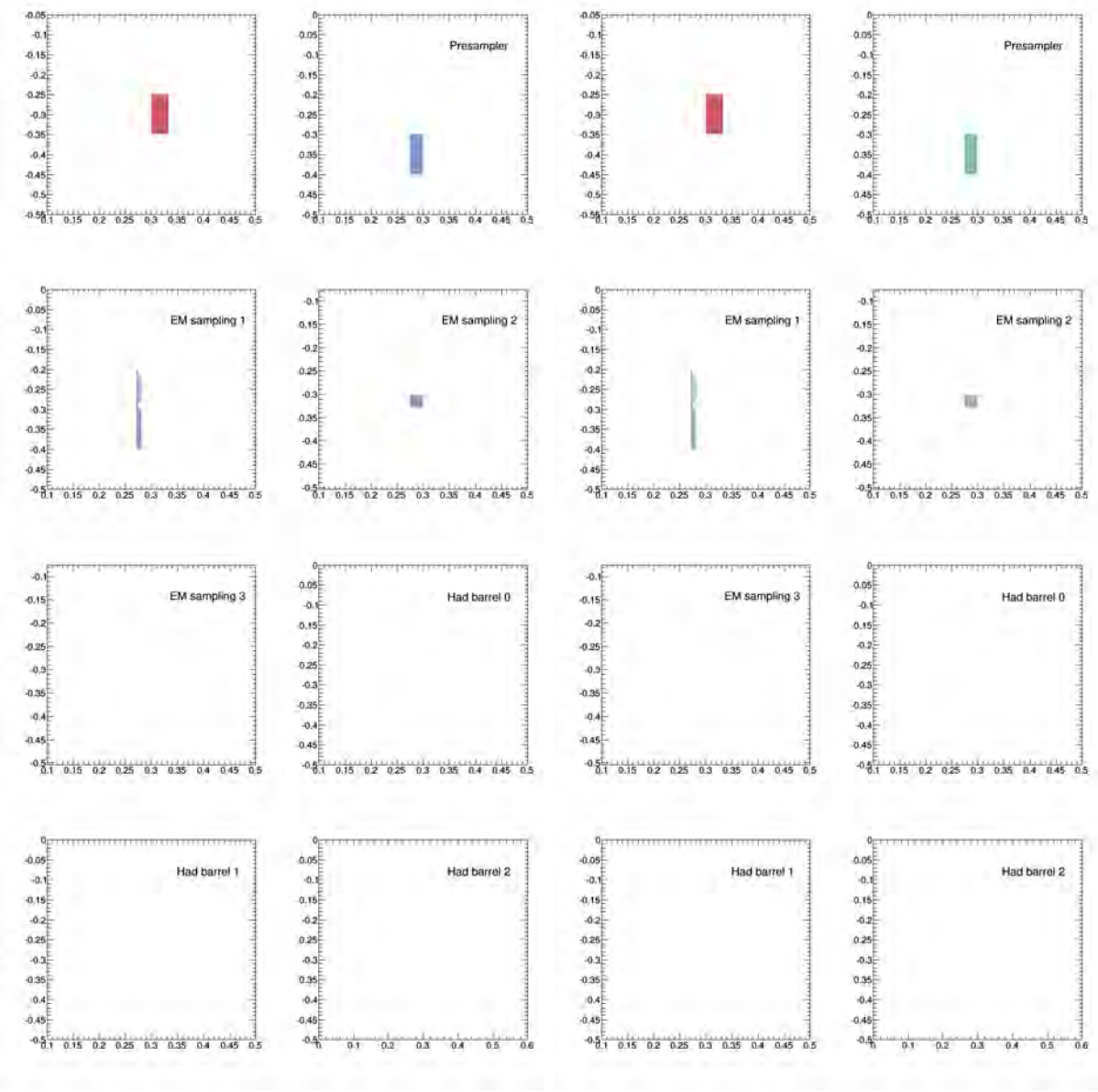

(a) calorimeter layers with extrapolated track coordinates (red) and truth energy-filled cells (blue).

(b) calorimeter layers with extrapolated track coordinates (red) and cells from reconstructed neutral eflow objects (green)

Figure 27: These are the calorimeter layers of another single charged pion event in which the eflow reconstruction was not completely successful. The layout is the same as in Figure 26. Although calorimeter hits are present in the Presampler and the first 2 EM layers, no calorimeter hits are associated to the track lying within a $dR = 0.2$ radius cone and are instead reconstructed as a neutral eflow object.

ter cells are coloured in blue and signify cells filled with truth energy. In (b), cells are coloured in green and indicate those cells that became part of a neutral eflow object after the particle flow algorithm was implemented in the event; cells of truth energy that were used for the reconstruction of the charged eflow object have been subtracted.
Events with surviving neutral eflow objects were studied and it has given us an idea where things go wrong. Figure 26 shows that if a particle deposits its energy over several layers, some hits in the deeper layer are missed as belonging to the charged particle and clustered to become a separate neutral eflow object. It appears that even if energy corresponding to the track has been subtracted, the remaining energy can be of a high enough fraction to pass the test condition for a neutral eflow object. The case is worse in Figure 27, where no cells have been subtracted. If, upon finding that the nearest cluster to the track did not carry sufficient energy, the algorithm implemented the Split Shower Recovery, then it appears to have found no cells within a radius of $dR < 0.2$ to subtract. However, there are several cells located within that cone, distributed across several layers, which the algorithm missed. The reason for this is not yet understood.

5.1.5 Conclusions

Single pion events were studied in order to better understand clustering behaviours in the calorimeter. The effects of noise thresholds were investigated as well as two cluster events in order to understand what happens when a single particle results in two reconstructed clusters. Finally, studies were performed on the reconstruction efficiency of eflow objects themselves.

A high threshold value is required given the studies of cluster numbers in single particle events. When increasing the noise threshold from zero to 30, the number of clusters per single neutral pion event is reduced from 12 to one.
A significant fraction of events contain two or more clusters. In two cluster events of a flat logE distribution, for a third of events, the second cluster had less than 5% of the total pion energy. This, however, changed when looking at low (1 GeV) energy pion events. Here the energy distribution between the two clusters ranged evenly from almost all energy in the one cluster to the pion energy being split in half between both clusters. As the amount of splitting in the $\eta - \phi$ plane is however relatively small, the Split Shower Recovery algorithm should be able to recover these split clusters.
Inherent problems within the eflow reconstruction algorithm were found. For a threshold value of 30, 87% of 1 GeV charged pion events contained one charged eflow object which is consistent with the track efficiency at that momentum range. Here also 81% of events containing a charged eflow object contained no neutral eflow objects close to the truth cluster. However, 19% of events did include neutral eflow objects. Studying these neutral eflow events by layers, it is yet to be understood why the eflow reconstruction algorithm failed in these cases.

Whilst a $\sim$ 87% success rate for eflow reconstruction is good, examining the subset of cases where the eflow reconstruction algorithm was unsuccessful would be an interesting extension to this analysis. This is especially true considering that this analysis worked with very clean and simple single particle events. Situations will become exceedingly worse once other particles from the main event, particles from the underlying event and particles from pile-up are included.

5.1.6 Additional: Jet Resolution Results from the particle flow ATLAS group

As stated at the beginning of this section, it is expected that the implementation of particle flow will improve the jet energy resolution at low p_T. The performance of various jet calibration schemes is shown in Figure 28. ATLAS currently uses the EM+JES+GSC scheme. Here, jets are reconstructed from clusters at the EM-scale (no corrections), after which jet energy scale (JES) corrections are applied to each jet to correct for the non-compensating nature of the calorimeter for hadronic signals, loss due to dead material, leakages and jet reconstruction inefficiencies. The other option is doing a local calibration (LC) at cluster level, so that cluster inputs for jet reconstruction are at the hadronic scale. A global sequential calibration (GSC) is additionally implemented which performs several energy corrections in sequence based on the topology of the calibrated jet. It improves the resolution by smoothing out fluctuations in the internal jet structure [50].
The implementation of particle flow after a EM+JES+GSC calibration is shown to improve the jet resolutions for low p_T jets (Figure 28). At around 50 GeV the EM+JES+GSC and Pflow+EM+JES+GSC calibration schemes perform equally well. At higher p_T, the EM+JES+GSC and LC+JES+GSC yield the best resolution.

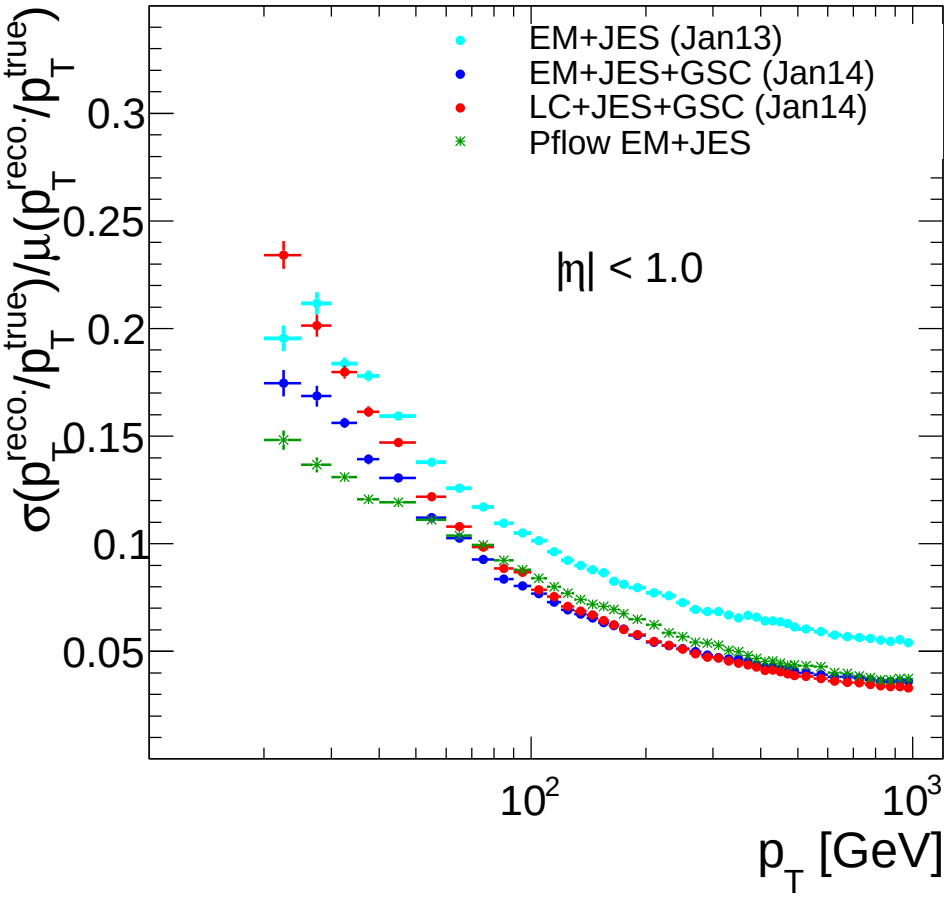

Figure 28: The jet resolution in the central η region for different jet calibrations. Particle flow is shown to yield the best jet resolution at low (< 50 GeV) p_T ranges.[51]

6 tH Analyis

Constraints on the fermionic and bosonic coupling of Standard Model particles to the newly discovered Higgs-like particle have been obtained from fits by both ATLAS and CMS (for more explicit details on the theory behind this analysis, refer to Section 2.2). Whilst all Higgs boson decay channels can probe the magnitudes of certain couplings, only one channel, $H \to \gamma\gamma$, probes the *relative signs* between the fermionic and bosonic coupling. However, statistics from this channel alone are not high enough to resolve the sign.
In such fits, the vector bosonic and fermionic couplings relative to the SM prediction are defined as

$$c_V(\kappa_V) \equiv g_{hVV}/g_{hVV}^{SM} \qquad \text{and} \qquad c_F(\kappa_F) \equiv g_{hff}/g_{hff}^{SM}. \tag{19}$$

Fits to these parameters, where c_V is restrained to positive values, result in a minimum close to the SM value, $c_V = c_F = 1$. In addition, a second, non-Standard Model, minimum appears around $c_V = 1$ and $c_F = -1$.
In order to lift this degeneracy in minima, further channels associated to the Higgs particle and sensitive to the relative signs of the couplings are needed. A promising channel is the single top production process in association with the Higgs (tH), where two prominent processes are possible; one bosonic and the other fermionic. This process does not however have a large cross-section.

This analysis seeks to estimate, at a truth level, the feasibility of measuring the tH signal in $H \to b\bar{b}$ over the large background using the ATLAS experiment at the LHC at $\sqrt{s} = 8$ TeV and 21 fb^{-1} of data. The sensitivities of the tH signals for the universal fermionic coupling value at each minimum in the present experimental fits are investigated.

The relevant tree-level process at proton-proton collisions is $Wb \to tHj$. A top quark and a Higgs boson are produced along with a jet that is characteristically directed in the forward η regions.
The dominant decay of the top quark is Wb (at 99.8% probability). The leptonic decay of the W boson, $W \to \ell\nu$ ($\sim 30\%$), serves as a 1 lepton trigger, where the term 'lepton' only refers to electrons and muons (taus will be ignored in this study). As neutrinos are not detected directly, the neutrino energy will be measured using missing transverse energy, $E_{\mathrm{T}}^{\mathrm{miss}}$. As the decay channel sought for the Higgs boson is $H \to b\bar{b}$, the final signature of the process is $tHj \to$ 3 b-jets+1 forward jet + $\ell^{+/-}$ + $E_{\mathrm{T}}^{\mathrm{miss}}$.

6.1 Signal and Backgrounds

A background can either be reducible or *ir*reducible. Irreducible means that the final state particles in the background are identical to those in the signal. Reducible means particles are misidentified as the same type as the particles being sought. For instance, a charm quark may be misidentified for a bottom quark

as a charm quark has an intermediate mass and a lifetime not too different from a bottom quark. Unlike the irreducible backgrounds that are indistinguishable from the signal, most of the reducible background can be removed during event selection.

The signal and backgrounds, their associated cross-sections and the number of Monte Carlo (non-normalised) events used, are given in Table 2[3]. Two samples were generated for the tH signal: one for the SM case with $c_F = 1$ and another for the non-SM case with $c_F = -1$. In both cases $c_V = 1$. Two large reducible backgrounds are the $t\bar{t}$ and $t\bar{t}j$ processes. Here, the second top quark decays as $t \to bc\bar{s}$, where the c or $\bar{s}$ are mistagged as a b-jet. Two further irreducible backgrounds are $tbbj$ and $tZbbj$, where the two b-jets originate from the $Z \to b\bar{b}$ decay. All samples include a leptonic top quark decay: the single top quark in the signal, $tbbj$ and $tZbbj$ samples, and at least one of the tops in the $t\bar{t}$ sample decays leptonically always. In the case of the $tbbj$ sample, taus were not generated; this does not affect the study as taus are ignored.

Table 2: Details for the SM signal, non-SM signal and all backgrounds considered

Process	Cross-Section (fb^{-1})	Generator	Number of MC events
$c_F = +1$ tH	1.66	MadGraph + Pythia	40 000
$c_F = -1$ tH	27.81	MadGraph + Pythia	40 000
$tb\bar{b}j$	11.28	MadGraph + Pythia	39 999
$tZbbj$	6.27	MadGraph + Pythia	40 000
$t\bar{t}(j)$	210.85×10^3	POWHEG+ Pythia	569 7995

The $t\bar{t}(j)$ background has a cross-section 10 000 times larger than the $c_F = -1$ signal and suppressing this background is the biggest challenge of the analysis.

6.2 Event Selection

Requirements are set to select the signal and minimise the backgrounds. The objects that are studied are leptons, b-jets, jets directed in the forward region and $E_{\mathrm{T}}^{\mathrm{miss}}$ due to the escaped neutrino. Several distinctions between background and signal are drawn and, based on these, effective criteria applied.

The complete set of implemented criteria is laid out in Table 3 along with the significance after each criterion. The details of each criterion are described in the following section.

[3]Names of the Monte Carlo datasets are given in Appendix A

Table 3: A summary of the criteria applied for event selection, the normalised number of events after each criterion for each sample, as well as the running significance value.

criterion	$\kappa_F = +1$	$\kappa_F = -1$	tbbj	tZbbj	$t\bar{t}$	Σ(bg)	$\frac{S}{\sqrt{B}}$ (SM)	$\frac{S}{\sqrt{B}}$ (non-SM)
initial	35	592	240	134	4491105	4491479	0.02	0.28
1 lepton	18	325	180	67	2217352	2217599	0.01	0.22
1 fwd jet	7	136	58	24	258299	258381	0.01	0.27
$\geqslant$ 3 central jets	6	122	44	20	193120	193184	0.01	0.28
$\geqslant$ 2 b-jets	6	119	41	20	134949	135009	0.02	0.32
$\geqslant$ 3 b-jets	4	88	25	13	2903	2940	0.08	1.63
m_{bb}	2	62	12	8	1254	1274	0.08	1.74

6.2.1 Acceptance criteria: p_T, η and lepton number

In Section 4.4, standard kinematic acceptance requirements motivated by the detector efficiency were described. These were a p_T and $|\eta|$ requirement of > 25 GeV and < 2.5 respectively. These requirements are applied in the present analysis, with the exception of the forward jet, for which the η requirement is $|\eta| > 2.5$.

Additionally, as the trigger signal is a single lepton, another requirement is that exactly one lepton exists for the acceptance of an event. In Table 4 the distributions of the number of leptons per event is shown for each sample – with and without the kinematic acceptance criteria applied.

Table 4: Distribution of the number of leptons/event for each sample.

	without acceptance			with acceptance		
no. of leptons/event	0	1	2	0	1	2
$c_F = +1$:	33%	67%	0%	48%	52%	0%
$c_F = -1$:	33%	67%	0%	45%	55%	0%
$tbbj$	1%	99%	0%	25%	75%	0%
$tZbbj$	34%	66%	0%	50%	50%	0%
$t\bar{t}$	29%	62%	9%	44%	51%	5%

Except for the $t\bar{t}$ sample, all samples studied include a single top quark decaying leptonically and thus one expects one lepton per event in these cases. The $t\bar{t}$ sample has two tops, one of which decays leptonically whilst the other does likewise or decays hadronically. Events with one lepton and two leptons are thus expected.

As τ leptons are ignored in this truth study, without acceptance requirements, around 33% of events are not counted as the leptonic decay is to a τ lepton. This is evident in the left side of Table 4 (save for the $tbbj$ sample since taus were not generated here).
Referring to the right side of Table 4, it appears that the kinematic acceptance requirement evens out the distributions somewhat. There is now almost a $50-50$ split between zero and one lepton events for all samples other than $tbbj$. There is a lower acceptance for leptons for $c_F = +1$ compared to the $c_F = -1$ case. This is likely because the average p_T value of the leptons is around 45 GeV for $c_F = +1$ and 50 GeV for $c_F = -1$. The significance after a 1 lepton requirement for the $c_F = +1$ and $c_F = -1$ cases are 0.01 and 0.22 respectively (Table 3).

6.2.2 η Distributions

The η distributions of the top quark and Higgs boson decay products in the signal and backgrounds are compared in Figure 29.
Figures 29a and 29b compare the distributions of the forward jet, the b quarks from the Higgs boson and the top quark and the lepton in the SM and non-SM case respectively. A slight difference is evident in the η distributions for b quarks from the top quark and the Higgs boson. These appear more forward directed in the SM $c_F = 1$ case (an RMS of $\eta \sim 1.25$ compared to $\eta \sim 1.06$). This is due to the top and the Higgs particles being more centrally produced in η ranges for smaller c_F values, as noted in [19] and [52]. Figures 29c and 29d present the same η distributions for the $tbbj$ and $tZbbj$ events, where the pair of b jets now originate from the initial collision and the Z-boson respectively. It is found here that the distributions very much mimic the signal events. In Figure 29e the distribution comparison for the $t\bar{t}$ events are shown, excluding the b quark pair (as this pair is not defined at quark level in the $t\bar{t}$ sample). The most notable difference is the absence of light quarks at high η in these events as compared to the other samples. In the case of the other samples, the light quark is a by-product of the initial proton-proton process and is emitted in a direction closer along the beam axis. In the $t\bar{t}$ process, however, it is a subsequent product of the top quark decay and the distribution of its direction is thus more centrally concentrated.
As the forward jet is expected to be one of the highest p_T jets, it is required that at least one of the top 2 highest p_T jets in the event lies at $|\eta| > 2.5$. Referring to Table 3, the effect of the forward jet requirement is a significance of 0.01 for $c_F = +1$ and 0.27 for $c_F = -1$.

6.2.3 Jet number requirements

In Figure 30 the number of b-jets (the definition of which at truth level is given in Section 4.4) per event are shown for each sample: Figure 30a is scaled by the fraction of events, whilst Figure 30b is scaled to the true cross-section of the relevant process.

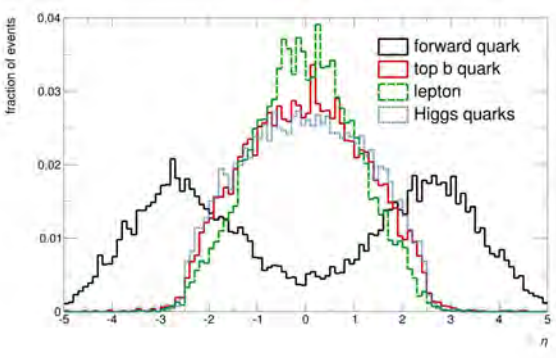

(a) signal $c_F = 1$

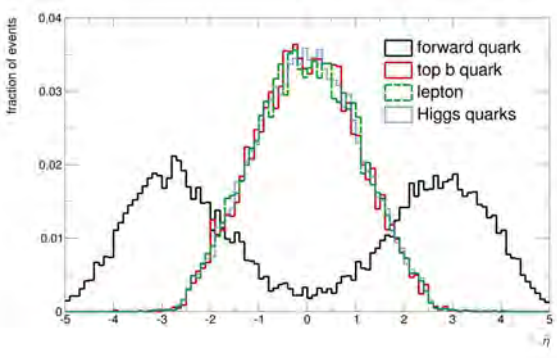

(b) signal $c_F = -1$

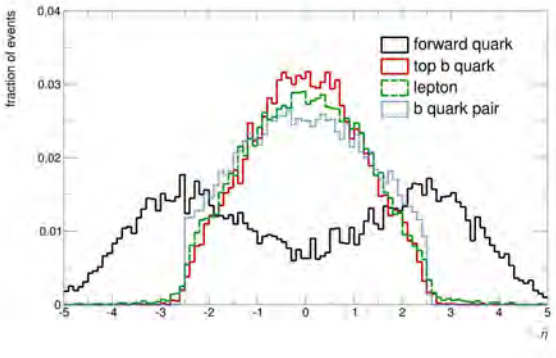

(c) $tbbj$

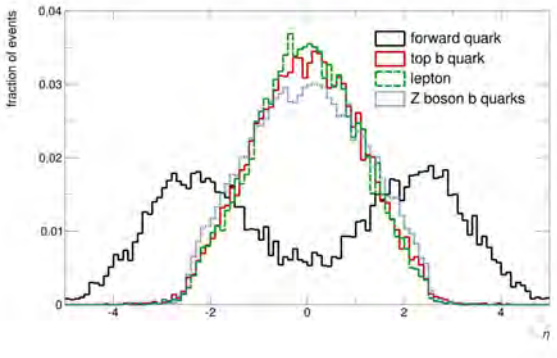

(d) $tZbbj$

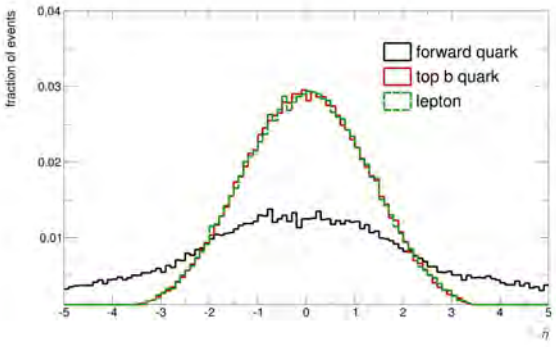

(e) $t\bar{t}$

Figure 29: η comparisons: the distributions of MC truth η of light (non-b) quarks (grey), Higgs (or Higgs candidate) b quarks (blue), the top b quark (red) and leptons (green) are shown for each sample.

The $t\bar{t}$ process actually contains no more than two b quarks, thus this background can be significantly reduced by setting a threshold on the number of b-jets. Referring to the histograms in Figure 30, it is clear that the $t\bar{t}$ background can be reduced by as much as 99% by requiring that three or more b-jets exist: the majority of $t\bar{t}$ events either have two b-jets or one b-jet (one b quark is missed). A third b-jet may appear in $t\bar{t}j$ events where the additional jet is a b-jet. Roughly 34% of the signal events produce less than 3 b-jets and around 15% 4 b-jets. The 25 GeV requirement is evidently more effective in the $tbbj$

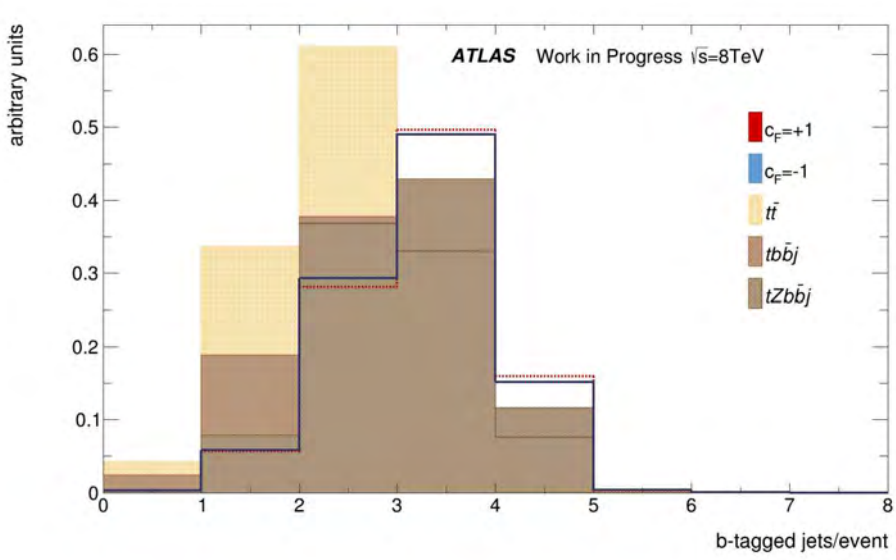

(a) The number of b-jets per event for each sample normalised to the same area. Acceptance requirements are applied.

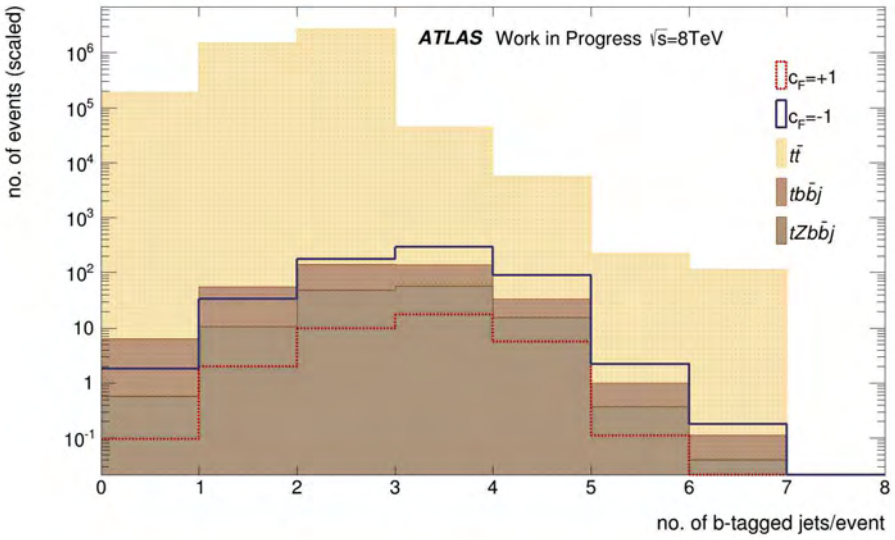

(b) The number of b-jets per event for each sample scaled by the relevant cross-section and integrated luminosity of 21 fb^{-1}. Acceptance requirements are applied, and all background samples are stacked.

Figure 30: Histograms of the number of b-jets per event are shown for different samples: backgrounds are presented in different shades of orange, the $cF = +1$ signal in red and the $cF = -1$ signal in blue. In (a), the counts are shown normalised to the same area, whilst in (b), the background samples are stacked and counts are normalised to the expected number of events at 21 fb^{-1}.

and $tZbbj$ events, as a smaller fraction of 3 b-jet events remains. Subsequently, keeping all events with 3 b-jets or more leads to a $\sim 34\%$ reduction in signal events, $\sim 45\%$ in tZbbj events, $\sim 59\%$ in $tbbj$ events and a fine $\sim 99\%$ reduction in $t\bar{t}$ events. However, mistagging is not applied in the present truth level analysis. At a reconstructed level this selection will not be as effective due to the b mistag rate of charm jets and, to a considerably lesser extent, of light jets (the mistag rate was discussed in Section 4.3). This will lead to a greater number of 3 b-jet events originating from the $t\bar{t}$ process. In order to give a sense of the range in which the $t\bar{t}$ process will be reducible, two additional requirements are added in between: 3 or more central jets per event, and then 2 or more b-jets per event, after which the significance lies at 0.02 for $c_F = +1$ and 0.32 for $c_F = -1$. After applying the final ≤ 3 b-jet requirement, the significance values are boosted to 0.08 for $c_F = +1$ and 1.63 for $c_F = -1$. It is evident that the 3 b-jet requirement is a considerable improvement.

6.2.4 Higgs boson mass reconstruction

The salient difference between the signal and the backgrounds is the presence of the Higgs boson. This means that the invariant mass of two of the b-jets in a signal event combined should reconstruct to a value that is consistent with the Higgs boson mass and can thus be used as a discriminating variable for the signal extraction.

First it needs to be understood how well jets identified as from a Higgs boson decay, describe the mass of the Higgs boson. Correct jets are found by matching jets to b quarks from the Higgs boson decay as described in Section 4.4. If a unique jet is successfully matched to each b quark from the Higgs boson decay, then the two jets are combined to compute their invariant mass. Around 77% of b-jets from the Higgs boson decay are successfully matched to a b quark and for these the reconstructed mass distribution is shown in Figure 31.

A Bukin function [53] was fit to indicate the mean at 116 GeV, which is lower than the actual Higgs boson mass. This is due to parton radiation discussed in Section 4.4.

In reality, it is not all that trivial to identify jets that are products of a Higgs particle. A jet pair from a background event can look surprisingly similar to a pair from Higgs particle production. In order to reduce the number of b-jet pair combinations, the top particle is first reconstructed and the b-jet used to reconstruct the top quark is excluded from the Higgs boson mass reconstruction.

All signal and background samples considered contain a W boson and a top quark. Thus, after identifying the b-jet from the top quark decay, the remaining 2 b-jets (in 3 b-jet events) can be expected to produce a reconstructed mass consistent with the mass of the Higgs boson for the signal samples, but inconsistent for the background samples where no Higgs particle exists.

The pre-selection requirements were applied before particle masses were reconstructed. After permuting through all 3 or 4 b-jets in the event, the b-jet that together with the reconstructed W boson lies closest to the top quark mass, is selected. Figures 32a and 32b show the reconstruction of the W boson mass

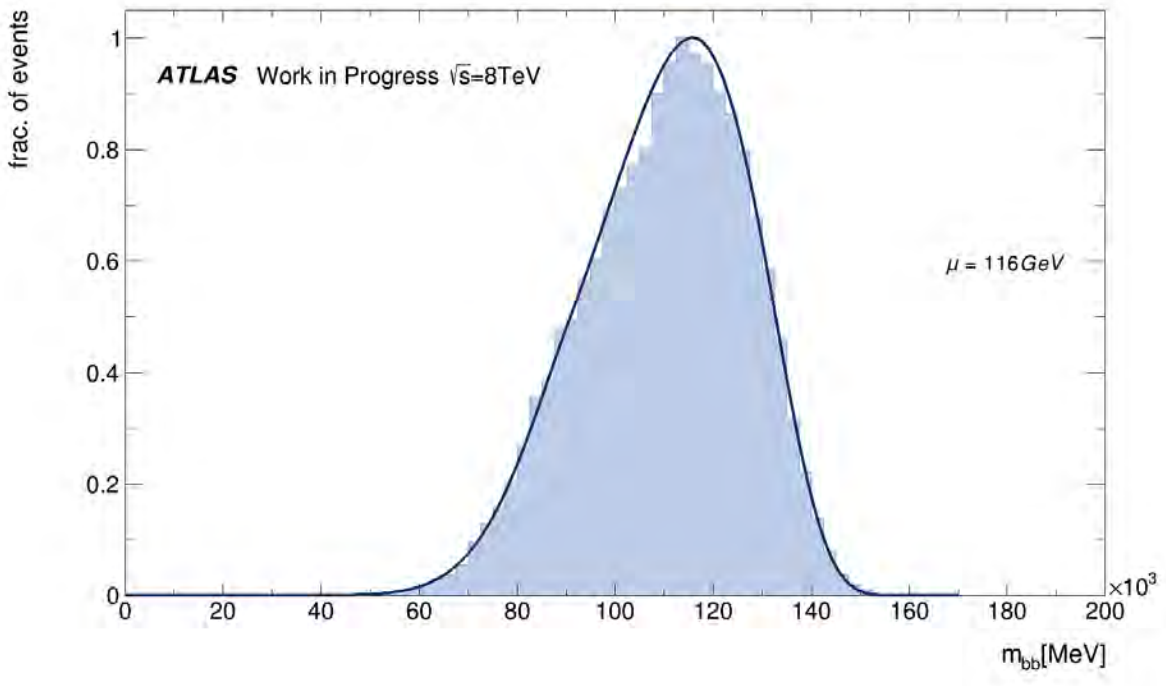

Figure 31: Histogram of the reconstructed mass of b-jet pairs matched to b quarks from the Higgs boson decay. The standard p_T and η requirements are applied. A jet is matched to a b quark by requiring $|\delta R| < 0.4$ and $0.4 < p_T^{jet}/p_T^{quark} < 1.2$.

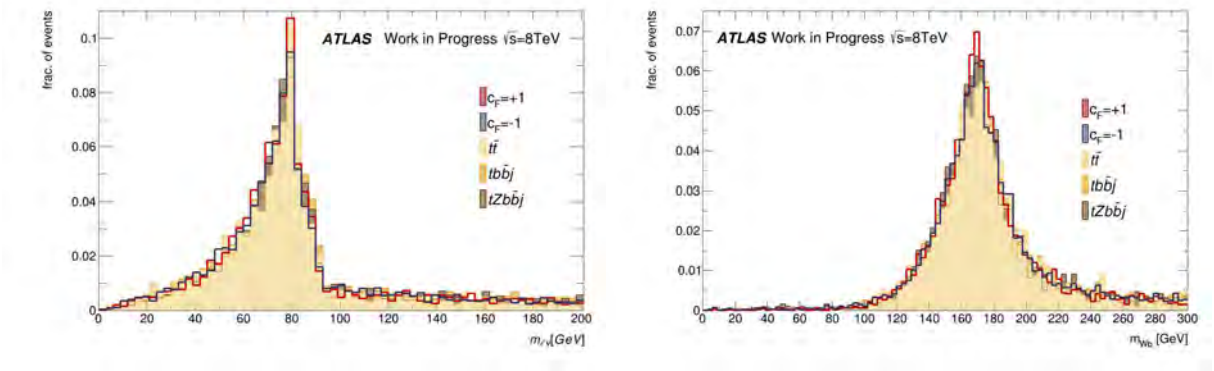

(a) Histogram of the invariant mass of the lepton plus $E_{\mathrm{T}}^{\mathrm{miss}}$ for each sample.

(b) Histograms of the closest-to-top-quark mass reconstruction for each sample, where the reconstructed W boson in (a) and a b-jet are combined.

Figure 32: Histograms of the reconstructed W boson (a) and the reconstructed top quark (b) are shown. All selection requirements have been applied.

following the method in Section 4.4 and the resulting top quark mass for the best match b-jet. No significant differences are observed between the samples. Using one of the signal samples the rate at which the correct b-jet was chosen for top quark mass reconstruction (the b-jet matched to the b quark from the top quark decay) was tested. Although all samples exhibit clear peaks, only 51% of the time the correct jet is chosen.

Finally, in Figure 33a the invariant mass of the remaining b-jets is shown. If the event contains four b-jets, the pair closest to the Higgs boson mass is chosen. The plot demonstrates the shape of the m_{bb} distribution for each process. The signal samples have the most defined peak, corresponding to the Higgs boson mass, as expected. The shape for $tZbbj$ also exhibits a dominant peak, but at the Z boson mass (91 GeV), as expected. The shapes for $t\bar{t}$ and $tbbj$ are flatter and lack a distinct peak, because the b-jets are not produced through resonant production. For comparison, the m_{bb} distribution for the non-SM signal is overlaid with the truth matched jets m_{bb} distribution in Figure 33b, in order to give an idea of the goodness of the reconstruction. The efficiency of selecting both correct b-jets (the b-jet matched to a b quark) is only 50% which is why the reconstructed distribution appears comparatively smeared. The top quark mass distribution, on the other hand, is narrower compared to the distribution where the b-jet is truth matched (Figure 17). This is a result of the high selection of combinations between 3 or more jets during the top quark mass reconstruction. It is noted that a multivariate technique for the simultaneous reconstruction of the top quark and Higgs boson would likely improve this.
Finally, Figure 34 shows the m_{bb} distribution with all processes normalised and stacked, for $c_F = -1$. Additionally, the non-stacked distribution for both signal samples are shown in comparison. It was found that applying a 65 GeV $< m_{bb} <$ 145 GeV threshold on events yielded the best significance, giving 0.08

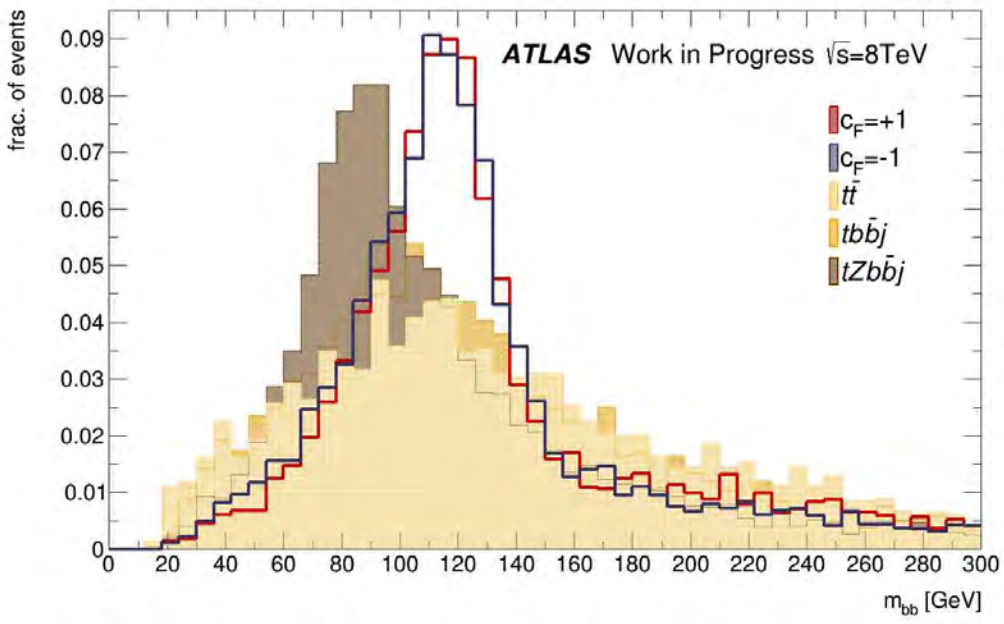

(a) Histograms of the invariant mass of b-jet pairs. The b-jet that is used for the top quark reconstruction is eliminated and the remaining pair of jets (or the pair that reconstructs closest to the Higgs boson mass in the case of a 4 b-jets event) are used.

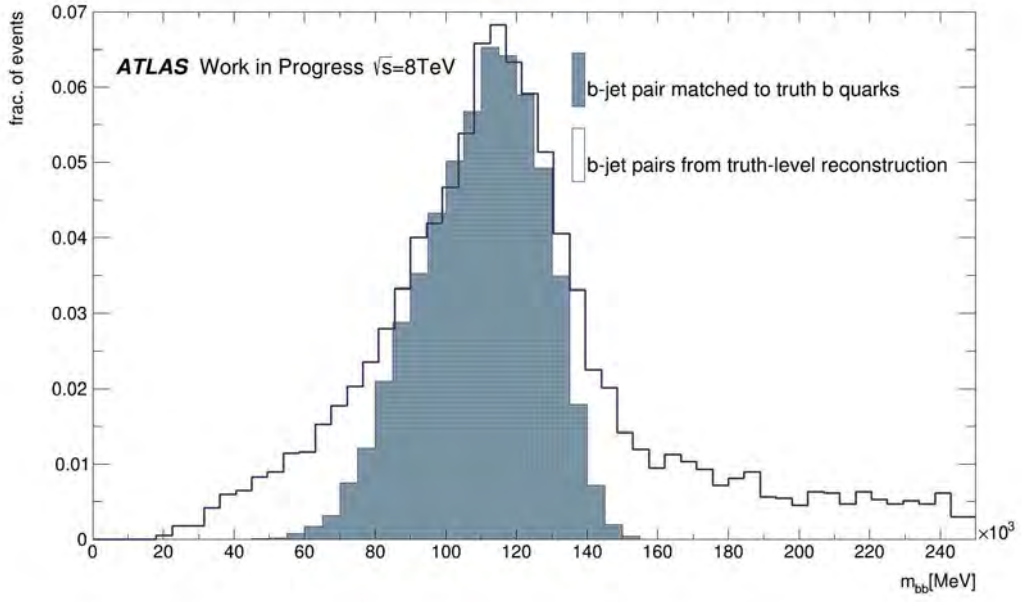

(b) The invariant mass distribution of b-jet pairs for signal $c_F = -1$ as the one in (a), overlaid with the distribution for the truth matched b-jet pair (Figure 31)

.

Figure 33: The Higgs boson mass reconstruction is shown for each sample in (a). The Higgs boson mass distribution for the $c_F = -1$ sample is shown in (b) again, along with the distribution for truth matched jets from the Higgs boson decay for comparison.

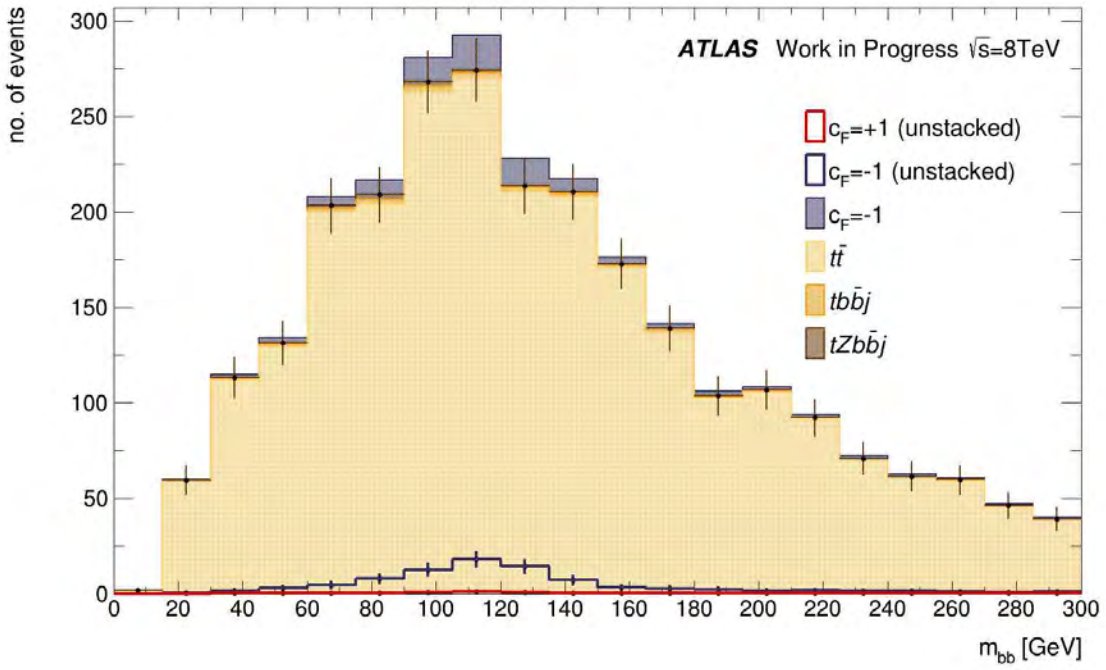

Figure 34: The final expected distribution of m_{bb} for $c_F = -1$, where background and the non-SM signal are normalised and stacked. The distributions for both signal $c_F = +1$ and $c_F = -1$ are also plotted as non-stacked distributions.

for $c_F = +1$ and 1.74 for $c_F = -1$.

The stacked plot in Figure 34 is the distribution expected to be observed when looking for the non-SM $c_F = -1$ signal in real data. An excess of 62 ± 1 events over a background of 1274 ± 16 events is expected in the region 65 GeV $< m_{bb} <$ 145 GeV (where uncertainties quoted are statistical uncertainties only).

6.2.5 jjb selection

The b-tagged and two additional high p_T non-b-tagged jets originate from the hadronically decaying top quark in the case of the $t\bar{t}$ events. One can thus expect the invariant mass of these three jets to lie close to the top quark mass at 175 GeV and the two non-b-tagged jets to lie close to the W boson mass. For the signal samples, this invariant mass is expected to be larger than the top quark mass, as one adds an additional jet to the two b-jets from the Higgs boson which already has a high mass. In studies done in [7] and [54] setting a lower limit on the jjb mass was thus suggested.

The non-SM $c_F = -1$ signal and the $t\bar{t}$ events are compared in the following figures to establish the effectiveness of a m_{jjb} threshold. In Figure 35a, the invariant mass of the top two p_T jets are shown. These jets do not include the b-jet used for the top quark reconstruction nor the highest p_T b-jet from the candidate Higgs pair, which is instead combined with the jet pair in order to obtain the m_{jjb} distribution in Figure 35b.

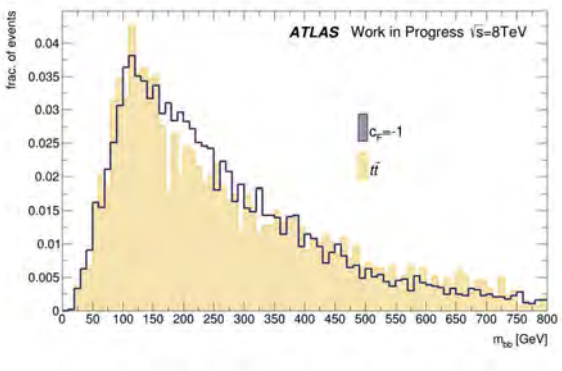

(a) Histograms of the jj mass reconstruction for non-SM $c_F = -1$ signal and $t\bar{t}$ events. The top two p_T jets in the event were used, excluding the selected b-jet for top quark reconstruction and the highest p_T jet from the Higgs candidate pair.

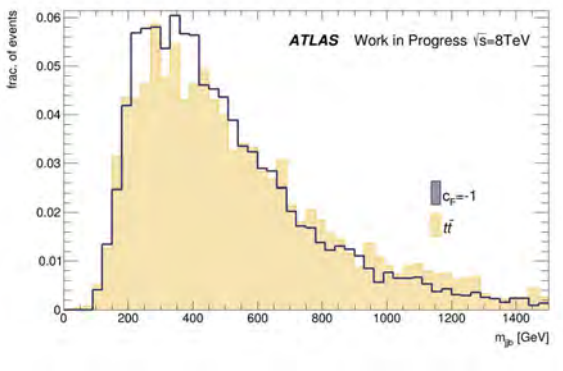

(b) Histograms of the jjb mass reconstruction for non-SM $c_F = -1$ signal and $t\bar{t}$ events. The jets from plot (a) are combined with the highest p_T jet from the Higgs candidate pair.

Figure 35: The invariant mass distributions of jets are studied in search for discriminating behaviour between the signal and $t\bar{t}$ background due to the effects of the second top quark in $t\bar{t}$ as suggested in previous studies. Clear deviations are not apparent.

Looking at the resulting distributions, it is not obvious that a lower limit on m_{jjb} will contribute to the significance. The distributions extend to high values in both cases. Therefore this section requirement was not applied in this study.

7 Discussion

7.1 Discussion of significance values

The significance, defined as $S/\sqrt{B}$, after all selection requirements is 0.08 in the $c_F = +1$ case and 1.7 in the $c_F = -1$ case. It is clear that for the Standard Model scenario the signal is very low because of the low cross-section of the process. With present data it would be difficult to distinguish it from background noise. For the non-SM scenario the situation is improved due to its enhanced cross-section, however a significance value of >= 3 is needed to claim evidence of this hypothesis. This would be reached with 65 fb^{-1} of integrated luminosity.

The addition of systematic uncertainties involved in measuring real data weakens the sensitivity further. This is shown in Table 6 for estimated systematic uncertainties of 5, 10 and 20%, where the significance is now greatly reduced to below 1σ for the $c_F = -1$ signal. Systematic uncertainties were described in Section 4.3.4 and a summary is given in Table 5. A dominant uncertainty is expected to come from the theoretical $t\bar{t}$ cross-section: the uncertainty in this is already estimated to be at around 10%. The uncertainty on the jet energy scale is another dominant uncertainty, on the order of $\sim 5\%$. The JES uncertainty

Table 5: Summary of uncertainties that would be considered for an analysis at reconstructed level.

type of uncertainty	description
systematic	lepton reconstrution, identification and trigger efficiencies
	jet energy scale
	b-tagging efficiencies
	theoretical cross-section calculations
	uncertainty on integrated luminosity
	pile-up effects
signal/background modelling	renormalisation and factorisation scale factors
	choice of parton distribution function (PDF)
	initial/final state radiation (ISR/FSR)
	uncertainty on free parameters of SM

is propagated to $E_{\mathrm{T}}^{\mathrm{miss}}$ measurements, which subsequently affects the W boson mass reconstruction. Another significant effect is the mistagging of charm jets which are the most common decay products of W boson decays. This will not only increase the number of background events passing the $\leq$ 3 b-jet requirement but the large uncertainties (on the order $\sim 6-20\%$) in the tagging efficiencies will also be a prominent contribution to the overall systematic uncertainty. The widened jet resolution due to detector effects will smear the m_{bb} distributions across the cut limits, lowering the number of signal events falling within the acceptance window. Whilst the reconstruction efficiency of jets is high in the central region, the efficiency drops in the forward regions where the forward jet is detected. Subsequently, the requirement of a forward jet will decrease the acceptance. The reconstruction efficiencies and systematic uncertainties for leptons are very good and thus are not expected to degrade the results of the present analysis significantly.

The present analysis nevertheless highlights the main effects that play a role in the performance of this study.

Table 6: Summary of significance calculations in the SM and non-SM case. Included are calculations assuming systematic uncertainties of 5, 10 and 20%.

tH signal	$S/\sqrt{B}$	$S/\sqrt{B+(0.05B)^2}$	$S/\sqrt{B+(0.1B)^2}$	$S/\sqrt{B+(0.2B)^2}$
$c_F = +1$:	0.08	0.03	0.02	0.01
$c_F = -1$:	1.74	0.85	0.47	0.24

It is unlikely that 2012 data at 8 TeV and with 21.3 fb^{-1} of integrated luminosity is sufficient for the determination of the sign of the top Yukawa coupling scale factor.

7.2 Future Analysis Improvements

An interesting distinction between $t\bar{t}$ events and single top quark events is the asymmetry in the charge of the lepton that is produces in both cases. A single top quark produced out of the positive-charge-weighted collision of two protons will tend to carry a positive charge, and consequently a higher number of positive leptons will be detected. In [55] the asymmetry in the tb and tbq channels is said to lead to around $60-70\%$ more top quarks. Even more interesting is the asymmetry in $t\bar{t}$ decays. This is however only slight. Whilst symmetrical at leading order, at next-to-leading order, the $\bar{t}$ is more centrally produced and the t quark less so. Thus a positive lepton is more likely to fall out of the acceptance region. This asymmetry has been measured by both ATLAS and CMS, who report figures that are compatible with the Standard Model [56] [57].
The asymmetries are displayed in Table 7. Here the events of the $c_F = -1$ signal sample are used to show the $\sim 66\%$ dominance of positively charged leptons over the $\sim 33\%$ of negatively charged leptons. In contrast, a small $\sim 50.4\%$ dominance of negative leptons over a $\sim 49.6\%$ of positive leptons is evident in the $t\bar{t}$ sample.

Table 7: Lepton charge asymmetries for samples $c_F = -1$ and $t\bar{t}$.

	frac. pos. leptons	**frac. neg. leptons**
sample $c_F = -1$	66%	33%
sample $t\bar{t}$	49.6%	50.4%

The significant enhancement of positive leptons in the signal may prove useful. One can plot the distribution for m_{bb}, for positive and negative leptons separately, and next subtract the distribution for negative leptons from the distribution for positive leptons. This was done for the plot in Figure 36 for non-SM $c_F = -1$ signal and background events. The $t\bar{t}$ background is hereby essentially eliminated save for statistical fluctuations. The excess of positive lepton events in the signal means a peak remains. The peak however is small – at 1 event or less per bin. The small acceptance means more data will most likely be needed to make a good measurement.

7.3 Prospects for LHC Run II

The second and final run of the LHC is expected to commence early 2015. It will run at the LHC's design luminosity of $1.0 \times 10^{34} cm^{-2} s^{-1}$, an increase from $6 \times 10^{33} cm^{-2} s^{-1}$ during the first run. The energy too will be stepped up to $\sqrt{s} = 14$ TeV. The luminosity increase means it is expected that up to 100 fb^{-1} of data will be obtained by 2018. The increase in the centre-of-mass energy furthermore boosts

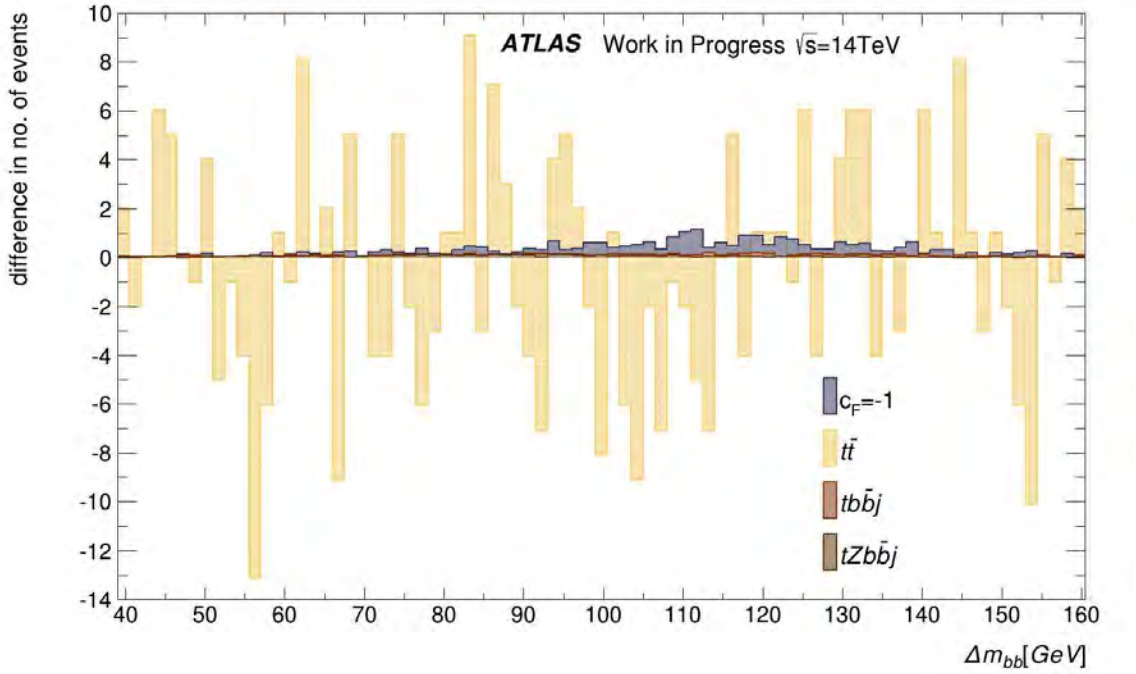

Figure 36: The remaining m_{bb} distribution after negative lepton events have been subtracted from positive lepton events, for the non-SM signal sample and all background samples.

the cross-sections of processes.

Considering these effects, the significance value for the tH process with $c_F = -1$ is projected to 14 TeV cross-sections and integrated luminosity, presented in Figure 37. Here, the projected significance is shown as a function of integrated luminosity. The significance values are calculated using the results from Table 3 and considering the 14 TeV over 8 TeV total cross-section ratios for the $c_F = -1$ tH process and the most significant background, the $t\bar{t}$ process. A summary of the 8 and 14 TeV total cross-sections for these two processes is given in Table 8. As branching ratios are not affected by higher collision energies, the ratios also hold for the partial cross-sections used in this work. The cross-section ratio for $c_F = -1$ is taken to be 4.2, according to NLO calculations given in [7]. The $t\bar{t}$ cross-section at 8 TeV is the calculated and measured cross-section stated in [58], whilst the 14 TeV cross-section is the one computed by the *HAdronic Top and Heavy quarks crOss section calculatoR (HATHOR)* [59] for a top quark mass of 173 GeV. The ratio for $t\bar{t}$ is taken as 3.5 then.

The luminosity curve shows that, if no systematic uncertainties are considered, around 15 fb^{-1} of statistics is sufficient to claim evidence of the non-SM signal if the expected significance is observed. However, even if a systematic uncertainty of 5% were assumed, the significance falls below the 2σ level, making this signal undetectable.

Table 8: Total cross-sections for the tH $c_F = -1$ and $t\bar{t}$ processes at 8 and 14 TeV. The ratio of these is used in the 14 TeV projection.

Process	8 TeV [fb]	14 TeV [fb]
tH ($c_F = -1$)	234	982
$t\bar{t}(j)$	240×10^3	833×10^3

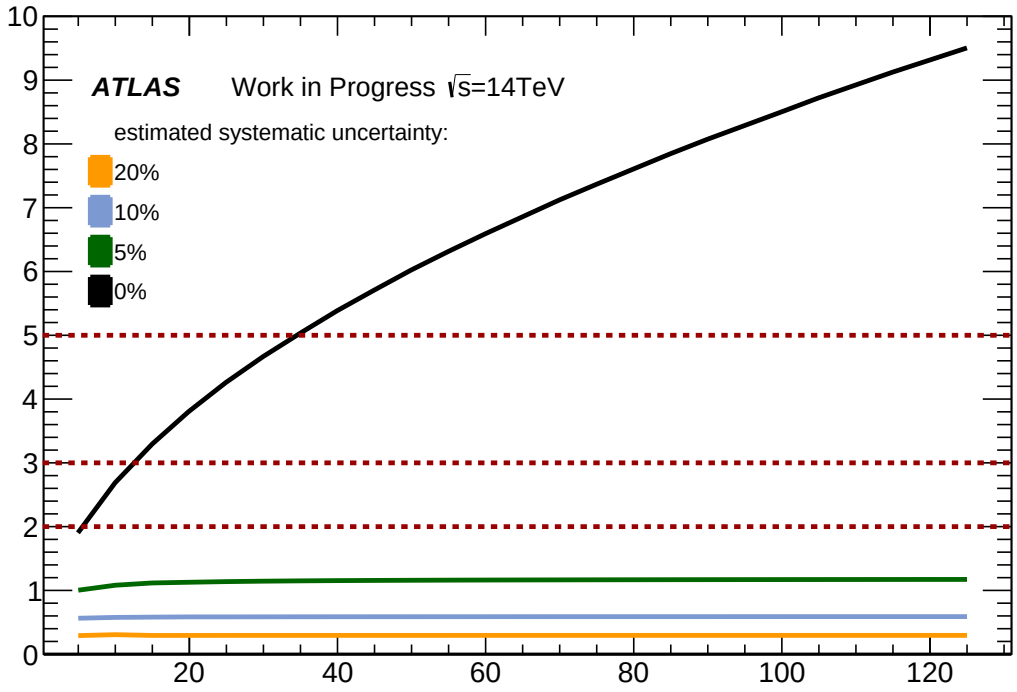

Figure 37: Significance value estimates for $c_F = -1$ signal events at 14 TeV are plotted as function of integrated luminosity, $\mathcal{L}$. The results from the present study at 8 TeV are rescaled to 14 TeV cross-section calculations. The effects of 5,10 and 20% systematic uncertainty limits in background on the significance are shown as a green, blue and yellow band, respectively.

8 Conclusion

The single top quark production in association with the Higgs boson (tH) was studied at truth level using Monte Carlo generations where the fermionic coupling factor, c_F, is set to 1 (SM value) and -1 (non-SM value), and the bosonic coupling factor, c_V is fixed at 1. This is according to coupling fits performed by ATLAS and CMS, in which it was found that whilst observations agreed with SM predictions, a non-SM

value of $c_F = -1$ was also compatible at the $\sim 2\sigma$ level. A way of resolving this degeneracy is the analysis of the tH process which is sensitive to the relative sign between the couplings c_F and c_V: due to a fermionic-bosonic interference, the cross-section for the smaller c_F value is roughly a magnitude larger.
The purpose of the study was to establish the feasibility of detecting the tH signal with 8 TeV data. It was found at truth level that significance values of 0.08 and 1.7 can be achieved for the $c_F = +1$ and $c_F = -1$ cases, respectively. For the SM scenario, the significance is too low for even an exclusion. For the non-SM scenario, an exclusion limit at 90% C.L. can be set at this sensitivity. However, even a low systematic uncertainty estimate of 5% degrades this significance to below 1σ level, making a meaningful exclusion unlikely even in the enhanced non-SM case.

The results of the feasibility study were used to project the significance to 14 TeV in anticipation of the LHC's upcoming run. The cross-sections were rescaled to match the new centre-of-mass energy. The prospects are not positive as even with a low systematic uncertainty of 5% in background the significance falls below the 2σ level. It is therefore unlikely that the Yukawa coupling will be resolved with the upcoming run.

A Datasets

Table 9: a list of MC datasets used for the tH analyis signal and background processes.

sample type	dataset
$c_F = +1$	$mc12\_8TeV.181098.MadGraphPythia8\_AU2CTEQ6L1\_tHbbj\_cfp1.merge.NTUP\_SMWZ.e1984\_s1581\_s1586\_r3658\_r3549\_p1328$
$c_F = -1$	$mc12\_8TeV.181098.MadGraphPythia8\_AU2CTEQ6L1\_tHbbj\_cfp1.merge.NTUP\_SMWZ.e1984_s1581\_s1586\_r3658\_r3549\_p1328$
$tb\bar{b}j$	$mc12\_8TeV.181096.MadGraphPythia8\_AU2CTEQ6L1\_tbbj.merge.NTUP\_SMWZ.e1984\_s1581\_s1586\_r3658\_r3549\_p1328$
$tZbbj$	$mc12\_8TeV.181094.MadGraphPythia8\_AU2CTEQ6L1\_tZbbj.merge.NTUP\_SMWZ.e1984\_s1581\_s1586\_r3658\_r3549\_p1328$
$t\bar{t}$	$mc12\_8TeV.117050.PowhegPythia\_P2011C\_ttbar.merge.NTUP\_SMWZ.e1727\_a188\_a171\_r3549\_p1328$

References

[1] ATLAS Collaboration. Observation of a new particle in the search for the Standard Model Higgs boson with the ATLAS detector at the LHC. *Physics Letters B*, 716(1):1 – 29, 2012.

[2] CMS Collaboration. Observation of a new boson at a mass of 125 GeV with the CMS experiment at the LHC. *Physics Letters B*, 716(1):30 – 61, 2012.

[3] ATLAS Collaboration. Combined coupling measurements of the Higgs-like boson with the ATLAS detector using up to 25 fb^{-1} of proton-proton collision data. Technical Report ATLAS-CONF-2013-034, CERN, Geneva, Mar 2013.

[4] CMS Collaboration. Combination of Standard Model Higgs boson searches and measurements of the properties of the new boson with a mass near 125 GeV. Technical Report CMS-PAS-HIG-12-045, CERN, Geneva, 2012.

[5] Georges Aad et al. Evidence for the spin-0 nature of the Higgs boson using ATLAS data. *Phys.Lett.*, B726:120–144, 2013.

[6] S. Chatrchyan et al. Measurement of the properties of a Higgs boson in the four-lepton final state. *Phys. Rev. D*, 89:092007, May 2014.

[7] Marco Farina, Christophe Grojean, Fabio Maltoni, Ennio Salvioni, and Andrea Thamm. Lifting degeneracies in Higgs couplings using single top production in association with a Higgs boson. *JHEP*, 1305:022, 2013.

[8] CMS Collaboration. Particle-Flow Event Reconstruction in CMS and Performance for Jets, Taus, and MET. Technical Report CMS-PAS-PFT-09-001, CERN, 2009. Geneva, Apr 2009.

[9] K. Kodama et al. Observation of tau neutrino interactions. *Phys.Lett.*, B504:218–224, 2001.

[10] Picture of the Standard Model of fundamental particles. `https://cdsweb.cern.ch/record/1473657/files/SMinfographic_image.png?subformat=`. Accessed: 2014-08.

[11] Peter W. Higgs. Broken Symmetries and the Masses of Gauge Bosons. *Phys. Rev. Lett.*, 13:508–509, Oct 1964.

[12] F. Englert and R. Brout. Broken Symmetry and the Mass of Gauge Vector Mesons. *Phys. Rev. Lett.*, 13:321–323, Aug 1964.

[13] J Beringer. Status of higgs boson physics. *Physics Review*, 010001(November 2013):1–192, 2014.

[14] ATLAS Collaboration. Measurements of Higgs boson production and couplings in diboson final states with the ATLAS detector at the LHC. *Phys. Lett. B*, 726(arXiv:1307.1427. CERN-PH-EP-2013-103):88–119. 38 p, Jul 2013.

[15] CMS Collaboration. Observation of a new boson with mass near 125 GeV in pp collisions at $\sqrt{s}$ = 7 and 8 TeV. *Journal of High Energy Physics*, 2013(6):1–127, 2013.

[16] J. Beringer et al. Review of particle physics. *Phys. Rev. D*, 86:010001, Jul 2012.

[17] F. Maltoni, K. Paul, T. Stelzer, and S. Willenbrock. Associated production of Higgs and single top at hadron colliders. *Phys.Rev.*, D64:094023, 2001.

[18] Sanjoy Biswas, Emidio Gabrielli, and Barbara Mele. Single top and Higgs associated production as a probe of the $Ht\bar{t}$ coupling sign at the LHC. *Journal of High Energy Physics*, 2013(1):1–16, 2013.

[19] Sanjoy Biswas, Emidio Gabrielli, Fabrizio Margaroli, and Barbara Mele. Direct constraints on the top-Higgs coupling from the 8 TeV LHC data. *JHEP*, 07:073, 2013.

[20] CMS Collaboration. Search for associated production of a single top quark and a Higgs boson in events where the Higgs boson decays to two photons at $\sqrt{s}$ = 8 TeV. Technical Report CMS-PAS-HIG-14-001, CERN, Geneva, 2014.

[21] Georges Aad et al. Search for $H \to \gamma\gamma$ produced in association with top quarks and constraints on the Yukawa coupling between the top quark and the Higgs boson using data taken at 7 TeV and 8 TeV with the ATLAS detector. *CERN-PH-EP-2014-179*, 2014.

[22] Lyndon Evans and Philip Bryant. LHC Machine. *Journal of Instrumentation*, 3(08):S08001–S08001, 2008.

[23] S.A. Bass, M. Gyulassy, Horst Stoecker, and W. Greiner. Signatures of quark gluon plasma formation in high-energy heavy ion collisions: A Critical review. *J.Phys.*, G25:R1–R57, 1999.

[24] Schematic of the LHC and injection chain. http://te-epc-lpc.web.cern.ch/te-epc-lpc/machines/lhc/general.stm. Accessed: 2014-08.

[25] J. Mnich. Status of the LHC. *Nuclear Physics B - Proceedings Supplements*, 205-206(C):2–9, 2010.

[26] Observation of a New χ_b State in Radiative Transitions to $\Upsilon(1S)$ and $\Upsilon(2S)$ at ATLAS. *Phys. Rev. Lett.*, 108:152001, Apr 2012.

[27] The ALICE Collaboration. The ALICE experiment at the CERN LHC. *Journal of Instrumentation*, 3(08):S08002, 2008.

[28] Joao Pequenao. Computer generated image of the whole ATLAS detector. Mar 2008.

[29] Figure of an actual $Z \rightarrow \mu\mu$ event at ATLAS. https://twiki.cern.ch/twiki/pub/AtlasPublic/EventDisplayStandAlone/2012_highPileup.png. Accessed: 2014-08.

[30] Scheme of the ATLAS inner detector. http://www.atlas.ch/photos/atlas_photos/selected-photos/inner-detector/combined/0803014_03-A4-at-144-dpi.jpg. Accessed: 2014-08.

[31] The ATLAS Collaboration. The ATLAS Experiment at the CERN Large Hadron Collider. *Journal of Instrumentation*, 3(08):S08003, 2008.

[32] T. Cornelissen, M. Elsing, S. Fleischmann, W. Liebig, E. Moyse, et al. Concepts, Design and Implementation of the ATLAS New Tracking (NEWT). *ATL-SOFT-PUB-2007-007, ATL-COM-SOFT-2007-002*, 2007.

[33] M Hodgkinson, D Tovey, and R Duxfield. Energy Flow Reconstruction with the eflowRec Combined Reconstruction Software in Athena 15.6.9.8. Technical Report ATL-PHYS-INT-2011-031, CERN, Geneva, Apr 2011.

[34] ATLAS Collaboration. *ATLAS liquid-argon calorimeter: Technical Design Report*. Technical Design Report. CERN, Geneva, 1996.

[35] Torbjorn Sjostrand, Stephen Mrenna, and Peter Z. Skands. PYTHIA 6.4 Physics and Manual. *JHEP*, 0605:026, 2006.

[36] Johan Alwall, Michel Herquet, Fabio Maltoni, Olivier Mattelaer, and Tim Stelzer. MadGraph 5 : Going Beyond. *JHEP*, 1106:128, 2011.

[37] Simone Alioli, Paolo Nason, Carlo Oleari, and Emanuele Re. A general framework for implementing NLO calculations in shower Monte Carlo programs: the POWHEG BOX. *JHEP*, 1006:043, 2010.

[38] Identification of the Hadronic Decays of Tau Leptons in 2012 Data with the ATLAS Detector. Technical Report ATLAS-CONF-2013-064, CERN, Geneva, Jul 2013.

[39] ATLAS Collaboration. *Expected performance of the ATLAS experiment: detector, trigger and physics*. CERN, Geneva, 2009.

[40] M. Cacciari, G. P. Salam, and G. Soyez. The anti-k_t jet clustering algorithm. *Journal of High Energy Physics*, 4:63, April 2008.

[41] L Asquith et al. Performance of Jet Algorithms in the ATLAS Detector. Technical Report ATL-PHYS-INT-2010-129, CERN, Geneva, Dec 2010.

[42] Search for the bb decay of the Standard Model Higgs boson in associated W/ZH production with the ATLAS detector. Technical Report ATLAS-CONF-2013-079, CERN, Geneva, Jul 2013.

[43] Search for the Standard Model Higgs boson produced in association with top quarks in proton-proton collisions at s = 7 TeV using the ATLAS detector. Technical Report ATLAS-CONF-2012-135, CERN, Geneva, Sep 2012.

[44] Commissioning of the ATLAS high-performance b-tagging algorithms in the 7 TeV collision data. Technical Report ATLAS-CONF-2011-102, CERN, Geneva, Jul 2011.

[45] Ringaile Placakyte. Parton Distribution Functions. *arXiv:1111.5452*, 2011.

[46] Measurement of the $t\bar{t}$ production cross-section in pp collisions at $\sqrt{s}$ = 8 TeV using $e\mu$ events with b-tagged jets. Technical Report ATLAS-CONF-2013-097, CERN, Geneva, Sep 2013.

[47] Measurement of t-Channel Single Top-Quark Production in pp Collisions at sqrt(s) = 8 TeV with the ATLAS detector. Technical Report ATLAS-CONF-2012-132, CERN, Geneva, Sep 2012.

[48] The Sheffield's group particle flow webpage. `http://www.hep.shef.ac.uk/research/atlas/eflow/`. Accessed: 2014-09.

[49] K Hamano, A Morley, and A Salzburger. Track Reconstruction Performance and Efficiency Estimation using different ID geometry samples. Technical Report ATL-COM-PHYS-2012-1541, CERN, Geneva, Oct 2012. plots for a poster at HCP.

[50] Georges Aad et al. Jet energy measurement with the ATLAS detector in proton-proton collisions at $\sqrt{s}$ = 7 TeV. *Eur.Phys.J.*, C73:2304, 2013.

[51] Chris Young. Plot of jet resolution for different calibration schemes, including PFlow. private communication.

[52] C. Englert and E. Re. Bounding the top Yukawa coupling with Higgs-associated single top production. *Phys.Rev.*, 89(7):073020, April 2014.

[53] A. D. Bukin. Fitting function for asymmetric peaks. *arXiv:0711.4449*, November 2007.

[54] Jung Chang, Kingman Cheung, Jae Sik Lee, and Chih-Ting Lu. Probing the Top-Yukawa Coupling in Associated Higgs production with a Single Top Quark. 2014.

[55] Matthew T. Bowen. Using charge asymmetries to measure single top quark production at the LHC. *Phys.Rev.*, D73:097501, 2006.

[56] Georges Aad et al. Measurement of the top quark pair production charge asymmetry in proton-proton collisions at $\sqrt{s} = 7$ TeV using the ATLAS detector. *JHEP*, 1402:107, 2014.

[57] Serguei Chatrchyan et al. Measurements of the $t\bar{t}$ charge asymmetry using the dilepton decay channel in pp collisions at $\sqrt{s} = 7$ TeV. *JHEP*, 1404:191, 2014.

[58] Measurement of the top quark pair production cross section in the single-lepton channel with ATLAS in proton-proton collisions at 8 TeV using kinematic fits with b-tagging. Technical Report ATLAS-CONF-2012-149, CERN, Geneva, Nov 2012.

[59] Twiki website for HATHOR. `https://twiki.cern.ch/twiki/bin/view/Sandbox/CrossSectionsCalculationTool`. Accessed: 2014-09.